CHARACTERIZATION AND APPLICATIONS OF NEGATIVE-INDEX METAMATERIALS

A DISSERTATION
SUBMITTED TO THE DEPARTMENT OF PHYSICS
AND THE INSTITUTE OF ENGINEERING AND SCIENCE
OF BILKENT UNIVERSITY
IN PARTIAL FULFILLMENT OF THE REQUIREMENTS
FOR THE DEGREE OF
DOCTOR OF PHILOSOPHY

By

Koray Aydın

June, 2008

I certify that I have read this thesis and that in my opinion it is fully adequate, in scope and in quality, as a dissertation for the degree of Doctor of Philosophy.

_____

Prof. Dr. Ekmel Özbay (Supervisor)

I certify that I have read this thesis and that in my opinion it is fully adequate, in scope and in quality, as a dissertation for the degree of Doctor of Philosophy.

_____

Prof. Dr. Bilal Tanatar

I certify that I have read this thesis and that in my opinion it is fully adequate, in scope and in quality, as a dissertation for the degree of Doctor of Philosophy.

_____

Assist. Prof. Dr. M. Özgür Oktel

I certify that I have read this thesis and that in my opinion it is fully adequate, in scope and in quality, as a dissertation for the degree of Doctor of Philosophy.

_____

Assist. Prof. Dr. Vakur B. Ertürk

I certify that I have read this thesis and that in my opinion it is fully adequate, in scope and in quality, as a dissertation for the degree of Doctor of Philosophy.

_____

Prof. Dr. Süleyman Özçelik

Approved for the Institute of Engineering and Science:

_____

Prof. Dr. Mehmet Baray,
Director of the Institute of Engineering and Science

ABSTRACT

CHARACTERIZATION AND APPLICATIONS OF NEGATIVE-INDEX METAMATERIALS

Koray Aydın
PhD in Physics
Supervisor: Prof. Dr. Ekmel Özbay
June, 2008

Metamaterials offer novel electromagnetic properties and promising applications including negative refraction, flat-lenses, superlenses, cloaking devices. In this thesis, we characterized the negative-index metamaterials that is composed of periodic arrangements of split-ring resonators (providing negative permeability) and thin wire (providing negative permittivity) arrays. The resonances of split-ring resonators (SRR) are investigated experimentally and theoretically. By combining SRR and wire arrays together, we observed a transmission band where both permittivity and permeability are simultaneously negative, indicating a left-handed behavior. Reflection measurements reveal that the impedance is matched to the free space at a certain frequency range. The left-handed metamaterial is also shown to exhibit negative refractive index by using three different experimental methods namely, refraction from a wedge-shaped negative-index metamaterial (NIM), beam-shift from a slab-shaped NIM and phase shift from NIMs with different lengths. Flat-lens behavior is observed from a slab-shaped negative-index metamaterial based microwave lenses. Furthermore, we demonstrated subwavelength imaging and subwavelength resolution by using thin superlenses constructed from SRR-wire arrays with an effective negative index. We have been able to image a point source with a record-level, $\lambda/8$ resolution. SRR

and wire arrays exhibit negative index provided that the wave propagates parallel to the plane of SRR structure which makes it hard to fabricate at higher frequencies. An alternative structure called fishnet metamaterial however could yield negative index with wave propagation normal to the structure. We observed left-handed transmission and negative phase velocity in fishnet type metamaterials. Finally, we studied enhanced transmission from a single subwavelength aperture by coupling incident electromagnetic wave to a single SRR placed at the near-field of the aperture.

***Keywords**:* Metamaterial, Left-Handed Material, Split Ring Resonator, Negative Permittivity, Negative Permeability, Negative Refraction, Negative-Phase Velocity, Flat-lens, Superlens, Subwavelength Imaging, Subwavelength Resolution, Enhanced Transmission.

ÖZET

NEGATİF İNDİSLİ METAMALZEMELERİN KARAKTERİZASYONU VE UYGULAMALARI

Koray Aydın
Fizik, Doktora
Tez Yöneticisi: Prof. Dr. Ekmel Özbay
Haziran 2008

Negatif kırılma, düz lens, süper lens ve görünmezlik pelerini gibi uygumaları bulunan metamalzemeler oldukça farklı elektromanyetik özelliklere sahiptirler. Bu tezde, negatif kırılma indisine sahip metamalzemelerin karakterizasyonu gerçekleştirilmiş ve mikrodalga uygulamalarından birkaçı gösterilmiştir. Bu metamalzemeler negatif permeabiliteye sahip yarıklı halka rezonatörleri ile negatif permitiviteye sahip ince tel yapıları bir araya getirilerek oluşturulmuştur. Yarıklı halka rezonatörlerinin rezonans karakteristikleri deneysel ve teorik olarak incelenmiştir. Yarıklı halka rezonatörleri ile tel yapılarının bir araya getirilmesi sonucu permitivite ve permeabilite değerlerinin eksi olduğu frekanslarda bir geçirgenlik bandı gözlemlenmiş ve bu bant boyunca metamalzemenin dalga vektörü, elektrik alan ve manyetik alanları için sol-el kuralına uyduğu belirlenmiştir. Bu metamalzemenin negatif kırılma indisine sahip olduğu üç farklı ve birbirinden bağımsız deneysel yöntem kullanılarak gösterilmiştir. Bu deneysel yöntemler; prizma şeklindeki metamalzemeden kırılma deneyi, düz metamalzeme levhadan dalganın yer değişiminin gözlemlenmesi ve farklı uzunluklardaki metamalzemelerden faz farkının ölçülmesidir. Mikrodalga boyutlarında çalışan ve düzgün yüzeye sahip lens başarıyla gösterildi. Ayrıca, negatif indise sahip

metamalzeme bazlı süperlenslerin dalgaboyu altı görüntüleme ve çözünürlük için kullanılabileceği deenysel olarak ispatlanmıştır. Rekor seviyede dalgaboyunun sekizde biri çözünürlük elde edilmiştir. Ağ şeklindeki alternatif metamalzemelerin de negatif indis ve negatif faz hızına sahip olduğu başarıyla gösterilmiştir. Son olarak tek bir dalgaboyu altı delikten yarıklı halka rezonatörü kullanarak arttırılmış iletim (transmiyon) çalışılmıştır.

***Keywords**:* Metamalzeme, Solak malzeme, Yarıklı halka rezonatörü, Negatif Permeabilite, Negatif Permitivite, Negatif Kırılma, Negatif Faz Hızı, Düz Lens, Süperlens, Dalgaboyu-altı Görüntüleme, Dalgaboyu-altı Çözünürlük, Arttırlmış İletim.

Acknowledgements

It is my pleasure to express my deepest gratitude and respect to Prof. Dr. Ekmel Özbay for his invaluable guidance, helpful suggestions and endless support. His personal and academic virtue shaped my academic personality and changed my approach to scientific study. I am very lucky to have the opportunity to study under his tutelage.

I would like to thank to the members of my thesis committee, Prof. Dr. Bilal Tanatar, Assist. Prof. Dr. Mehmet Özgür Oktel, Assist. Prof. Dr. Vakur B. Ertürk, and Prof. Dr. Süleyman Özçelik for reading the manuscript and commenting on the thesis.

I am very fortunate to have been a member of the Özbay group, where I had a chance to work together and benefit from brilliant, intelligent and excited people. I am indebted to Dr. Mehmet Bayındır for teaching how to use microwave experiment setup and guiding me at the very beginning of my academic study. Special thanks to Ertuğrul Çubukçu for his help, understanding and friendship. I appreciate Dr. Kaan Güven, İrfan Bulu and Dr. Zhaofeng Li for their continuous support during my research. This thesis would never been succesful with the endless help of the Özbay group members. I also had a chance to collaborate with Hümeyra Çağlayan, Levent Şahin, Şerafettin Bilge and Atilla Özgür Cakmak. Thank you all. I appreciate the efforts of Serkan Bütün, Murat Güre and Erkin Ülker for teaching me optical lithography and Bayram Bütün for his help during hybrid inorganic-organic light emitting sources project. Indeed, all of the people with whom I've overlapped in the Özbay group have contributed to my academic

and social life; for this I thank Necmi Bıyıklı, İbrahim Kimukin, M. Deniz Çalışkan, Turgut Tut, Süheyla Sena Akarca-Bıyıklı, Özgür Kelekçi, Evrim Çolak, Tolga Yelboğa, Evren Öztekin, Muhammed Acar, Mustafa Öztürk.

I would like to thank the members of Nanotechnology Research Center and Advanced Research Laboratory for making my life easier. I am also thankful to my professors and friends in the Department of Physics. Special thanks to Aşkın Kocabaş, Muhammed Yönaç, Levent Subaşı, Dündar Yılmaz, Engin Durgun, Sefa Dağ, M. Emre Taşgın, and R. Volga Ovalı, with whom I had a great time during my life in Bilkent.

There is a long list of my close friends, whether old or new, far away of nearby; to feel their existence is my life source. Thank you all.

I would like to express my endless thanks to my mother, father and sister for their love, encouragement and care. I would also thank to my new family, who doubled the support and encouragement I have.

Finally, special thanks go to my wife, **Elif**, for her boundless love, endless trust and to my son, **Said Enes**, for shining a different color onto my life. I cannot imagine finishing all my achievements without their endless moral support. I dedicate this labor to my wife and my son.

Contents

List of Figures

Chapter 1

Introduction

Electromagnetic waves play key role in our daily life, since they are essential for many applications including communication, imaging, sensing and devices like antennas, light sources, optical fibers, lenses, etc. Spanning from extremely low frequencies up to Gamma rays, the electromagnetic wave phenomena always received great interest and scientists widely studied the interaction of waves with the matter. Propagation of electromagnetic waves in free space is less interesting. It is the interaction between waves and materials that led to the many applications and devices listed above. Transmission, reflection, refraction, diffraction are among the many affects resulting from the interaction between waves and materials. Materials response to an incident electromagnetic wave is determined by their macroscopic electromagnetic parameters, namely the dielectric permittivity (ε) and the magnetic permeability (μ). Ordinary materials usually have positive values of ε and μ. The response from the ordinary materials is only a small fraction that one can access theoretically. Material responses could be extended to the values that are not readily available by designing artificial structures, so called metamaterials. The phrase “Meta” is borrowed from Greek meaning “beyond”. Materials are composed of atoms that are much smaller than the wavelength of light. To describe the interaction of light with a material, one can take an average

over the atomic scale, so that the atomic details are not important. It is then considered as a homogeneous medium and one can define the electromagnetic parameters; the permittivity and the permeability to describe the electromagnetic response. An analogy could easily be established with the metamaterials, where their building blocks, the meta-atoms, are much smaller than the wavelength of the electromagnetic wave and thus one can assign effective permittivity and permeability. What makes metamaterials so interesting is that one can tailor the electromagnetic parameters to have any desired value within theoretical limits, including negative ones.

The interest in metamaterial research started at the beginning of 21th century, after the successful demonstration of a metamaterial with simultaneously negative values of dielectric permittivity and magnetic permeability [1]. However, it was forty years ago, at 1968, when a Russian physicist dreamed about a conceptual material in which ε and μ are both negative [2]. His dream had to wait for forty years, since negative value of permeability was a hidden treasure that is later discovered by Sir John B. Pendry in 1999 [3]. The term left-handed material is coined by Veselago for such structures having simultaneously negative values of ε and μ. Refractive index then possesses negative values that are not achievable with known materials. A negative index reverses many of known optical affects and changes the way we treat optics and electromagnetism. After 2000, there has been a growing interest in metamaterials where the number of papers in metamaterials, negative refraction and related studies doubled every ten months (Fig. 1.1), following an effective Moore's Law [4]. Although it has been eight years since the beginning of the metamaterial field, we witnessed publication of five books on this specific topic, indicating the interest of scientific community to metamaterials [5-9]. Even a journal named "Metamaterials" has been launched by Wiley.

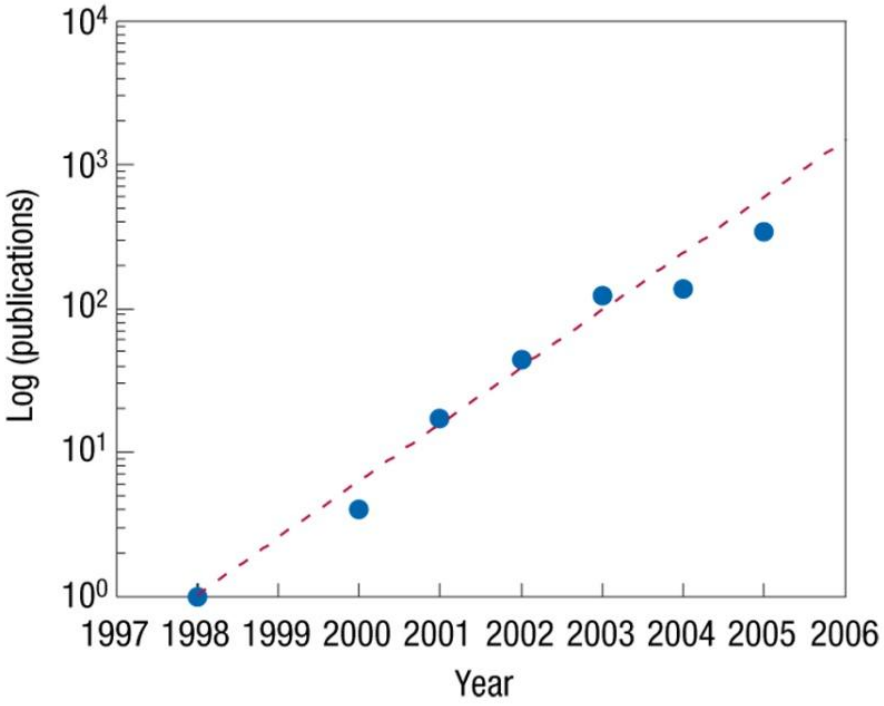

Figure 1.1: The number of articles published in SCI journals on the topics of metamaterials and negative refraction. (after [4])

1.1. Motivation

Metamaterials offer a wide range of exciting physical phenomena that are not attainable with ubiquitous materials. Artificial magnetism is among one of the exotic electromagnetic property of metamaterials. Magnetic response could be attained from non-magnetic materials by designing structures into capacitive and inductive elements. An example of such structures is a split-ring resonator. One can tailor the magnetic permeability to any desired value including negative values. This in turn brings the possibility of engineering metamaterials with a negative-index provided that effective permeability and permittivity of the resulting structure are simultaneously negative within a frequency range [10]. Metamaterials are not the only route to achieve negative refraction. Photonic

crystals are proposed for refracting electromagnetic waves negatively, where the permittivity and permeability are both positive [11-15]. Plasmonic effects could also be used at optical frequencies to yield negative refraction [16]. Negative refraction is also demonstrated by using semiconductor metamaterials [17].

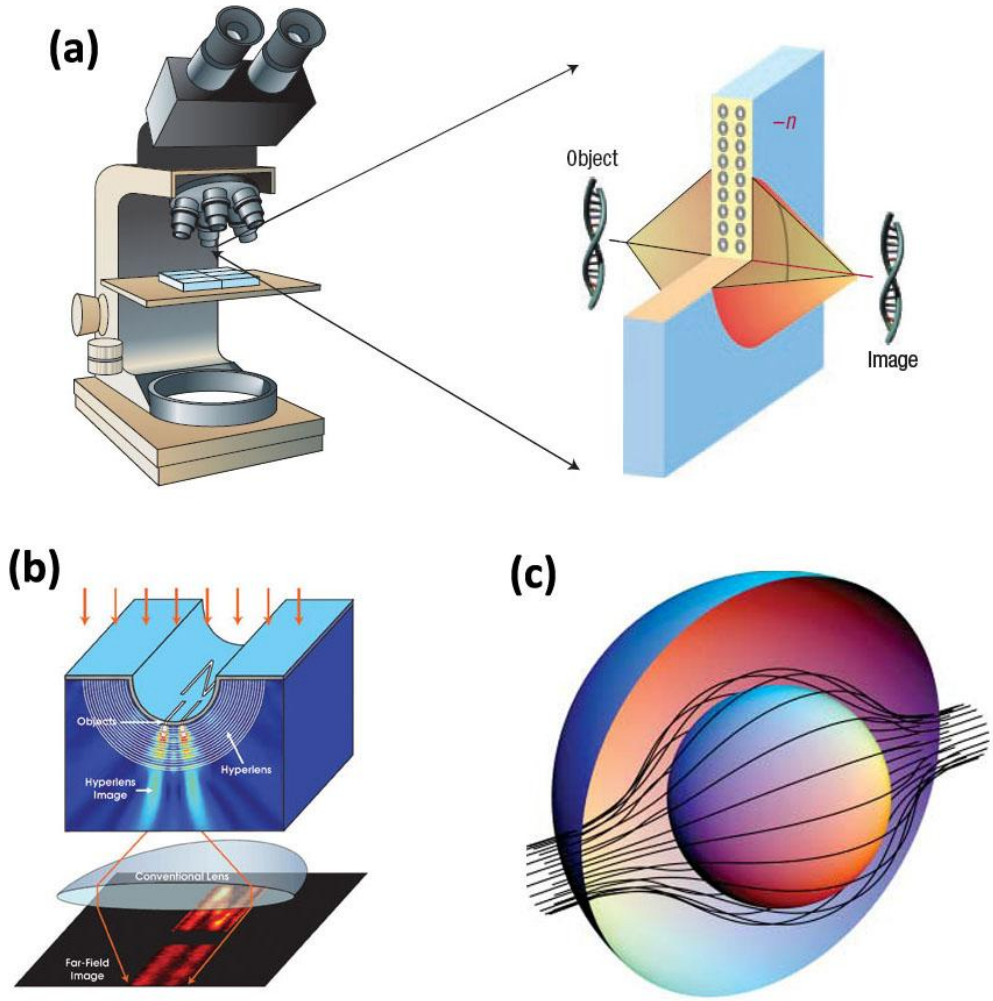

Figure 1.2: Some applications of metamaterials. (a) Superlens (after [28]), (b) magnifying hyperlens (after [30]), (c) cloaking device (after [32]).

One of the most exciting applications of negative-index metamaterials (NIM) is a perfect lens. Stimulated by J. B. Pendry's seminal work [18], superlenses that are capable of imaging subwavelength size objects (Fig. 1.2(a)) attracted great deal of interest [19-28]. Hyperlenses composed of anisotropic metamaterials with hyperbolic dispersion are alternative imaging systems (Fig. 1.2(b)) providing magnification of small objects [29-31].

Although the scientists focused their efforts specifically to negative permeability and negative index metamaterials at the beginning, later it was found out that there are many interesting regions at the electromagnetic parameter space that can be accessed by metamaterials. It is possible to construct a cloaking device (Fig. 1.3(c) that could be used to "hide" an object inside it provided that either $0 < \varepsilon < 1$, or $0 < \mu < 1$ [32-34]. Another interesting application is supercoupling, tunneling and electromagnetic energy squeezing through very narrow channels by utilizing metamaterials with near-zero parameters, i.e. $\varepsilon \sim 0$ or $\mu \sim 0$ [35-37].

Metamaterials are geometrically scalable, thus offering a wide range of operation frequencies including radio [38, 39], microwave [40-52], millimeter-wave [53], far infrared (IR) [54], mid-IR [55, 56], near-IR frequencies [57-60] and even visible wavelengths [61, 62].

1.2. Outline of this thesis

In this thesis, we investigate the properties of metamaterials at microwave frequencies. Although the core of this thesis is based on the experimental measurements, numerical simulations are also utilized to understand the physical mechanisms and verify the measured results.

In Chapter 2, the building block of a left-handed metamaterial (LHM), split-ring resonators (SRR) are studied in detail. Starting from a single SRR unit cell and verifying the origin of resonances, we have been successfully demonstrated

the magnetic resonance behavior. Periodic arrays are then formed to obtain an effective medium giving negative values of permeability. Detailed experimental and numerical studies are performed to understand the dependence of SRR's parameters on the magnetic resonance frequency. This section is concluded with a capacitor-loaded split-ring resonator structure that is utilized to tune the magnetic resonance frequency of SRR.

Chapter 3 is devoted to the characterization of negative-index metamaterials that is obtained by combining SRR-arrays together with a thin-wire media. The section starts with a small discussion about negative permittivity structures at microwave frequencies where the experimental results are presented. Transmission and reflection characteristics of one-dimensional left-handed metamaterials are provided. Effective parameters of the corresponding LHM structure are retrieved from the calculated transmission and reflection amplitudes and phases. Negative refraction is then demonstrated by using two different experimental methods, namely refraction from a wedge-shaped LHM and from a slab-shaped LHM. Finally, phase shift between the consecutive number of layers of LHM structure is measured to be negative at frequencies where both permittivity and permeability were negative, indicating a negative phase velocity.

Verifying the negative-index for the metamaterial structures, we took an additional step to demonstrate the proposed flat-lens focusing behavior in Chapter 4. A slab-shaped LHM lens is used to focus a point source that is not achievable with a lens made of positive-index material. The chapter discusses the image formation for the sources located outside the lens, as well as the case when the sources are embedded within the flat-lens.

Chapter 5 describes the experimental demonstration of a negative-index metamaterial (NIM) based superlens that is capable of imaging subwavelength objects with a resolution of $\lambda/8$. The superlens was operated at an impedance-matched frequency to assure that the losses due to the reflection are kept at the minimum level. Moreover, subwavelength resolution is achieved with two point

sources separated by a distance eight times smaller than the wavelength. The effect of thickness of the superlens on the resolving power is experimentally studied, in which a thicker superlens resulted in a lower resolving power due to increased losses.

A planar metamaterial composed of metallic slab and wire pairs is shown to be a promising alternative to the SRR-wire type metamaterials in chapter 6. These metamaterials are also named as fishnet type NIMs is characterized at microwave frequencies and retrieved effective parameters verified a negative-index frequency band. Phase measurements are performed to demonstrate the negative phase advance in these structures. Further numerical simulations showed that the backward-wave propagation within NIM structure, supporting the negative-phase velocity behavior.

In chapter 7, we proposed and demonstrated enhanced transmission from a single subwavelength aperture by placing a single split-ring resonator at the near-field of the aperture. The aperture radius is $\lambda/20$, the smallest aperture known for achieving enhanced transmission. One can employ electric and/or magnetic resonance of SRR structure to yield extraordinary transmission properties.

Finally, chapter 8 summarizes the achievements in the thesis.

Chapter 2

Magnetism from split-ring resonators

2.1. Introduction

The response of materials to the incident magnetic field is determined by magnetic permeability. Magnetic permeability is positive in usual materials. The absence of the negative values of magnetic permeability provided little motivation for studying negative-index materials. Because of the lack of magnetic charge analogous to an electric charge, it is more difficult to obtain a material with negative magnetic permeability. To obtain negative permeability, one has to extend the magnetic properties of the materials. In 1999, Pendry *et al.* introduced several configurations of conducting scattering elements displaying a magnetic response to an applied electromagnetic field when grouped into an interacting periodic array [3]. The resonant behavior of SRRs is due to the capacitive elements (gaps and splits), which in turn results in rather high positive and negative values of permeability near the magnetic resonance frequency (ω_{m}).

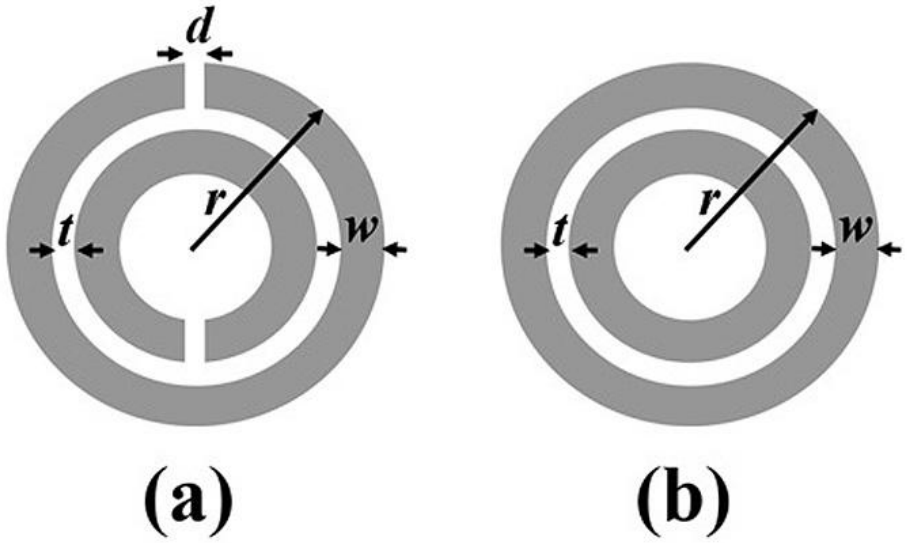

Figure 2.1: Schematic drawings of (a) Single unit cell of SRR, (b) Single unit cell of CRR.

Figure 2.1(a) shows the design of Pendry, described as a split ring resonator (SRR). In a split ring resonator there are two rings both having a split. By having splits in the rings, the SRR unit can be made resonant at wavelengths much larger than the diameter of the rings. The purpose of the second split ring, inside and whose split is oriented oppositely to the outside split, is to generate a large capacitance in the small gap region. The gap between the rings prevents current from flowing around any one ring. However, there is a considerable capacitance between the two rings, which enables current to flow.

2.2. Resonances of a single split-ring resonator

In this section, we studied transmission through a single unit cell of SRR in order to gain an understanding of the resonant behavior of SRR. Split-ring resonators under investigation are built from concentric metal rings on a dielectric printed

circuit board with a thickness of 1.6 mm and ε = 3.85 [46]. A schematic drawing of split ring resonator can be seen in Fig. 2.1(a). The width of the splits and the gap between the inner and outer rings are 0.2 mm, the metal width is 0.9 mm, and the outer radius is 3.6 mm. The deposited metal is copper with a thickness of 30 μm. We also fabricated a ring resonator structure in which the splits are removed [46]. The resulting structure is named conventionally as a closed ring resonator (CRR) and shown schematically in Fig. 2.1(b).

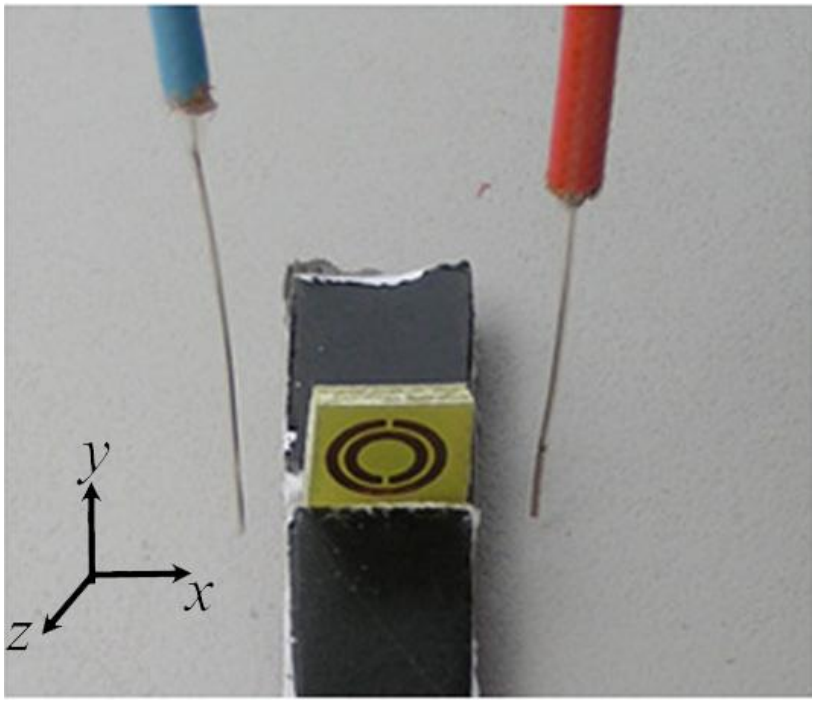

Figure 2.2: Experimental setup for measuring transmission through a single unit cell of SRR structure. The structure is placed between two monopole antennas.

The resonance behavior could be observed from the frequency response of single SRR[47, 63-65]. Two monopole antennas are used to transmit and detect the EM waves through the single SRR unit cell. The monopole antenna was constructed by removing the shield around one end of a microwave coaxial cable. The exposed center conductor which also acted as the transmitter and receiver was

on the order of λ/2, arranged to work at the frequency range covering the magnetic resonance frequency (ω_m) of the SRR structures. A single SRR is placed between the monopole antennas as shown in Fig. 2.2. The distance between the monopole and SRR unit cell is 6 mm. Monopole antennas are then connected to the HP-8510C network analyzer to measure the transmission coefficients. First we measured the transmission spectra in free space (i.e. without SRR unit cell) which is used as the calibration data for the network analyzer. Then, SRR unit cell was inserted between the monopole antennas, and we performed the transmission measurements by maintaining distance between the transmitter and receiver monopole antennas fixed.

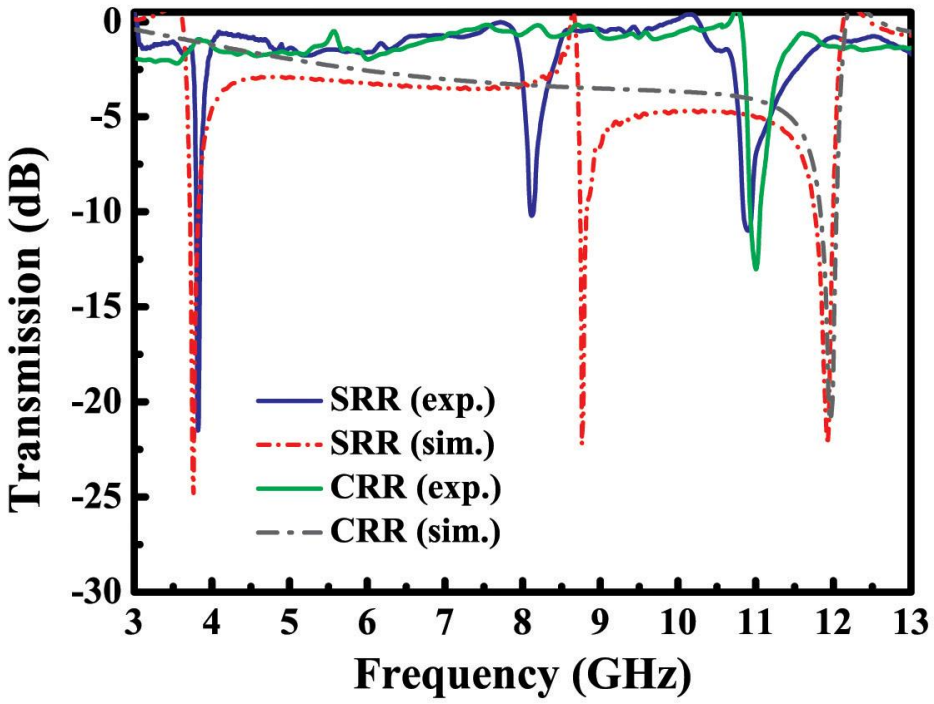

Figure 2.3: Measured and simulated frequency responses of single SRR and CRR structures.

We first measured the frequency response of the single split ring resonator and closed ring resonator unit cells. The measured frequency response of single SRR (blue line) and single CRR (green line) is provided in Fig. 2.3. As seen in the figure, three transmission dips were observed at the frequencies 3.82, 8.12, and 10.90 GHz throughout the transmission spectrum of single SRR [65, 66]. On the other hand, a single dip was observed at 10.92 GHz for a single CRR.

We also performed simulations to check the experimental results. Simulations are performed by using commercial software, CST Microwave Studio which is a 3D full-wave solver, employing the finite integration technique (FIT). In order to determine the resonance frequencies of the structures under consideration, we have included one layer of the SRR structures along the propagation direction. In the simulation setup, the structures are subjected to an incident plane wave. Open boundary conditions are employed along the propagation direction. Periodic boundary conditions are used along the directions other than the propagation direction. Hence, the structure is assumed to be periodic and infinite along the directions that are perpendicular to the propagation direction. The transmission amplitudes are obtained by measuring the fields at a distant point from the structures. This point was chosen such that beyond this point the transmission coefficients do not change with the increasing distance. Such a choice was made to exclude the near-field effects due to the highly resonant nature of the structures under consideration. The simulated frequency responses of SRR (red dashed-dotted line) and CRR (grey dashed-dotted line) are given in Fig. 2.3. The simulations agree well with the experiments.

The splits in the split ring resonators structure play a key role in obtaining magnetic resonance. Removing the splits prevents the current from flowing between the inner and outer rings, and therefore, the magnetic resonance is no longer present. Based on this principle, we observed two magnetic resonances for split ring resonator structure at ω_{m1}= 3.82 GHz and ω_{m2}= 8.12 GHz. Notice that the wavelength is 7.86 cm, whereas the diameter of the SRR structure is 7.2 mm.

Therefore, by employing the aforementioned SRR structure with sizes corresponding to the $1/11^{th}$ of free space wavelength, magnetic resonance can be obtained. The wavelength in the material (4.0 cm) is even approximately $1/6^{th}$ of structure size. The reason why SRR received a great amount of interest is not only because of being a source for negative permeability, but also for achieving resonance with subwavelength features. Therefore, an effective medium theory becomes applicable for SRR media, and LHMs.

Split ring resonator not only exhibits magnetic resonance induced by the splits at the rings, but electric resonance is also present via the dipole-like charge distribution along the incident electric field [46, 49]. Such an electric resonance behavior is observed at ω_e=10.90 GHz for the split ring resonator and closed ring resonator unit cells.

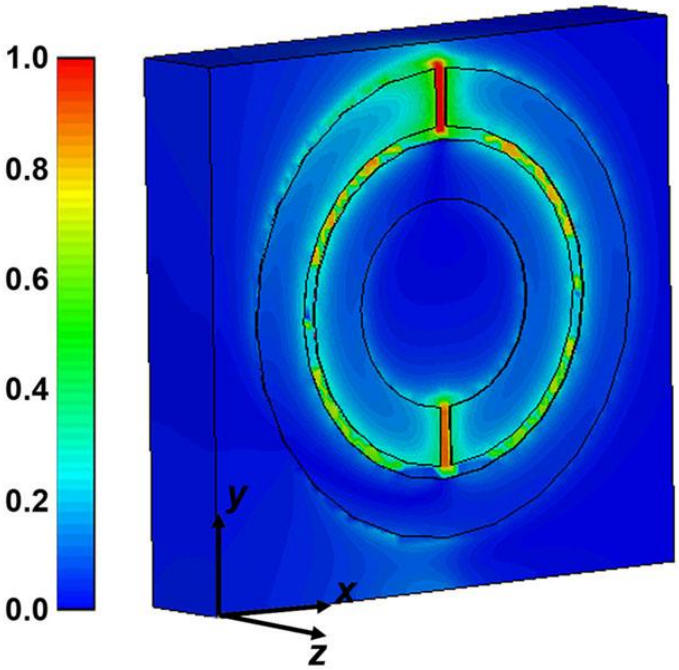

Figure 2.4: Simulated electric field intensity profile at the magnetic resonance frequency of the split ring resonator.

We have simulated the electric field intensity at the magnetic resonance frequency of SRR, 3.82 GHz. Electric field monitor is placed at the resonance frequency and the resulting intensity profile is plotted in Fig. 2.4. The intensities are normalized with respect to the maximum intensity value. It is clear that the electric field is concentrated at the splits and the gaps between the concentric rings. The strongest localization occurred at the outer ring's split region. The E-field is also localized at the inner split region and gap region but localization is not as strong as the case in the outer split region [67].

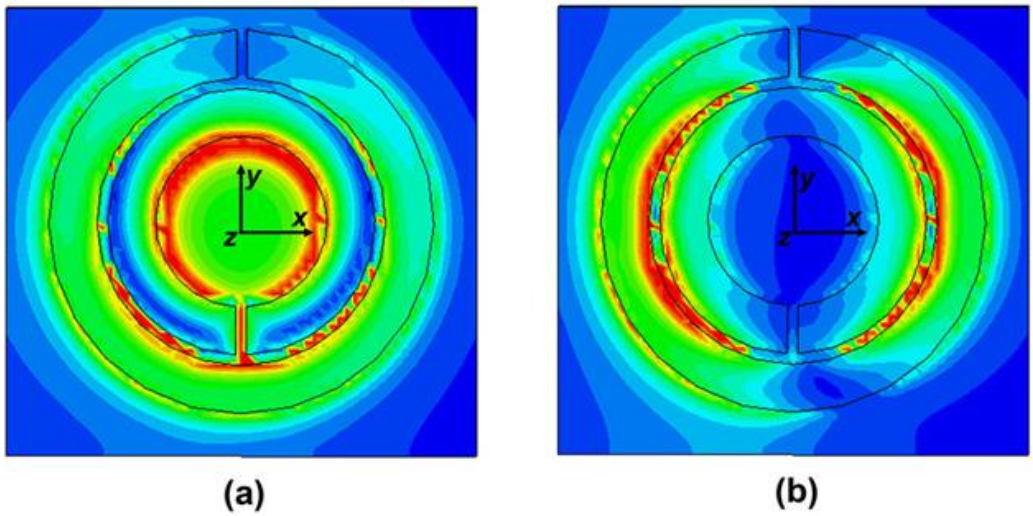

Figure 2.5: Simulated magnetic field magnitudes of a single SRR at (a) 3.82 GHz, and (b) 11.92 GHz.

We also performed simulations in order to monitor the magnitude of the magnetic field at the SRR structure. The simulations were performed at 3.82 GHz and 11.92 GHz, which correspond to the transmission dip in the simulated transmission spectrum of SRR (former is the magnetic, latter is the electrical resonance) [65]. The magnitude of the magnetic fields is shown in Fig. 2.5. As clearly seen in Fig. 2.5(a), a circular current is present at the SRR. Such a circular current excites the magnetic resonance, and therefore, a transmission dip was observed at 3.82 GHz in simulations. However, the behavior of the magnetic field

changes at 11.92 GHz (see Fig. 2.5(b)). The direction of the current flow is not circular, but rather an up-down direction. Since the current is not circular the magnetic resonance cannot be excited. The transmission dip at this frequency can only be due to the electrical resonance of the ring resonator structure.

2.3. Negative permeability media: Periodic arrays of split ring resonators

In the previous section we studied frequency response of single SRR and CRR unit cells. If these structures are combined together, the coupling between the resonators results in band gaps around the resonance frequencies. By combining the SRRs into a periodic medium, such that there is strong magnetic coupling between the resonators, unique properties emerge from the composite and isotropy can be achieved. One of the unique properties is the availability of negative values of permeability.

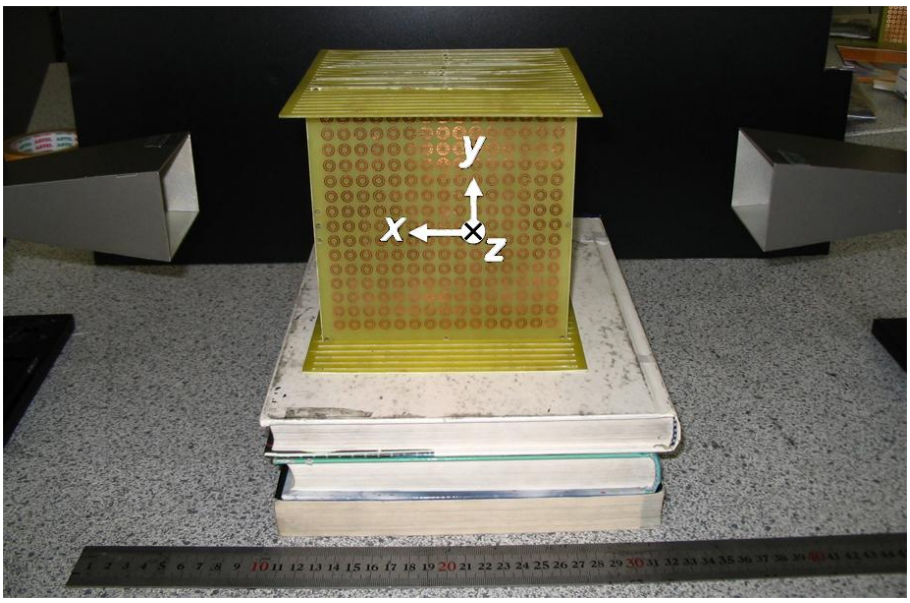

Figure 2.6: Experimental setup for transmission measurements.

To obtain negative permeability, we periodically arranged SRR structures. The number of unit cells along the *x*, *y*, and *z* directions are $N_x = 10$, $N_y = 15$, and $N_z = 25$, with lattice spacings $a_x = a_y = 8.8$ mm and $a_z = 6.5$ mm. The directions can be seen in Fig. 2.2. The wavevector is along the *x* direction, while E-field is along the *y* direction, and H-field is along the *z* direction. Experimental setup for measuring the transmission-amplitude and transmission-phase spectra consists of a HP 8510C network analyzer, and standard high gain microwave horn antennas as shown in Fig. 2.6.

Figure 2.7 shows the measured and simulated transmission spectra of periodic SRRs and CRRs. The first band gap between 3.55-4.05 GHz is observed at the transmission spectrum of SRR array but not in CRR array. However, the second band gap between 8.15-11.95 GHz is observed for both cases. As clearly seen in the figure, the agreement between the measured and simulated data is good.

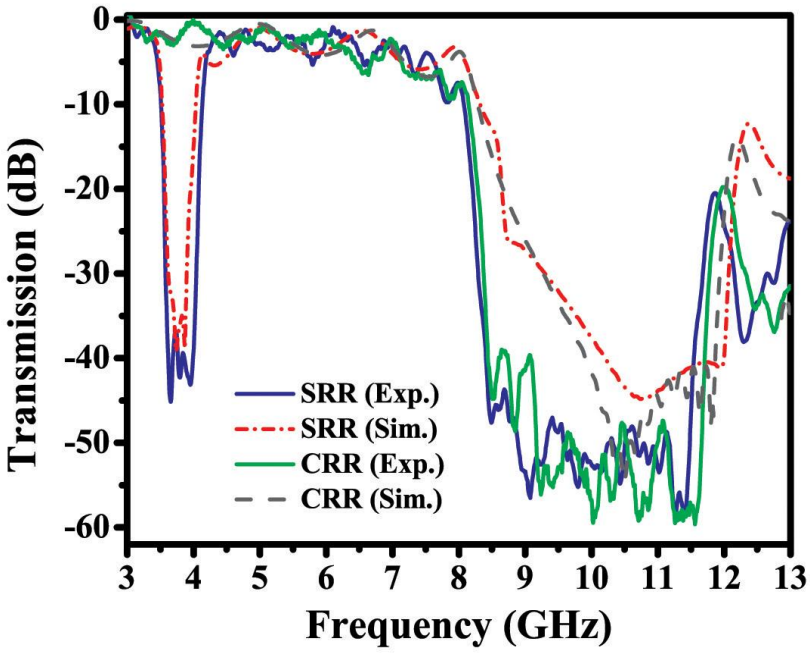

Figure 2.7: Measured and simulated transmission spectra of SRR and CRR arrays.

Based on the measurements and simulations, we can safely claim that the stop bands of split ring resonator media cannot be assumed as a result of "negative μ" behavior. Some of the observed gaps (such as the second band gap in this measurement) in the transmission spectra could also originate from the electrical response of the split ring resonators or from Bragg gaps due to periodicity [46]. The band gap between 3.55-4.05 GHz is due to the magnetic response of split ring resonators. However, the stop band 8.15-11.95 GHz appeared due to the electrical response of the concentric rings.

2.4. Effect of SRR parameters on magnetic resonance frequency

The SRR structure has capacitive elements that increase the response of the material to the incident EM radiation. Capacitance due to the splits prevents current to flow around the rings but the mutual capacitance between the two rings enables the flow of the current through the structure. Since SRRs play an important role for the construction of LHMs with negative index, considerable amount of effort has been given to understand the underlying physics of these negative permeabiltiy materials [68-79]. There are several analytical models in the literature studying the magnetic and electrical resonances of SRRs. It is possible to model an individual SRR as an L-C circuit system Total capacitance of the SRR system has mainly two contributions, one arising from the splits and the other from the gap between the concentric rings. Inductances arise from the conducting rings and gap between inner and outer rings. In this section we will investigate certain geometrical parameters like split width, gap between the rings, metal width and additional capacitors and their effect on ω_m [63].

2.4.1. Effect of split width

Schematic drawing of an individual SRR is given in Fig. 2.1(a), with parameters split width (*d*), gap distance (*t*), metal width (*w*) and radius of the outer ring (*r*). Initially the parameters are taken to be $d = t = 0.2$ mm, $w = 0.9$ mm and $r = 3.6$ mm. By keeping other parameters constant, we only changed the split width (*d*) of SRRs.

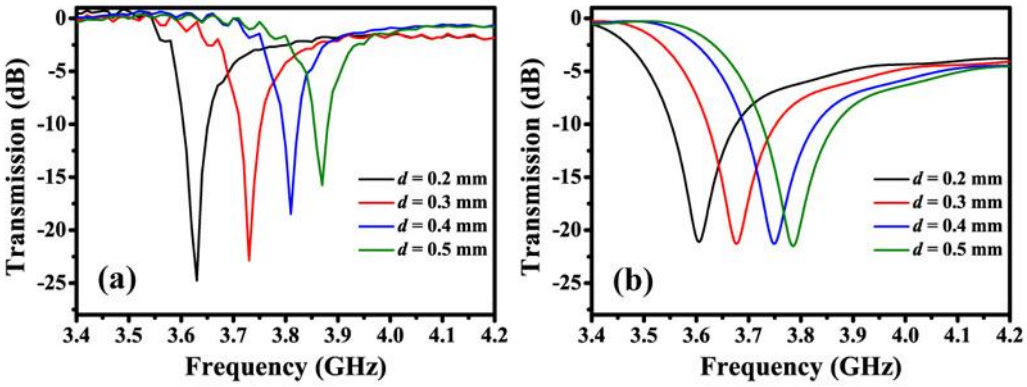

Figure 2.8: Transmission spectra of individual SRRs with different split widths obtained via (a) experiment, and (b) simulation.

Figure 2.8(a) displays the measured transmission spectra of 4 SRR structures with different split widths ($d = 0.2$, 0.3, 0.4 and 0.5 mm). A dip in the transmission spectra was observed for all SRR structures. Figure 2.8(b) shows the simulated transmission spectra and there is a good agreement between experimental results and numerical simulations.

The splits behave like a parallel plate capacitor. We can think of two metal plates of thicknesses 30 μm and widths 0.9 mm are placed with a distance *d* away from each other. Since we increase the split width, the capacitance due to splits will decrease, which in turn will decrease the total capacitance of the system.

Previously developed analytical models of SRRs [75, 76] predict the same behavior: Decreasing the capacitance of the system will increase the resonance frequency. Therefore experimental results and simulations provided in this section agree well with the analytical models in the literature [75, 76].

2.4.2. Effect of gap distance

In this section we studied the effect of gap between inner and outer rings on ω_m of SRR structures. The other parameters are kept constant (d = 0.2 mm, w = 0.9 mm and r = 3.6 mm), and only gap distance (t) is varied from 0.2 to 0.5 with 0.1 mm steps. Since we fixed the radius of the outer ring, increasing the gap distance will also decrease the size of the inner ring.

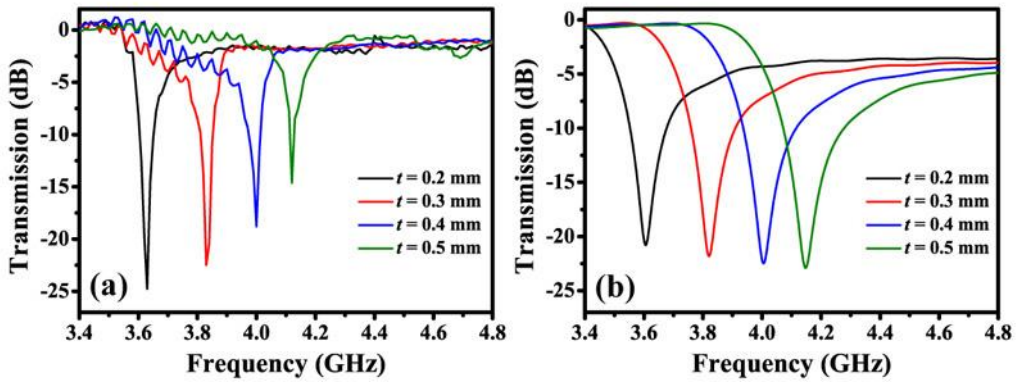

Figure 2.9: Transmission spectra of individual SRRs with different gap distances obtained via (a) experiment, and (b) simulation.

Figure 2.9(a) and (b) display the measured and simulated transmission spectra of SRRs with different gap distances. Resonant behavior is observed both experimentally and numerically at similar frequencies. Increasing the distance between inner and outer rings, results in an increase of the magnetic resonance frequency of SRR structure.

Changing the distance between the inner and outer rings will change the mutual capacitance and mutual inductance between the rings. Analytical model by Sauivac *et al.* proposes that increasing the gap distance, decreases both mutual capacitance and mutual inductance of the equivalent LC circuit of SRR system [75]. By following the formulation of the model given in [75], ω_m is found to increase with increasing gap distances, that agrees with the results of experiments and simulations.

2.4.3. Effect of metal width

In this section we changed the metal width of both inner and outer rings. The other parameters are kept constant (d = t = 0.2 mm, and r = 3.6 mm). Keep in mind that by fixing the radius of the outer ring, the size of the inner ring is larger for narrower ring configurations.

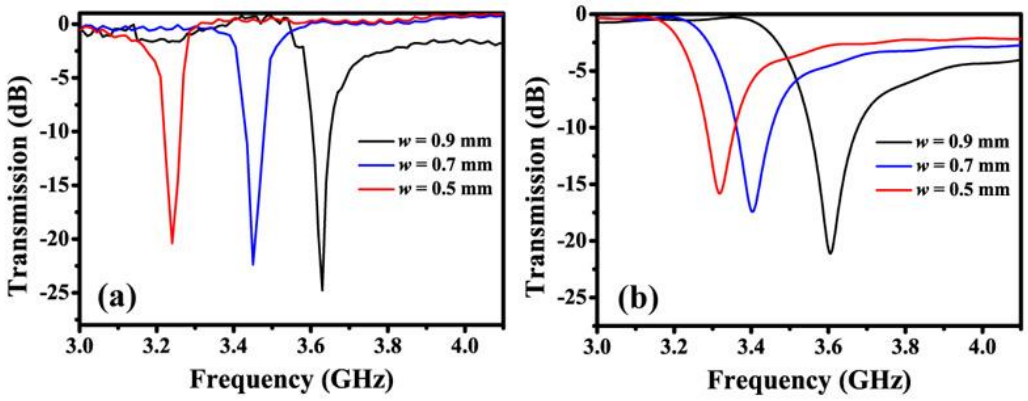

Figure 2.10: Transmission spectra of individual SRRs with different metal widths obtained via (a) experiment, and (b) simulation.

Figure 2.10(a) and (b) display the measured and simulated transmission spectra of SRR structures with different metal widths (w = 0.5, 0.7, and 0.9 mm). Both experiments and simulations predict that ω_m increases with increasing metal width.

Metal width affects all capacitances and inductances due to analytical model of Sauivac *et al.* [75]. Increasing the metal width will decrease the mutual inductance and mutual capacitance. Therefore SRRs made of thinner rings will have smaller resonant frequencies. This result agrees with both experiment and simulations reported in this section.

2.5. Capacitor-loaded split-ring resonators as tunable metamaterial components

Total capacitance of the SRR system has mainly two contributions. The first one is the capacitance at the split regions and the second contribution is from the gap between the concentric rings. These capacitances together with the inductances from the rings, determine the ω_m of the resonator structure. Changing the capacitance and inductance values results in a change in ω_m of SRRs, as expected from an L-C circuit. Surface mount capacitors with various capacitance values are placed at three different capacitive regions of SRRs. Namely, (i) the gap region between inner and outer rings, (ii) outer ring's split region and (iii) inner ring's split region [67]. The photographs of the SRRs loaded with capacitors are given in the insets of Fig. 2.11 (a), (b) and (c), respectively.

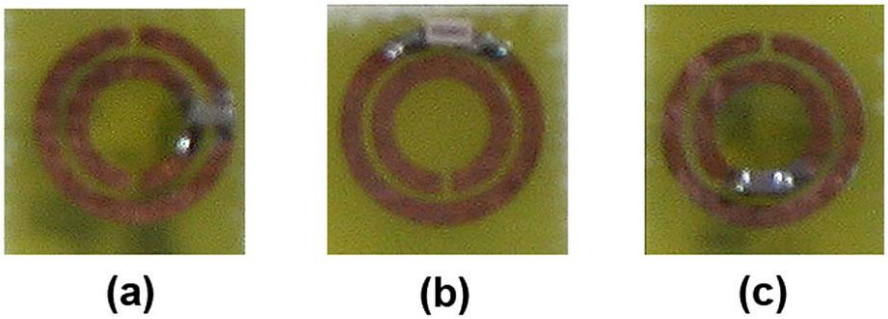

Figure 2.11: SRR with capacitor loaded (a) in the gap region between concentric rings, (b) in the outer split region, and (c) in the inner split region

The magnetic resonance frequencies of SRRs as a function of capacitances loaded at different capacitive regions are shown in Fig. 2.12 with corresponding data points. Magnetic resonance frequency of SRR without any additional capacitance is measured at 3.82 GHz. It is clear from figure that the highest amount of tuning can be achieved by loading capacitances at the outer split region.

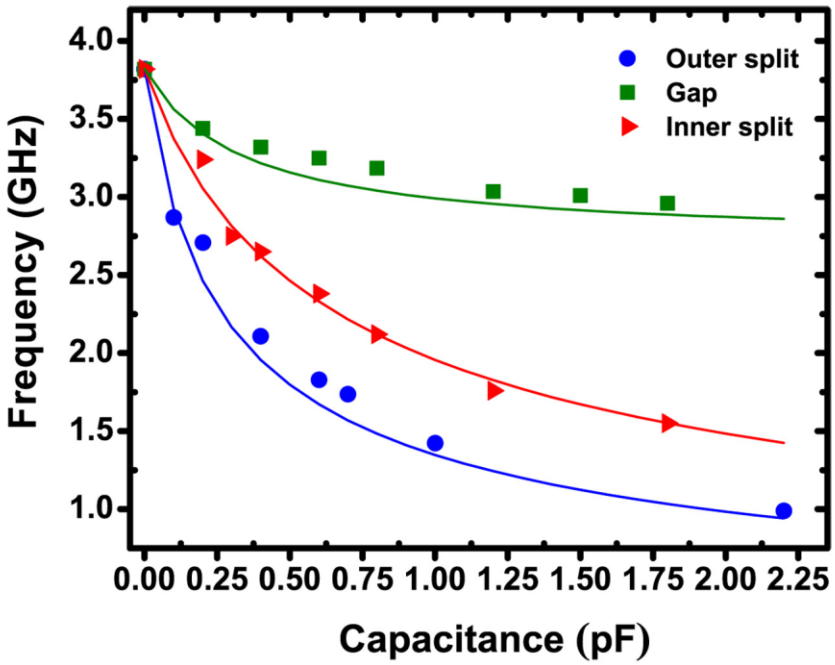

Figure 2.12: Magnetic resonance frequency of a split ring resonator as a function of loaded-capacitances at different capacitive regions. Solid lines are the results obtained from the numerical models.

In general the split capacitances are relatively small and can be ignored. However, if a capacitor is loaded in the split region, the split capacitance becomes important and affects resonance frequency as observed in our study. In ref. [76] and [74], the capacitances due to the splits were taken into account; therefore we will use this model to compare our experimental results. The approximate formula for the lowest magnetic resonance frequency is given in [74] as:

$$\omega_m = \left(\sqrt{2\pi L_{av}(\pi C_g / 2 + C_{s1} + C_{s2}}\right)^{-1} \quad , \qquad (2.1)$$

where L_{av} is the average inductance of the two rings, C_g is the capacitance due to the gap, C_{s1} and C_{s2} are capacitances due to the outer and the inner splits, respectively. By using the formula provided in [75], we calculated the gap capacitance as C_g=0.14 pF. The capacitances due to the splits are calculated to be C_{s1}=C_{s2} =1.2 fF. Since the magnetic resonance frequency of our SRR structure is at ω_m=3.82 GHz, putting the known parameters in (2.1) average inductance is found to be L_{av}=76.7 nH. The capacitors inserted at the split region is connected in parallel to the split capacitance, therefore we can insert C_{s1}=C in (2.1) and plot the corresponding curve for the outer split. Note that C is the capacitance value of the surface mount capacitor. The results obtained from the model are plotted with blue line in Fig. 2.12 and the results extremely agree well with experimental data. It is clear from the experimental observations that the effect of the capacitance in the inner split region is less than the outer split region. Therefore we can introduce a phenomenological factor in the model to obtain the best fit with the experimental data. In (1) if we put $0.4\times C_{s2}$ instead of C_{s2}, the red line in Fig. 2.12 is obtained. As clearly seen, the match between the model and the experimental results are quite good.

As a comparison, ω_m shifted down to 2.86 GHz with a 3.3 pF capacitor loaded at the gap region. But same amount of tuning has been achieved with a 0.1 pF capacitor at the split region of the outer ring. To reduce ω_m down to 2.86 GHz, a capacitor with capacitance value between 0.2-0.4 pF is required to be loaded at the inner ring's split region. Instead of mounting varactors at the gap region, putting them at the split regions should result in higher tunability ranges for SRR structures. The highest tunability range is achieved with capacitors at the outer ring's split region.

It is worth mentioning at this point that by loading capacitor at the split region of the outer ring with a value of C = 2.2 pF, we managed to obtain ω_m at 0.99 GHz. To our knowledge, this is the highest reduction of resonance frequency of SRR. The diameter of the SRR structure is 7.2 mm and the free-space wavelength at 0.99 GHz is 303 mm. Therefore magnetic resonance is achieved by using a subwavelength structure with a size of λ/42.

Chapter 3

Negative Index Metamaterials

3.1. Introduction

Metamaterials have become a remarkable research area in recent years and received burgeoning interest due to their unprecedented properties unattainable from ordinary materials. Generally speaking, the dielectric permittivity (ε) and the magnetic permeability (μ) are both positive for natural materials. In fact, it is possible to obtain negative values for ε and μ by utilizing proper designs of metamaterials. To be specific, negative permittivity values at microwave frequencies are accessed by making use of thin metallic wire meshes [80-82]. It is rather difficult to obtain negative permeability due to the absence of magnetic charges. Pendry *et al.* came up with a brilliant solution and employed an array of split ring resonators exhibiting negative effective permeability (μ_{eff}) values for frequencies close to the magnetic resonance frequency (ω_{m}) of the split ring resonators [3]. The first steps to realize these novel type of materials were taken by Smith *et al.*, where they were able to observe a left-handed propagation band at frequencies where both dielectric permittivity and magnetic permeability of the composite metamaterial are negative [1, 40]. Soon after, left-handed metamaterials

with an effective negative index of refraction are successfully demonstrated by various groups [10, 43, 45, 50].

In this chapter, we investigate the transmission, reflection and refraction properties of such metamaterials comprised of split-ring resonator and wire arrays yielding left-handed electromagnetism.

3.2. Left-handed metamaterials: Transmission properties

In this section we study the transmission properties of left-handed metamaterials composed of periodic SRR and wire arrays as shown in Fig. 3.1(a).

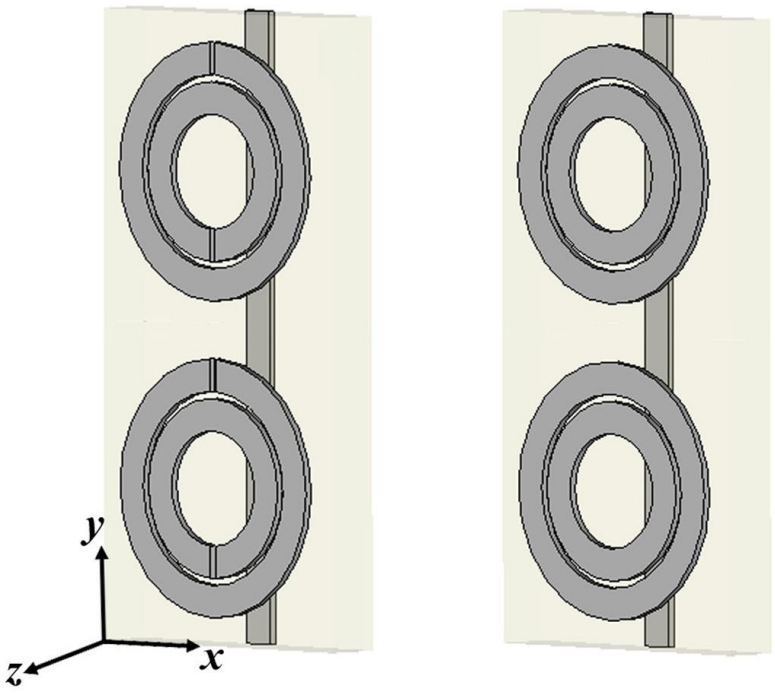

Figure 3.1 (a) A layer of 1D LHM composed of SRR and wire arrays, and (b) composite metamaterial (CMM) composed of CRR and wire arrays.

3.2.1. Negative permittivity

The electromagnetic response is dominated by negative permittivity concept in the visible and UV frequency regions. However, at lower frequencies starting from the near infrared and downwards, dissipation asserts itself, therefore dielectric function becomes imaginary. To achieve negative permittivity values at microwave range, the thin metallic wire concept is proposed [80-82].

By assembling thin metallic wire structures into a periodic medium with appropriate parameters, negative permittivity can easily be achieved at microwave frequencies. Plasma frequency of the thin metallic wires is given after detailed calculations as [80]

$$\omega_p^2 = \frac{ne^2}{\varepsilon_0 m_{eff}} = \frac{2\pi c_0^2}{a^2 \ln(a/r)} \tag{3.1}$$

where c_0 is the speed of light in free space, a is the lattice parameter and r is the radius of the wires.

The metallic wires were structured on a scale much less than the wavelength of radiation. When the wavelength of the incident radiation is much larger than the size and spacing of a collection of scatterers, the response of the scatterers to the incident fields can be treated by way of the effective medium theory.

$$a << \lambda = 2\pi c_0 \omega^{-1} \tag{3.2}$$

In the thin wire case, the effective medium theory holds since corresponding λ for ω_p is much larger than the radius of the wires. Therefore, an effective dielectric permittivity, ε_{eff} can be used to define the permittivity of the medium. As far as external electromagnetic radiation is concerned, a thin wire structure appears as an

effectively homogeneous dielectric medium whose internal structure is only apparent as it dictates ε_{eff}.

To demonstrate the negative permittivity concept we constructed a periodic array of thin wire structures. The length and width of the continuous thin wire structures are l = 19 cm, and w = 0.9 mm. The array is formed with N_x = 5, N_y = 15, and N_z = 32 unit cells, with lattice spacings $a_x = a_y$ = 8.8 mm and a_z = 6.5 mm [46]. Red line in Fig. 3.2 displays the transmission spectra of a thin-wire media. The plasma frequency is located at 8.0 GHz, below which the EM waves are not transmitted since the permittivity is negative.

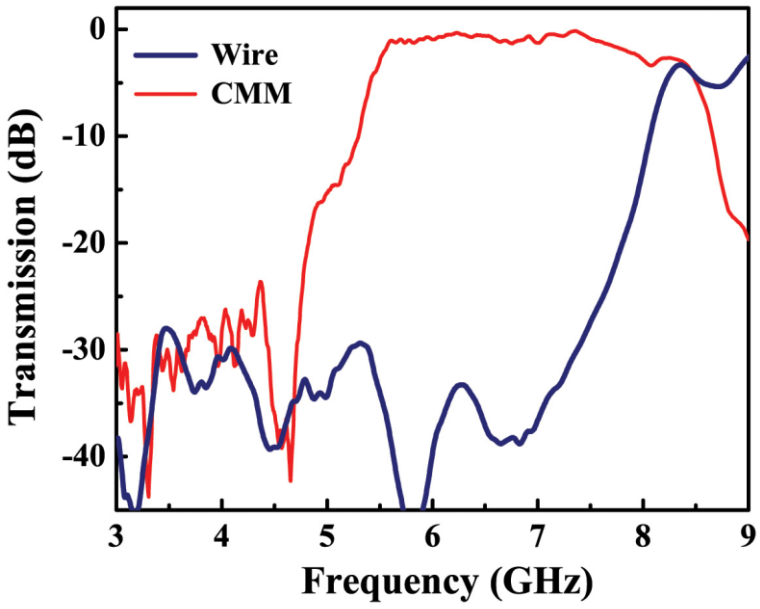

Figure 3.2: Measured transmission spectra of periodic wire (blue line), and CMM (red line) arrays.

SRRs, in addition to their resonant magnetic response at ω_m, exhibit a resonant electric response at ω_0. This behavior is similar to the electric response of a system of cut-wires (wires of finite length) which exhibits a stop band with a well-defined

lower edge due to the discontinuous nature of the wires. The SRR structures contribute to the effective permittivity of the CMM, causing a downward shift on the plasma frequency determined solely from wire structures. To demonstrate this effect, a CMM consisting of periodic alternating layers of CRRs and wires is used (Fig. 3.1(b). Thickness, length and the width of the wires are 30 μm, 19 cm and 0.9 mm respectively. While the plasma frequency of the wire-only structure is around 8 GHz, the plasma frequency is reduced down to 5.3 GHz for the CMM structure since both CRRs and wires respond together to electric field. As one can see from Fig. 3.2, the plasma frequency of the CMM is much lower than that of the wires alone. Therefore it is important to determine whether the shift in plasma cut-off frequency covers the magnetic resonance gap, which would render the CMM as a right-handed medium. This effect must be taken into account in left-handed metamaterial designs.

3.2.2. Left-handed metamaterial

Left-handed metamaterials are composite structures in which the electromagnetic response is determined by effective electromagnetic parameters. Left-handed behavior is achievable with the combination of structures that give rise to negative permittivity and negative permeability separately. In this work, we combined thin wire media providing negative permittivity and SRR array providing negative permeability to obtain a metamaterial with left-handed electromagnetism. A schematic drawing of a left-handed metamaterial sample is provided in Fig. 3.1(a). The length and width of the continuous thin wire structures are l = 19 cm, and w = 0.9 mm. The left-handed material is composed of N_x = 5, N_y = 15, and N_z = 32 unit cells, with lattice spacings a_x = a_y = 8.8 mm and a_z = 6.5 mm. Note that the lattice spacings are kept same with the lattice spacing of only split ring resonator medium studied in the previous section.

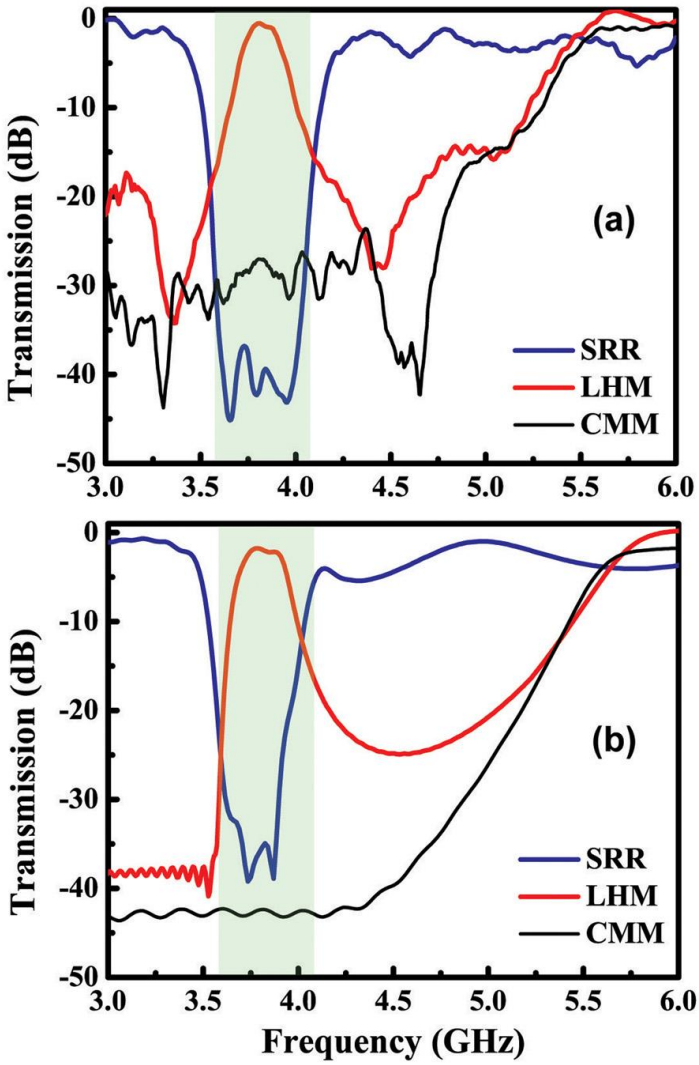

Figure 3.3: Transmission spectra of periodic SRR (blue line), LHM (red line) and CMM (black line) arrays obtained from (a) measurements and (b) numerical simulations.

Figure 3.3(a) depicts the measured transmission spectra of SRR (blue line), LHM (red line) and a composite metamaterial (CMM) composed of CRR and wire arrays (black line) with 5 unit cells along the propagation direction. The band gap in the transmission spectrum of SRR between 3.55-4.05 GHz is shown to be due to magnetic resonance in the previous section, therefore effective magnetic

permeability is negative within this frequency range. The plasma frequency of the CRR and wire array that is used to construct the left-handed material is shown to be at 8.0 GHz in the previous section. Therefore below 8.0 GHz, the effective permittivity of wire array is negative. The condition for the formation of left-handed transmission band is that the effective ε and μ should be simultaneously negative at a particular frequency range. As seen in Fig. 3.3(a), a transmission band (shaded region in the figure) is observed between 3.55 and 4.05 GHz. The transmission peak is measured to be -0.8 dB at 3.86 GHz. This is the highest transmission peak measured for a LHM structure.

For the composite metamaterial of CRR and wire arrays, the transmission band disappeared. We indicated that the wire media has plasma frequency around 8 GHz. SRR and CRR structures have also electric responses and therefore contribute to the total electric responses of the composite systems (LHM and CMM). Resulting LHM has a plasma frequency around 5.3 GHz, therefore the plasma frequency is reduced down. We performed numerical simulations to check the validity of the experimental results. Numerical simulation results are provided in Fig. 3.3(b) and predict the left-handed transmission band with peak value of -2.7 dB between 3.60 - 4.10 GHz.

3.3. Reflection properties of left-handed metamaterials

In this section we present the reflection measurements of a 1D LHM structure. In the measurements transmitter and receiver horn antennas were placed close to each other by keeping the angle between the antennas very small. The transmitter horn antenna sends the EM wave to the first surface of the structures and the receiver antenna measures the amplitude of the reflected EM waves. We used two different LHM structures with 5 and 10 layers along the propagation direction.

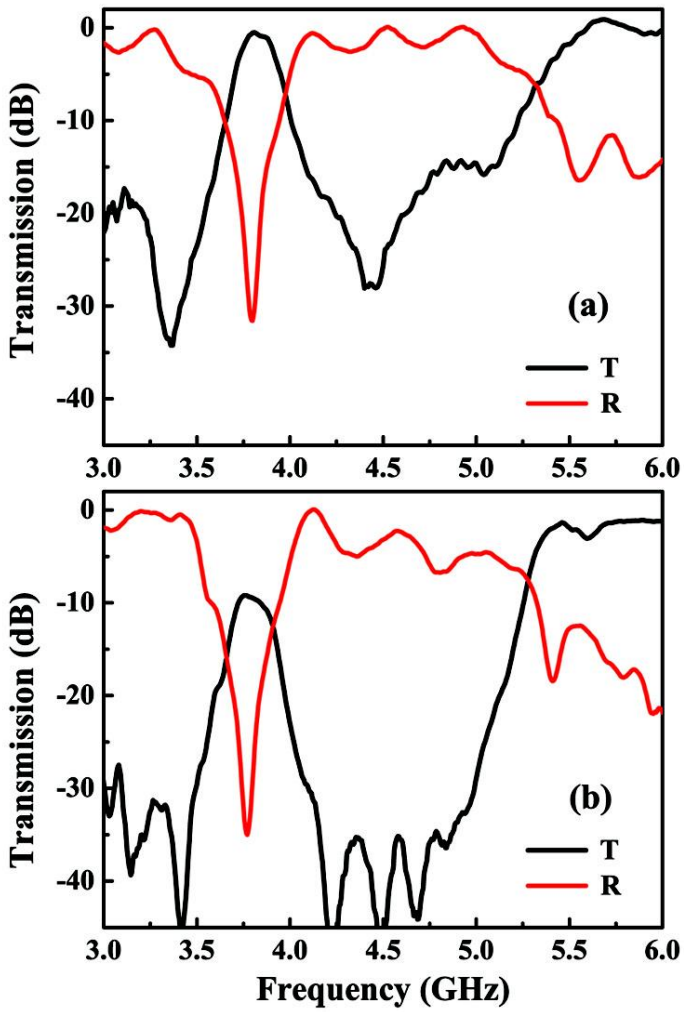

Figure 3.4: Measured transmission (black line) and reflection (red line) spectra of (a) 5 layer and (b) 10 layer 1D LHM.

Figure 3.4(a) plots the measured transmission and reflection spectra of a 5-layer LHM [66, 83, 84]. In the reflection spectrum, we observed a sharp dip at 3.79 GHz with a minimum value of -31.2. Figure 3.4(b) shows the measured transmission (black line) and reflection (red line) spectra for 10-layer 1D LHM. The transmission peak is measured to be -9.2 dB at 3.76 GHz. Expectedly, as the number of layers along the propagation direction increases, the transmission within

the left-handed transmission band decreases due to the losses. The minimum reflection is measured to be -35.0 dB at 3.77 GHz. The incident EM waves with frequencies around 3.77 GHz are almost transmitted through the left-handed material without being reflected at the left-handed material-air interface. The low reflection from the surface can be attributed to either matched impedance at the interface or to the thickness resonance of the slab. In the next section, we will show by extracting the effective parameters using retrieval procedure, that the impedance is matched to the free space. Impedance matching is desired for NIM structures, since it is required to achieve a perfect lens.

To provide a comparison, reflection spectra of two different numbers of layers are plotted in Fig. 3.5(a). The solid line is the reflection spectrum of 5 layers, whereas the dashed-dotted line corresponds to that of a 10-layer LHM structure. The dip at the reflection spectrum of LHM with 5 layers is measured to be at 3.79 GHZ with a dip value of -31.2 dB. The frequency where the reflection dip is observed nearly did not change although the structure's thickness is reduced by half. Therefore, the impedance matching cannot be due to the thickness resonance.

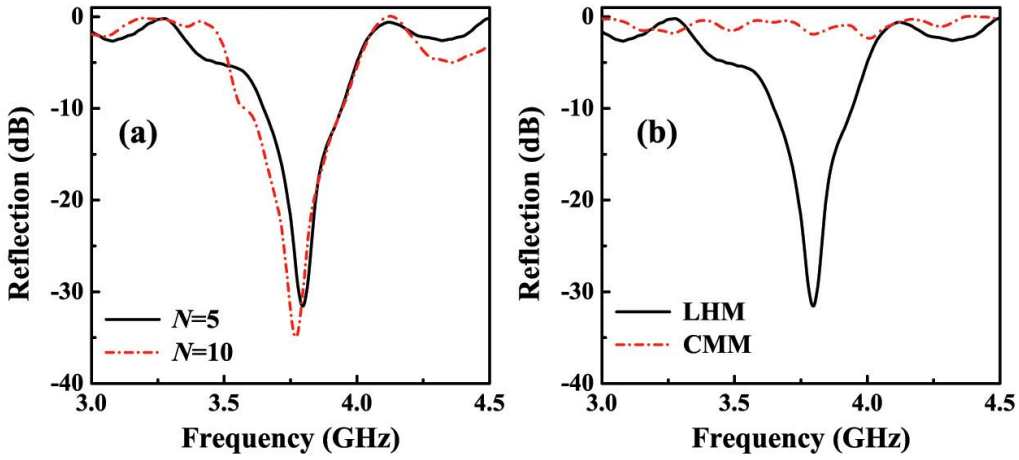

Figure 3.5: Measured reflection spectra of (a) 5 and 10 layers 1D LHM, (b) reflection spectra of 5 layers LHM and CMM structures.

We claim that this very low reflection from the surface LHM is due to the impedance matching between air and LHM. The impedance of LHM will be equal to that of free space if the real parts of ε and μ are equal. As seen in Fig. 3.5(a), the impedance matched frequency range (low reflection regions) is narrow. It is not surprising to have such a small range for an impedance matched frequency region, since μ_{eff} of SRRs is known to vary rapidly between the magnetic resonance (ω_{mo}) and magnetic plasma frequencies (ω_{mp}), although ε_{eff} of wires varies slowly throughout the frequency spectrum.

We also performed reflection measurements on a composite metamaterial (CMM) where the SRR structure was replaced with two concentric rings without splits (Fig. 3.1(b)). The left-handed transmission band is no longer present for the CMM case, because the magnetic permeability is positive due to lack of magnetic resonance. The measured reflection spectrum of CMM is shown in Fig. 3.5(b) with a dashed-dotted line. The CMM structure reflects most of the incident EM waves throughout the frequency spectrum. However, the EM waves incident to the LHM structure around 3.77 GHz are nearly transmitted through the LHM without being reflected at the surface. This measurement indicates that the negative permeability of SRRs is responsible for the dip in the reflection spectrum of LHMs.

3.4. Retrieved effective parameters

Dielectric permittivity, $\varepsilon = \varepsilon' + i\varepsilon''$ and magnetic permeability, $\mu = \mu' + i\mu''$ are used to describe the response of materials to the incident electromagnetic field; where ε' and μ' are the real parts, ε'' and μ'' are the imaginary parts of the corresponding effective parameters. Retrieval procedure is widely used to extract the effective parameters of metamaterial structures [68, 85-90]. The effective parameters of the NIM are retrieved by using the calculated amplitudes and phases of transmission and reflection. We have employed the retrieval procedure to obtain

effective parameters Z_{eff}, n_{eff}, ε_{eff}, and μ_{eff} by following the approach outlined in Ref. [68]. The advantage of this procedure is that the correct branch of the effective refractive index and effective impedance was selected. The ambiguity in the determination of the correct branch is resolved by using an analytic continuation procedure.

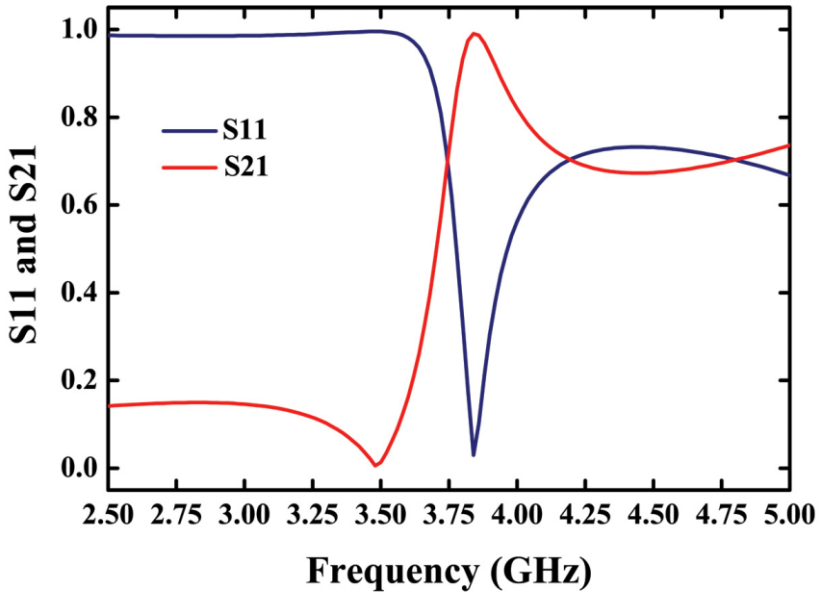

Figure 3.6: Simulated S-parameters for 1D LHM.

The S parameters are simulated by using HFSS, a full-wave electromagnetic software whose accuracy has been verified earlier. For the HFSS simulations, a single unit cell is simulated along the *x* direction, with periodic boundaries applied along the *y* and *z* directions. Hence, the simulation setup coincides with a slab of LHM that consists of a single layer. The effective permittivity and permeability values were then derived from the transmission and reflection coefficients of the single layer of LHM. Transmission (red line) and reflection (blue line) spectra of a single unit cell of LHM are plotted in Fig. 3.6. The transmission peak and the reflection dip appear at 3.85 GHz.

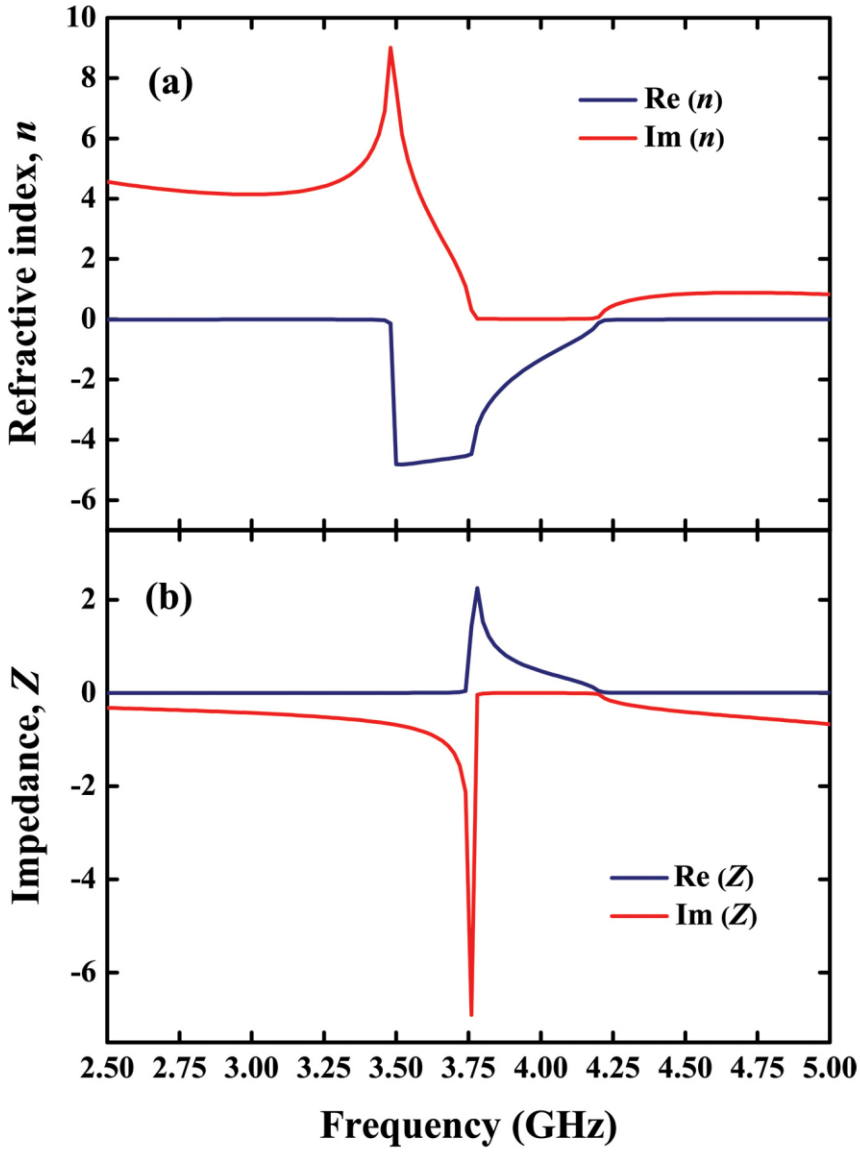

Figure 3.7: Simulated real and imaginary parts of effective (a) refractive index, and (b) impedance for 1D LHM.

These data together with the calculated transmission and reflection phase data are used to extract the effective index and effective impedance of the LHM media. Real (blue line) and imaginary (red line) parts of the effective refractive index is given in Fig. 3.7(a). Refractive index possesses negative values between 3.50 and 4.20 GHz. This frequency region coincides with the left-handed transmission band

observed from the measurements and CST simulations. Figure 3.7(b) shows the real (blue line) and imaginary (red line) parts of the effective impedance of the composite LHM.

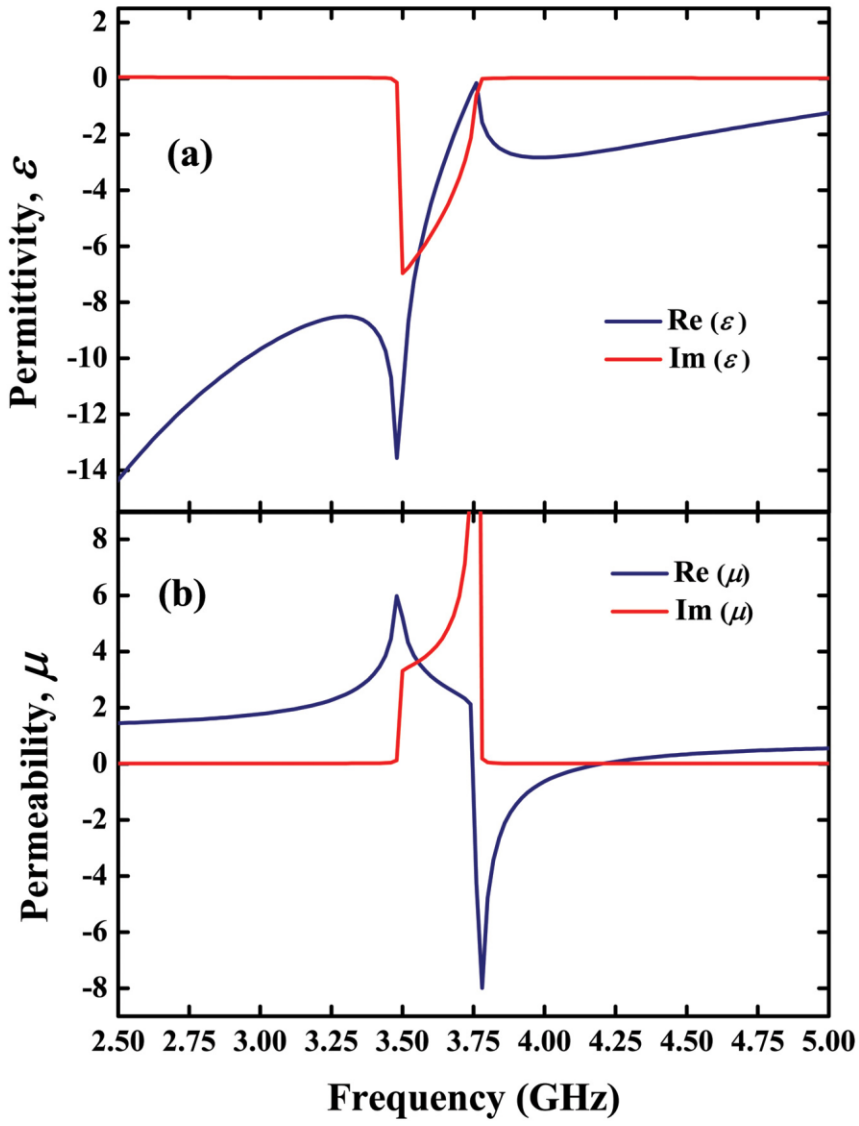

Figure 3.8: Simulated real and imaginary parts of effective (a) dielectric permittivity and (b) magnetic permeability.

Once we find the effective index and impedance of the system, the effective permittivity and permeability can be calculated by using the relations, $\varepsilon = n/z$ and $\mu = nz$. We plotted the real (blue line) and imaginary (red line) parts of the effective permittivity and permeability of the medium in Fig. 3.8(a) and 3.8(b), respectively. Expectedly, the dielectric permittivity of the composite medium is negative below the plasma frequency. Near the resonance frequency of SRR (3.85 GHz), the form of permittivity deviates from the Drude model. The effective permeability possesses both positive and negative high values around the magnetic resonance frequency. Permeability is negative between 3.75 and 4.20 GHz.

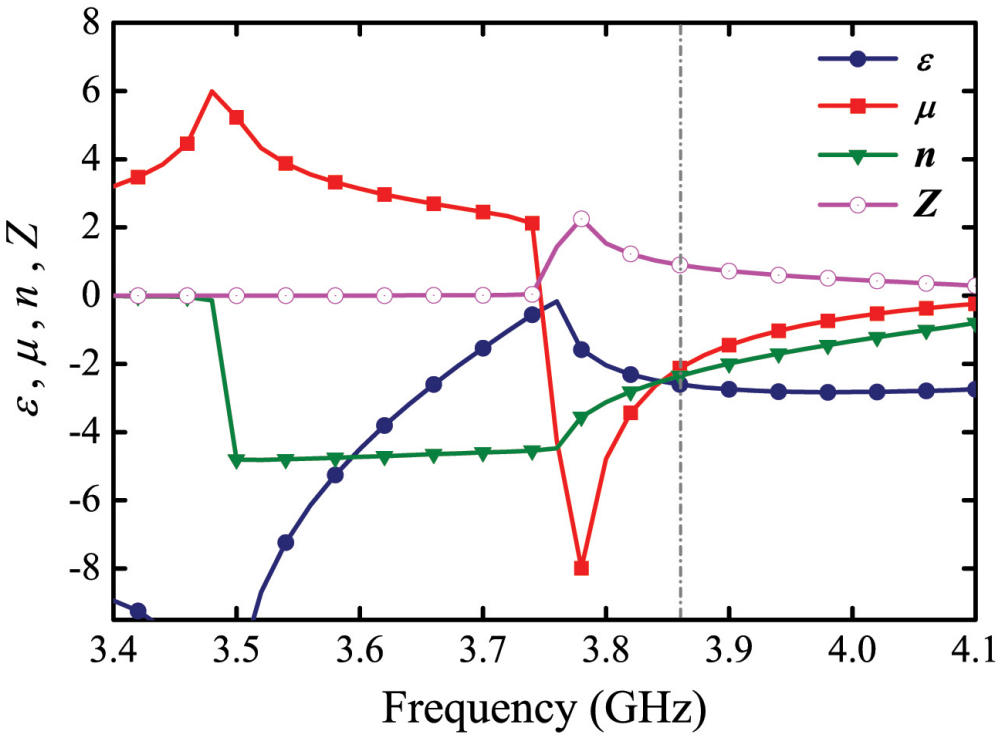

Figure 3.9: Simulated real parts of effective permittivity, permeability, refractive index and impedance. Dashed gray line corresponds to the frequency region where ε = μ, therefore the impedance is Z=1.

For a better interpretation of the retrieved effective parameters, we plotted the real parts of effective permittivity, permeability, refractive index and impedance in Fig. 3.9. ε' and μ' possess negative values between 3.75 and 4.20 GHz. The minimum reflection in the simulations occurs at 3.85 GHz, where $\varepsilon' = \mu' =$ -2.45 (dashed gray line). The impedance is defined as $Z = \sqrt{\mu'/\varepsilon'}$, therefore impedance matching is obtained when $\varepsilon' = \mu'$. This frequency corresponds to the minimum of the reflection spectrum, therefore impedance of LHM is matched to that of free-space at 3.85 GHz (dashed line in Fig. 6), where Z'=1.

The reflection coefficient of an EM wave for the electric field perpendicular to the plane of incidence case:

$$r = \frac{\sqrt{\frac{\varepsilon_0}{\mu_0}}\cos\theta_i - \sqrt{\frac{\varepsilon_1}{\mu_1}}\sqrt{1-\left(\frac{n_0}{n_1}\right)^2\sin^2\theta_i}}{\sqrt{\frac{\varepsilon_0}{\mu_0}}\cos\theta_i + \sqrt{\frac{\varepsilon_1}{\mu_1}}\sqrt{1-\left(\frac{n_0}{n_1}\right)^2\sin^2\theta_i}}. \qquad (3.3)$$

In the above formula the EM wave is assumed to be incident from the air to the LHM surface with an incident angle of θ_i. The refractive index is given by $n = \sqrt{\varepsilon\mu}$ and the impedance of the medium is $Z = \sqrt{\mu/\varepsilon}$. For free-space ε_0=μ_0=1 and therefore n_0=1 and Z_0=1. For θ_i=0, the EM waves are normally incident to the LHM surface. Eq. (1) is reduced to:

$$r = \frac{Z_1 - Z_0}{Z_1 + Z_0}, \qquad (3.4)$$

where Z_1 is the impedance of the LHM, and Z_0 is the free-space impedance. It is obvious from the Eq. (3.4) that if the impedance of the LHM is matched to free-

space, the reflection coefficient will be zero. Naturally occurring materials are not matched to free-space. However, LHM has an advantage in achieving impedance matching since their effective permeability and permittivity are strongly frequency dispersive. One can control the permeability and permittivity of the LHM layer, and impedance matching can therefore be obtained.

The refractive index is, $n' = -2.45$ at 3.85 GHz. The imaginary part of the effective index is $n'' = 0.012$, meaning that the losses are small at the frequency of minimum reflection. The ratio of the absolute value of the real part of the index to its imaginary part is a figure of merit for negative-index metamaterials. For our metamaterial structure, figure of merit is calculated as $FOM = |n'| / n'' = 205$. The minimum reflection frequency is observed at 3.75 GHz in the measurements, however, in the simulations it appeared at 3.85 GHz. This frequency difference between the simulated and measured reflection spectrum may be attributed to fabrication tolerances and deviation from the ideal structure that may possibly caused by misalignments during the experiments.

3.5. Negative refractive index

In the previous two sections we performed transmission and reflection measurements to characterize the split-ring resonators and left-handed metamaterials. In this section we move on to the experiments to measure the refractive index of our sample at the left-handed frequency region. We performed three different and independent experimental measurements to verify that the index of refraction is negative. First, we measured refraction from a 2D wedge-shaped left-handed material structure. Then, we performed refraction experiments on slab-shaped LHM structures. Finally we performed a phase shift experiment to

verify and calculate the negative refractive index, which will be discussed section 3.6.

3.5.1. Refraction through wedge-shaped left-handed materials

A typical experimental method for the observation of left-handed properties is to use wedge-shaped structures [10, 43, 45, 50, 91]. In our experiments we used a prism-shaped (wedge) structure composed of 2D left-handed material (Fig. 3.10(a)). If we transmit EM waves to the first interface of the wedge sample as shown in, the incident beam will not be refracted at this surface, since it is normal to the surface (Fig. 3.10(b). The refraction will occur in the second interface of the wedge sample where the incident beam approaches the normal of the sample with an angle equal to the wedge angle. If the wedge sample has a positive refractive index, the beam will be refracted at the left side of the normal. However, if the wedge structure is constructed with a negative index material, refraction will occur at the other side of the normal corresponding to the right side of the normal.

Using the idea discussed above we constructed an experimental setup which is schematically drawn in Fig. 3.10(b). Two horn antennas are used in our experiments. The source is located 13 cm (~2λ) away from the first interface of the wedge. The receiver antenna is mounted on a rotating arm to obtain the angular distribution of the transmitted signal. The receiver antenna is located at a distance of 70 cm (~10λ) away from the second interface of the wedge. We measured the transmission in free space without the wedge sample in between, and used this data as a calibration. Then we inserted the sample and measured the transmission by rotating the receiver antenna with 2.5° steps.

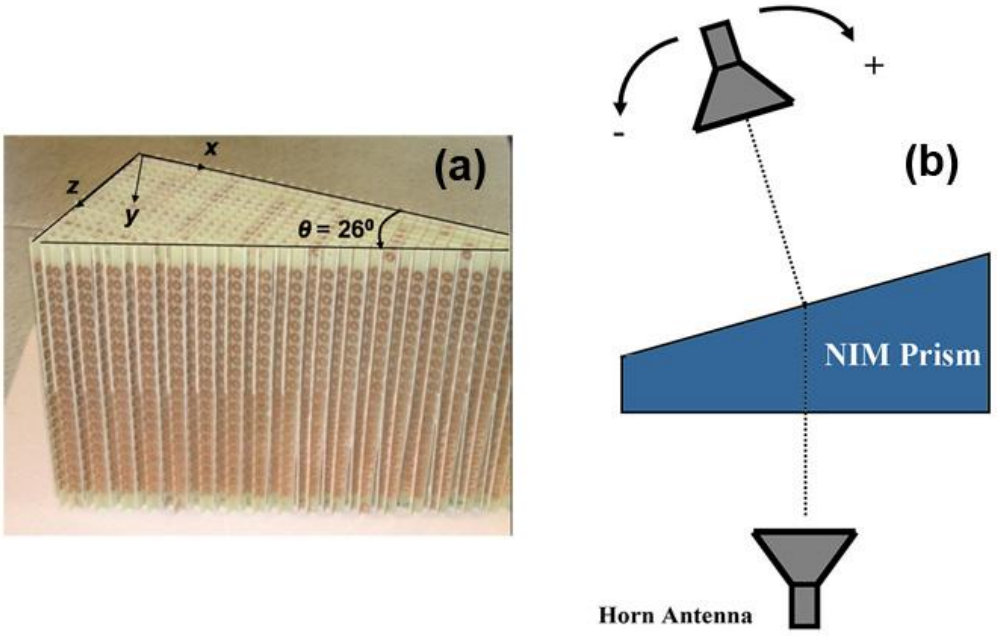

Figure 3.10: (a) Photograph of wedge-shaped NIM and (b) scheme of experimental setup for verifying negative refraction by wedge shaped NIM.

A wedge structure is constructed to test the negative refraction of 2D LHMs by cutting the boards and assembling them as shown in Fig. 3.10(a). Lattice spacings of the wedge are $a_x = a_y = a_z = 9.3$ mm. The minimum and maximum number of unit cells at the propagation direction is 3 and 19, respectively. So the average number of layers, also corresponding to the number of layers at the center of the wedge is 11 layers. 2 consecutive layers along the *x* direction have the same number of layers along *z* direction. Then the number of layers along the *z* direction is reduced by one. By using this two by one design, we obtained a wedge angle of $\theta = 26°$.

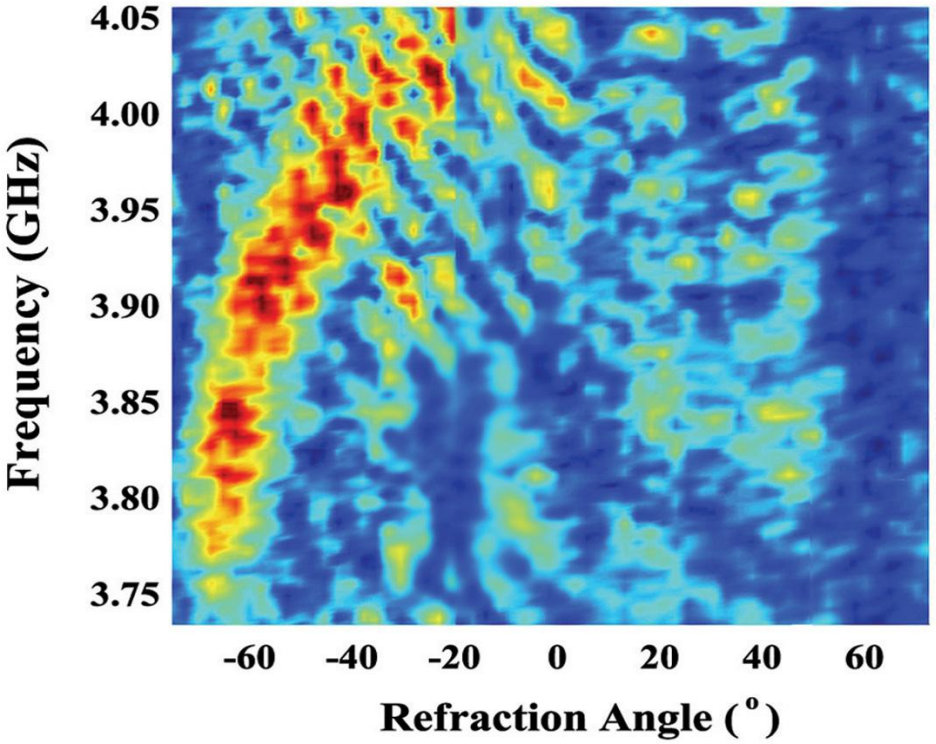

Figure 3.11: Measured beam profiles of the EM waves refracted from a 2D prism shaped LHM as a function of frequency and angle of refraction between 3.73 - 4.05 GHz.

The angular refraction spectrum is scanned by $\Delta\theta = 2.5°$ steps. Figure 3.11 displays the intensity spectrum as a function of frequency and refraction angle. It is evident from the figure that the transmitted beam is refracted on the negative side of the normal. As seen from Fig. 3.11, the incident beam is refracted with negative refraction angles between 3.73-4.05 GHz corresponding to the frequency regime where both permittivity and peremability are negative. If Fig 3.11 is analyzed in detail, it is clearly seen that refraction angle values, therefore negative refractive indices are not the same in all frequencies. At lower frequencies the EM waves are refracted at higher negative refraction angles, which results in a higher

negative refractive index. The refraction index is lowered if we go to higher frequencies.

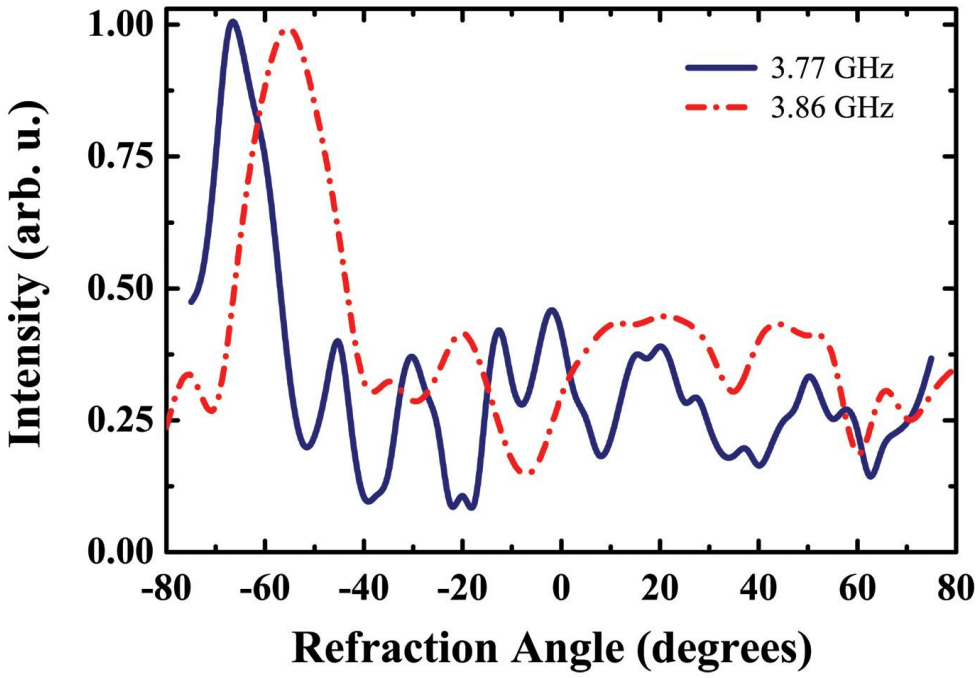

Figure 3.12: Measured beam profiles from the waves refracted from a wedge-shaped 2D left-handed material at 3.77 GHz (blue line) and 3.86 GHz (red line).

The refracted beam profiles from the NIM-air interface are shown in Fig. 3.12 for two different frequencies, 3.77 GHz (blue line) and 3.86 GHz (red line). At these frequencies, the beam is refracted on the negative side of the normal indicating that the angle of refraction is negative. The angle of the refraction at 3.77 GHz is measured to be θ_r = -65° and at 3.86 GHz θ_r = -60°. We can use Snell's law for calculating the n_{eff} of the 2D NIM structure by the simple formula $n_{eff} \sin\theta_i = n_{air} \sin\theta_r$. At 3.86 GHz the refractive index is calculated as n_{eff} = -1.98 ± 0.05. The angle of refraction increases when the frequency is lowered, hence the n_{eff} increases. The calculated refractive index at 3.77 GHz is n_{eff} = -2.07 ± 0.05.

3.5.2. Refraction through slab-shaped left-handed materials

In this section, we performed refraction experiments by using a slab-shaped LHM structure. The 2D LHM structure is composed of $N_x = 40$, $N_y = 20$, and $N_z = 10$ unit cells, with lattice spacings $a_x = a_y = a_z = 9.3$ mm (Fig. 3.13(a)). The refraction spectrum is measured by a setup consisting of HP 8510C network analyzer, a standard high gain microwave horn antenna as the transmitter, and a monopole antenna as the receiver (Fig. 3.13(b)). The size of the monopole antenna is 3.8 cm, that is the half of the wavelength of the EM wave at working frequency, f= 3.86 GHz.

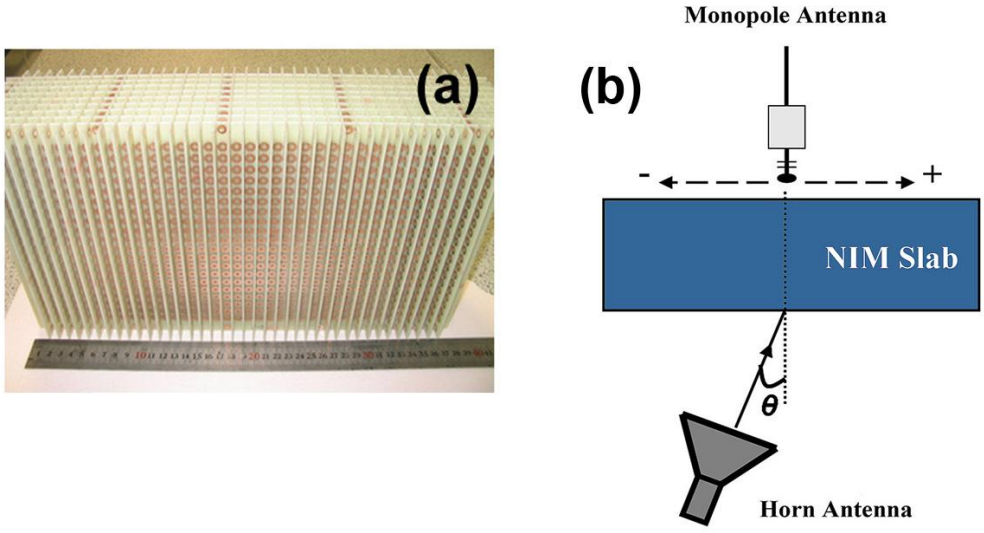

Figure 3.13: (a) Photograph of 10-layer NIM slab (b) Scheme of experimental setup for verifying negative refraction by using beam-shift method.

As seen in Fig. 3.13(b) the horn antenna is placed on the negative side (-x) of the LHM structure with respect to its central axis. The horn antenna is 125 mm (1.6λ) away from the first interface of LHM slab. FWHM of the beam at the interface is comparable to the wavelength and smaller than the size of the incident

surface (5λ). Plane wave is sent through the LHM slab with an incident angle of θ_i = 15°. The intensity distribution of EM wave is scanned by monopole antenna mounted to a 2D scanning table with $\Delta x = \Delta z = 2.5$ mm steps. In our experiments we can measure only the power at a certain point, which corresponds to the time averaged intensity at that point.

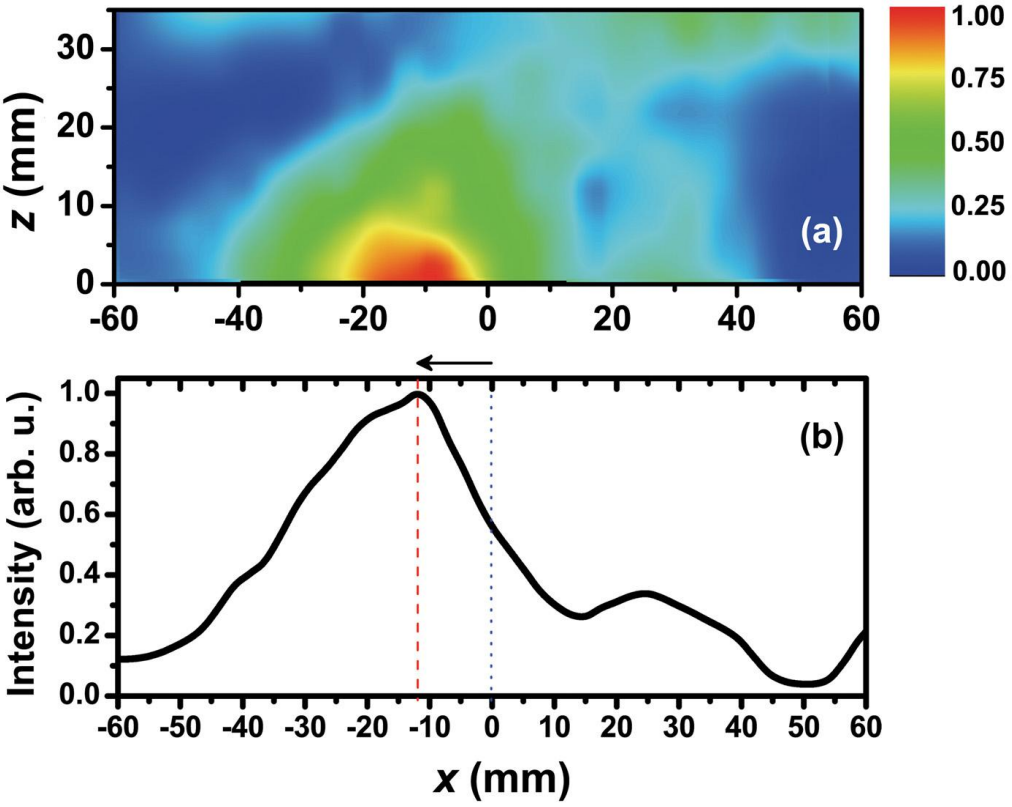

Figure 3.14: (a) Spatial intensity distribution of outgoing EM wave at 3.86 GHz along x-z plane. (b) Intensity profile of EM wave at the LHM-air interface (z = 0).

Figure 3.14(a) displays the measured refraction spectrum at 3.86 GHz. The intensities are normalized with respect to maximum intensity. The incident EM wave has a Gaussian beam profile centered at $x = 0$. Therefore by measuring the shift of the outgoing beam, one can easily deduce whether the structure has positive or negative index of refraction. As clearly seen in Fig. 3.14(a), the center

of the outgoing Gaussian beam is shifted to the left side of the center of the incident Gaussian beam, which due to Snell's law, corresponds to negative refraction. As expected, the angle between the normal and the outgoing beam should be equal to the angle of incidence. This angle is found to be 18^{o}, which is close to the $\theta_i = 15°$.

Figure 3.14(b) is the cross-section of Fig. 3.14(a) taken at $z = 0$, in other words it provides the intensity distribution of EM wave just at the LHM-air interface. As seen in Fig. 3.14(b), the center of the refracted Gaussian beam (red dashed line) is measured at -12.5 mm away from the center of the incident Gaussian beam (blue dotted line).

Snell's law is an effective method for calculating refractive indices. Since we know the amount of the beam shift (-12.5 mm) and the thickness of the LHM slab, $t = 91.2$ mm, angle of refraction is found to be $\theta_r \cong 8°$. Refractive index of LHM is then calculated from Snell's law ($n_{air} \sin\theta_i = n_{eff} \sin\theta_r$) as $n_{\text{eff}} = -1.86$.

3.6. Negative phase velocity

For materials with a negative refractive index, the phase velocity points toward the source that is the phase velocity and energy flow are anti-parallel inside a NIM [50, 92, 93]. By measuring the transmission-phases for NIMs with varying thicknesses, one can verify that the phase velocity is indeed negative [50]. HP 8510-C network analyzer is capable of measuring the transmission-phase. We have constructed 4 different 2D NIM slabs with number of layers $N_x = 5$, 6, 7 and 8. The transmitted phases are plotted in the frequency range 3.70-4.00 GHz, which is within the left-handed transmission region.

Figure 3.15 shows the transmitted phase for different number of layers of NIM slabs. It is evident from the figure that, increasing the number of layers of NIM results in a decrease at the phase of the transmitted EM wave. However, if

the material possesses a positive refractive index, one would observe an increase in the transmitted phase with the increasing number of unit cells [50].

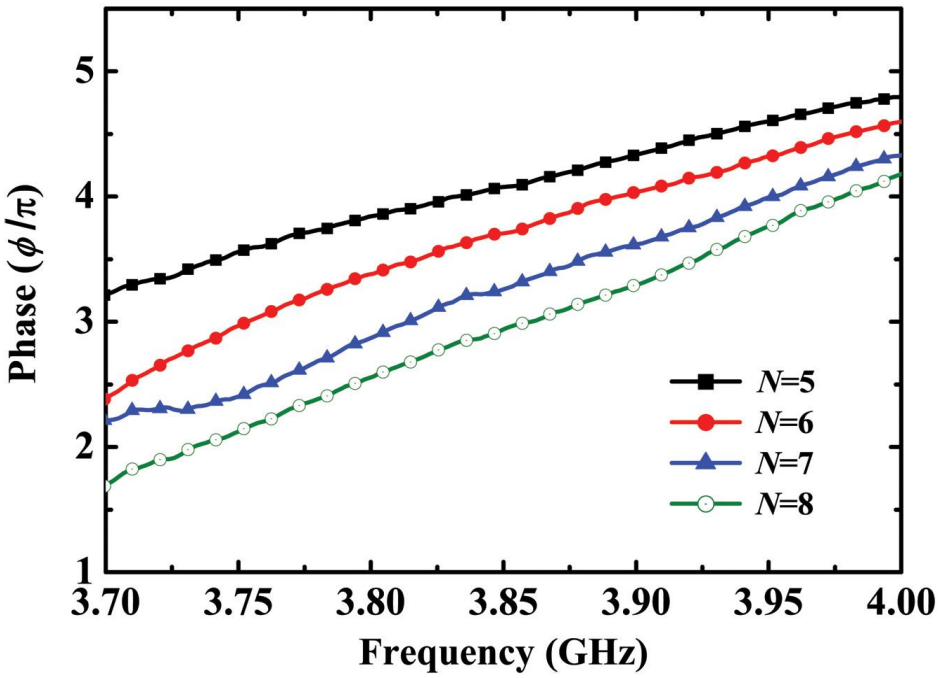

Figure 3.15: The measured transmission phase spectra of LHMs with 5, 6, 7 and 8 number of layers along the propagation direction.

The index of refraction in terms of wavelength, phase shift, and change in the length of left-handed material is given by [50]:

$$n = \frac{\Delta\phi}{\Delta L}\frac{\lambda}{2\pi} \tag{3.5}$$

At f=3.86 GHz, the wavelength of the EM wave is λ=7.77 cm. The average phase shift per unit cell (ΔL=8.8 mm) obtained from the experimental results is $\Delta\Phi$ = -0.45±0.04π. Inserting these values in (3.5), index of refraction at 3.86 GHz

is found to be n_{eff} = -1.98±0.18. The average phase shift and calculated refractive index for the numerical simulations at 3.77 GHz are $\Delta\Phi$ = -0.51±0.04π, and n_{eff} = -2.31±0.18.

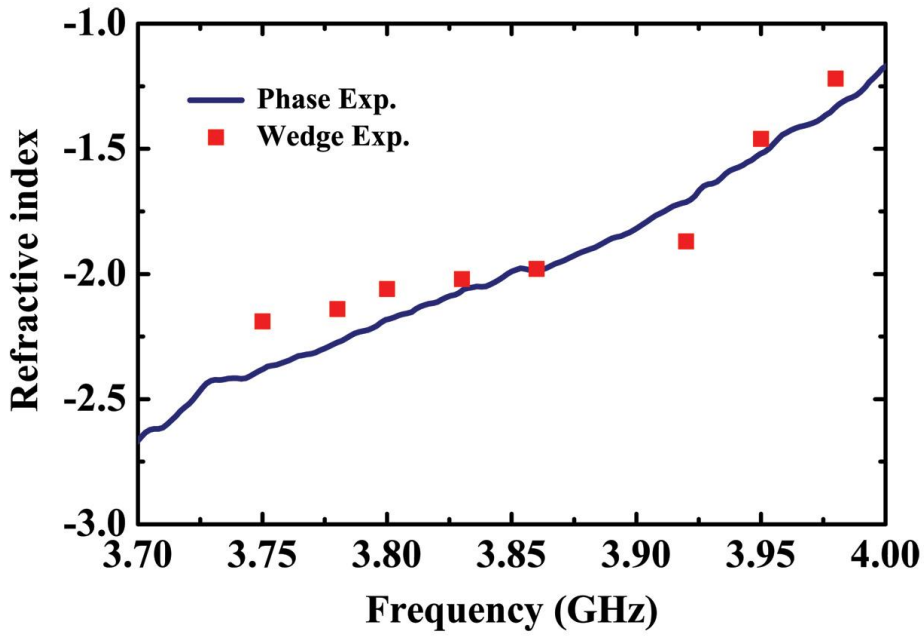

Figure 3.16: Measured effective refractive indices as a function of frequency obtained from the phase shift experiments (blue line) and prism experiments (■).

In Fig. 3.16, we plotted the refractive index values calculated by using the phase shift between the consecutive numbers of NIM layers. The symbol (■) corresponds to the refractive indices obtained from wedge experiments at some other frequencies. There is a good agreement between the results obtained from two different methods. We also found index of refraction at 3.86 GHz by using beam shift method as -1.91. The index of refraction values obtained from the wedge and the phase shift experiment are both -1.98 at this frequency. Therefore we have been able to show that the results obtained from three different experiments agree extremely well.

Chapter 4

Flat-lens focusing

4.1. Introduction

A negative refractive index allows a flat lens to bring EM waves into focus, whereas positive refractive index materials always require curved surfaces to focus EM waves [2, 18]. The presence of negative refraction enables the possibility that the slab structure may act like a lens for an omni-directional source. As described in detail in Ref. 18, a parallel-sided slab of material made of negative index metamaterial can focus EM waves. EM waves emerging from an omni-directional source located near such a lens will first be refracted through the first air-LHM interface and will come into focus inside the material. Then outgoing EM waves will face refraction again at the second LHM-air interface and the refracted beam will meet the optical axis of flat lens, where the second focusing will occur. If the lens is not thick enough, the focusing may not occur inside the lens, which in turn will result in a diverging beam instead of a converging beam, even if the material is negatively refracting. Therefore, the thickness of the lens plays a crucial role for observing flat lens behavior. Multi-focal flat lenses of LHMs [94], and planoconcave lenses of PCs [95] are used in other studies making use of the negative refraction concept for constructing an image.

In this chapter, we present results from research conducted on negative refraction and the flat lens behavior of LHMs. Our structure exhibits high transmission and low reflection at certain frequency ranges. An omni-directional source is placed at two different distances from the LHM lens, in which a clear image of the source is subsequently observed.

4.2. Point focusing by a NIM flat lens

We have employed a LHM lens with 40×20×10 layers along the *x*, *y* and *z* directions (Fig. 3.13(a)). Along the propagation direction (*z* direction) the structure has 10 unit cells, and the thickness is t = 91.2 mm. The top view of the experimental setup for verifying focusing through a flat lens of LHM is schematically given in Fig. 4.1. A monopole antenna is used as the point source. The source is located away from the LHM lens at two different source distances of $d_s = 0.5\lambda$ and $d_s = \lambda$. The intensity distribution of an EM wave is scanned by another monopole antenna with $\Delta x = \Delta z = 5$ mm steps.

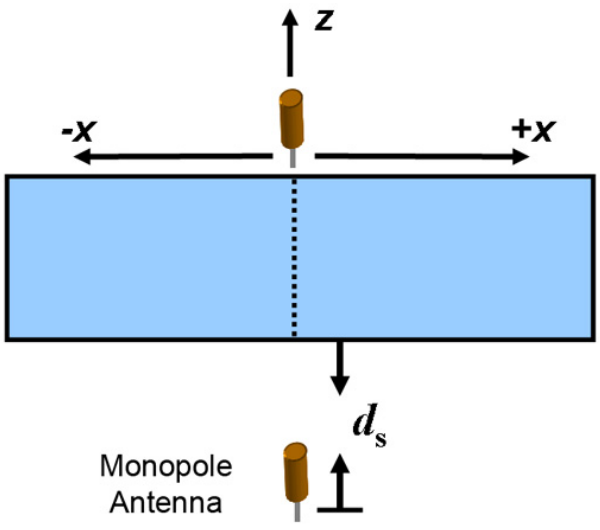

Figure 4.1: Schematic drawing of the top view of experimental setup for verifying flat lens focusing.

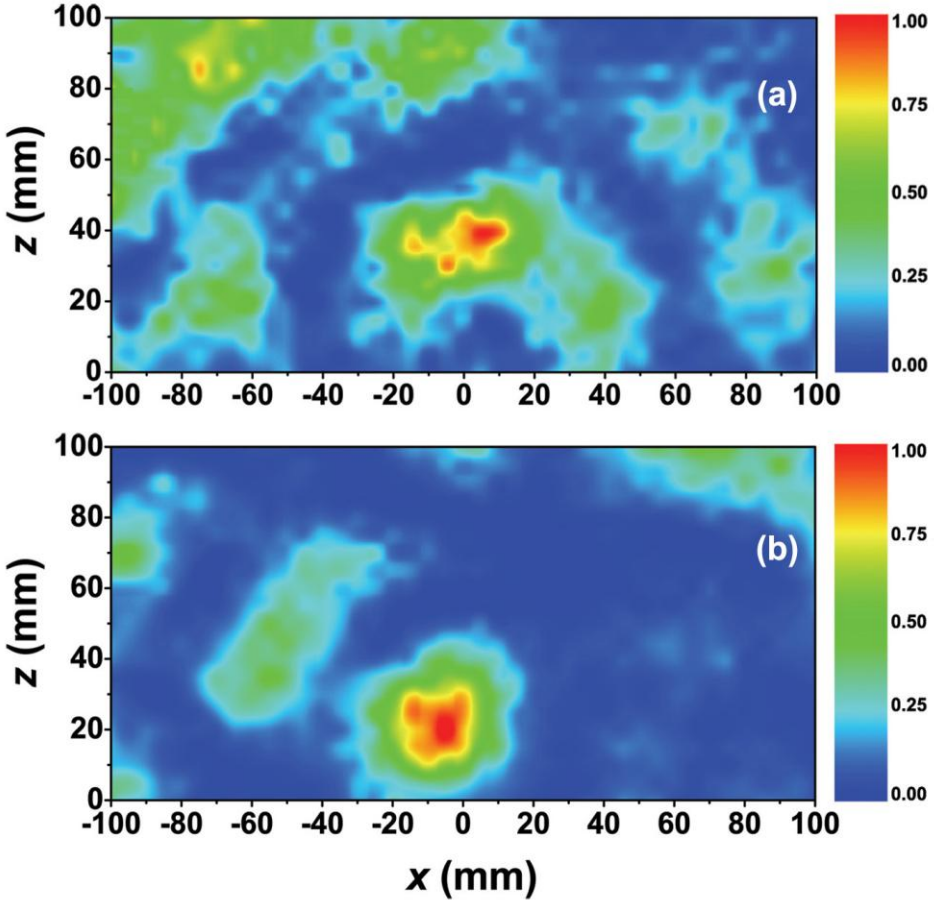

Figure 4.2: Measured transmission spectra along the x-z plane for a point source located at (a) $d_s = 0.5\lambda$, and (b) $d_s = \lambda$ away from the LHM lens. The x direction is parallel to the LHM lens where x = 0 is the optical axis of the flat lens, whereas the z direction is perpendicular to the LHM lens where z = 0 is the LHM-air interface.

The measured intensity spectra are shown in Fig. 4.2, with the intensities normalized with respect to the maximum intensity values. The point $z = 0$ corresponds to the LHM-air interface. Figure 4.2(a) provides the intensity distribution for the omni-directional source located at $d_s = \lambda/2$ away from the LHM lens. As seen in the figure, an image is formed at a focal length of z = 40 mm (~0.52λ). For the case where the point source is placed at $d_s = \lambda$, the image is

observed at z = 20 mm (~0.26 λ) (Fig. 4.2(b)). As the point source is moved away from the LHM flat lens, the focal length is shifted towards the flat lens, which is consistent with imaging theory.

Figure 4.3 depicts the intensity distribution of the focused EM wave along the longitudinal (z) direction taken at $x = 0$, for the source distances of $d_s = \lambda/2$ and $d_s = \lambda$. The focal length moves towards the flat lens for larger source distances.

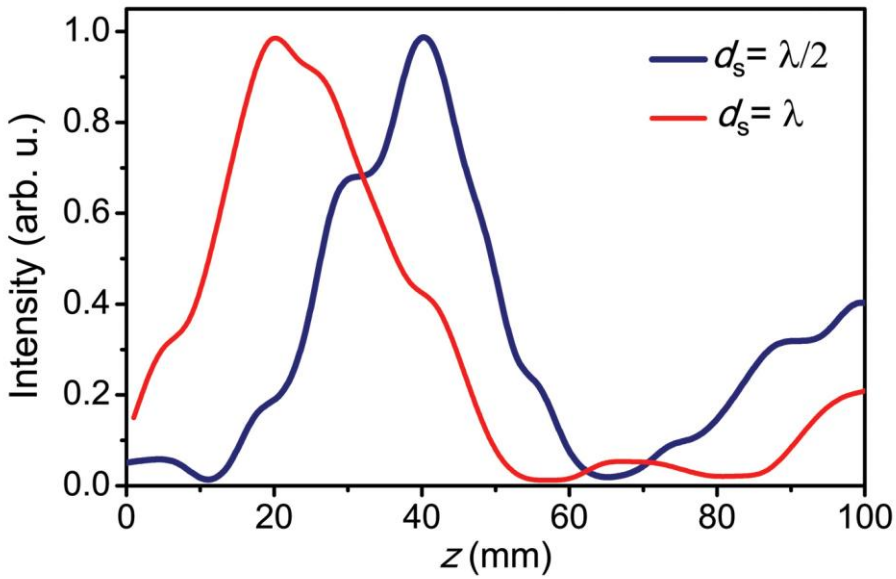

Figure 4.3: Intensity profile of the focused EM waves at x = 0 point along longitudinal direction

Figure 4.4 displays the lateral intensity profile of the focused EM waves at the focal lengths z = 40 mm for $d_s = \lambda/2$ and z = 20 mm for $d_s = \lambda$. It is evident from Figs. 4(a) and 4(b) that the EM wave is focused in the longitudinal and lateral directions. FWHM of the focused beams along the longitudinal direction are ~0.3λ, for both source distances. From the intensities along the lateral direction, FWHMs are found to be 0.4λ and 0.36λ for the source distances $d_s = \lambda/2$ and $d_s = \lambda$, respectively, which are below the diffraction limit. Since the material used to construct the flat lens has a negative refractive index, the evanescent waves are

enhanced inside the lens subsequently enabling sub-wavelength imaging. As seen in Fig. 4(b), when the focal length is closer to the lens (as the case for $d_s = \lambda$), the contribution of the evanescent waves to focusing is higher, which in turn results in better sub-wavelength resolution (0.36λ).

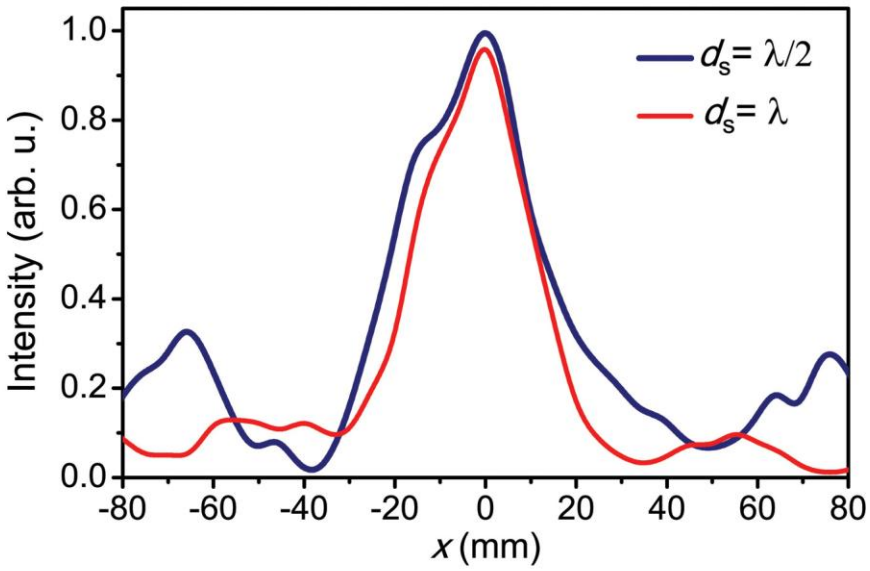

Figure 4.4: Intensity profile of the focused EM waves at the focal points of each source along the lateral direction. The graphs are for the point source located at λ/2 (black) and λ (red) away from the air-LHM interface.

LHM structures are all-angle negatively refracting materials, since the effective refractive index of these structures is determined by the effective material parameters, dielectric permittivity and magnetic permeability. All-angle negative refraction is essential for focusing the beam diverging from a point source. Another crucial point is that the lens should not suffer much from the reflections at the LHM-air interface. The advantages of our flat lens in a nutshell are that: (1) The lens is constructed from an all-angle negative refractive index LHM slab, (2) it operates at a frequency where the transmission is at the maximum and the reflection is minimum, assuring that the experimental results are not any artifact of the reflections from the surface, (3) it is working in free space rather than an

isolated waveguide environment, and (4) it enables sub-wavelength focusing by virtue of the negative refractive index.

4.3. Electromagnetic wave focusing from sources inside a NIM flat lens

In the previous section, we have observed flat lens behavior from the sources located outside of the LHM lens. In this section, we investigated the focusing behavior of a flat lens where the omni-directional source is embedded inside the LHM slab. The focusing behavior was previously observed inside LHM lenses experimentally [96]. We followed a different approach here. We chose to put the source inside the LHM lens and measure the field intensity outside the lens. This section is divided into two subsections. We first shall discuss the flat lens behavior, where the lens focuses the incident EM wave in the lateral and longitudinal directions. Secondly, we will present our experimental observation of subwavelength imaging (superlens behavior) near the LHM lens at the frequency where the LHM sample has the lowest reflection value.

In the focusing experiments a slab-shaped LHM lens with 40×20×10 layers along the *x*, *y* and *z* directions is used. The top-view of the LHM lens is provided in Fig. 4.5. Along the propagation direction (*z* direction) the structure has 10 unit cells, in which the thickness is t = 90.9 mm. The periodicity along the *z*-direction, as well as along the *x* and *y* directions is $a_z = a_x = a_y$ = 9.3 mm. We used monopole antennas as the point source. We embedded the source inside the LHM lens at different locations. We chose routinely to identify the position of the source in terms of the number of layers (N_s).

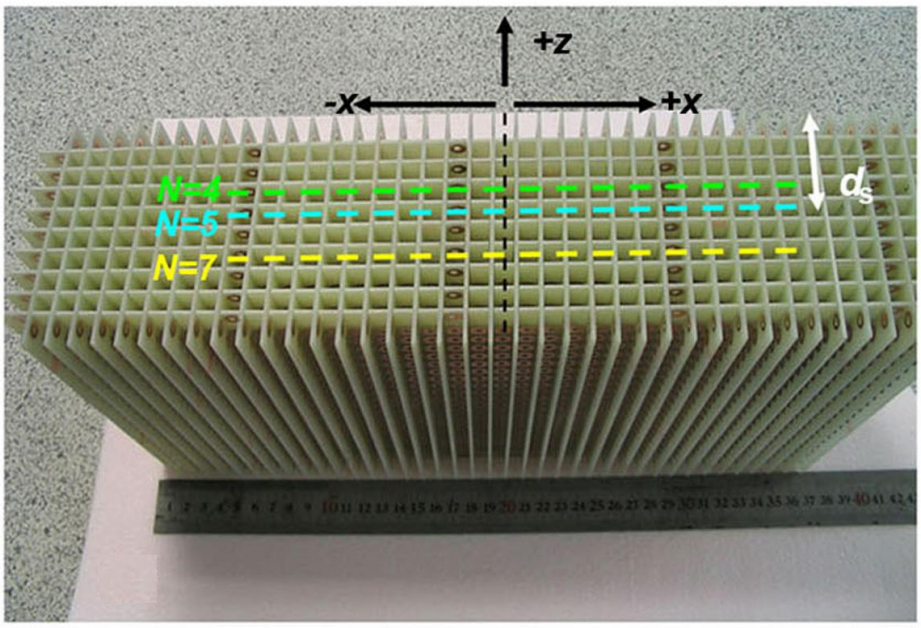

Figure 4.5: LHM slab lens with 10 unit cells along the propagation direction (z-axis).

In Fig. 4.5 colored dashed lines show the axis of the sources, which are d_s away from the LHM-air surface. The distance of the source to the LHM-air interface can be given by the formula d_s=9.3(N_s-1)+r, where r = 3.6 mm is the radius of the SRR. The intensity distribution of an EM wave is scanned from the surface by another monopole antenna with $\Delta x = \Delta z$ = 2.5 mm steps. In the experiments, we can solely measure EM field intensity at a point.

4.3.1. Flat lens behavior

Figure 4.6(a) and (b) depicts the spatial intensity distribution of the outgoing EM waves from the sources embedded inside the layers N_s = 5 and N_s = 7 at 3.89 GHz. The intensities are normalized with respect to the maximum intensity values. For both cases, we observed focusing along the longitudinal and lateral directions. However, there is a change at the focal point, when the location of the source is

changed. The EM waves are focused at z = 10 mm and z = 15 mm for the sources at the fifth and seventh layers. As the point source is moved away from the LHM-air surface, the focal length is increased, which is consistent with the imaging theory.

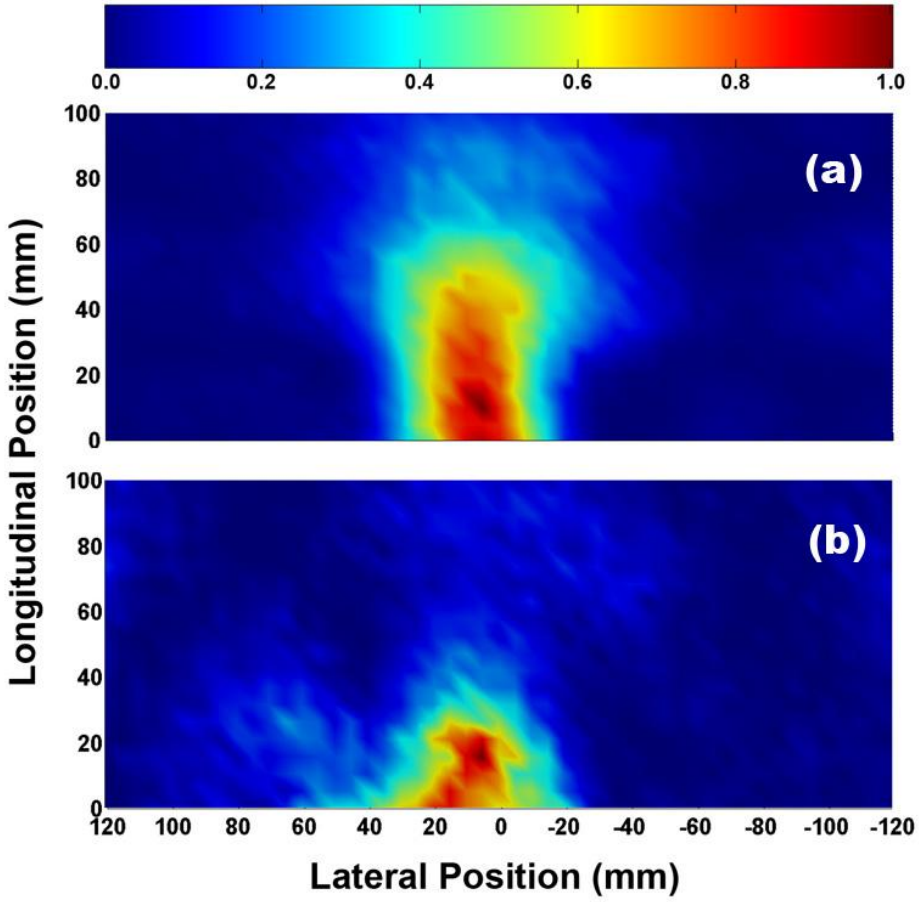

Figure 4.6: The spatial intensity distribution of the outgoing EM waves from the sources located inside the (a) fifth layer, and (b) seventh layer of the LHM slab lens at 3.89 GHz.

The spot sizes of the focused beams along the lateral direction (x) for both source distances are ~0.4λ. We were able to focus EM waves that were smaller than half of the wavelength. However, the distances of the focal point are away from the surface of the LHM lens. The FWHM of the focused beam will be

smaller if the image is formed closer to the LHM lens, since the evanescent modes are present near the LHM lens.

4.3.2. Superlens behavior

In the previous section, we investigated the imaging properties of the flat lens at 3.89 GHz. At a lower frequency, however, at f = 3.77 GHz, the imaging behavior changes. Figure 4.7 displays the intensity distribution of the EM waves at 3.77 GHz where the sources are located inside the fourth and fifth layers of the LHM flat lens. The EM waves are focused along the lateral direction for both source distances.

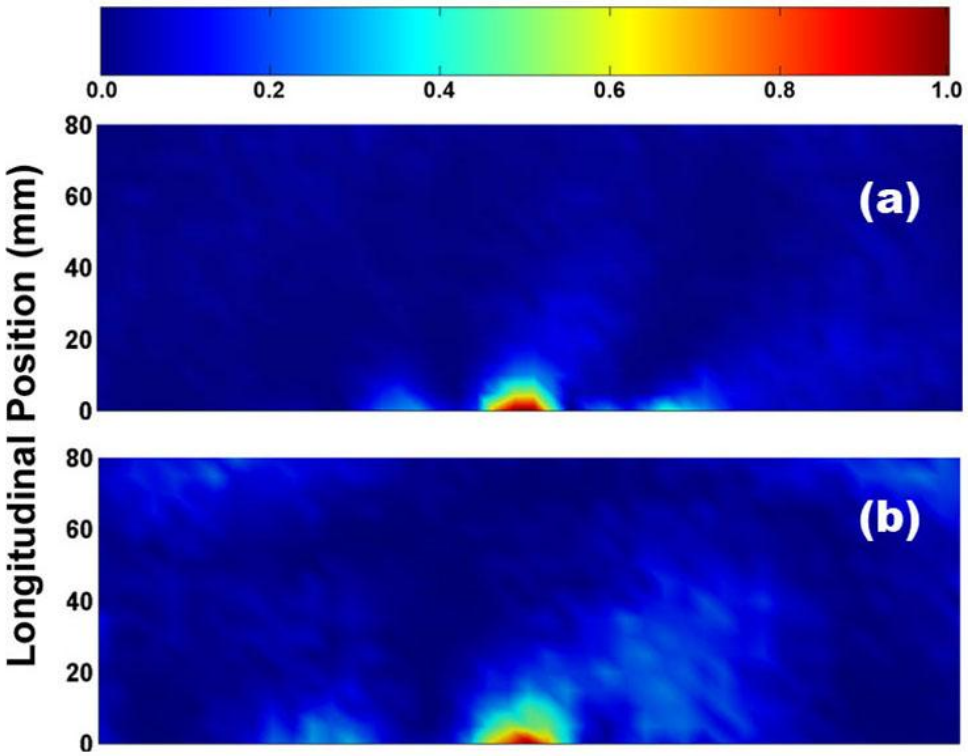

Figure 4.7: The spatial intensity distribution of the outgoing EM waves from the sources located inside the (a) fourth layer and (b) fifth layer of the LHM slab lens at 3.77 GHz.

We also performed scanning measurements in air by removing the LHM lens. The EM waves are scanned from 50 mm away from the point source. The resulting intensity distribution of the EM waves propagating in free space is provided in Fig. 4.8. The beam size in free space is clearly larger than that of the EM wave propagating inside the lens.

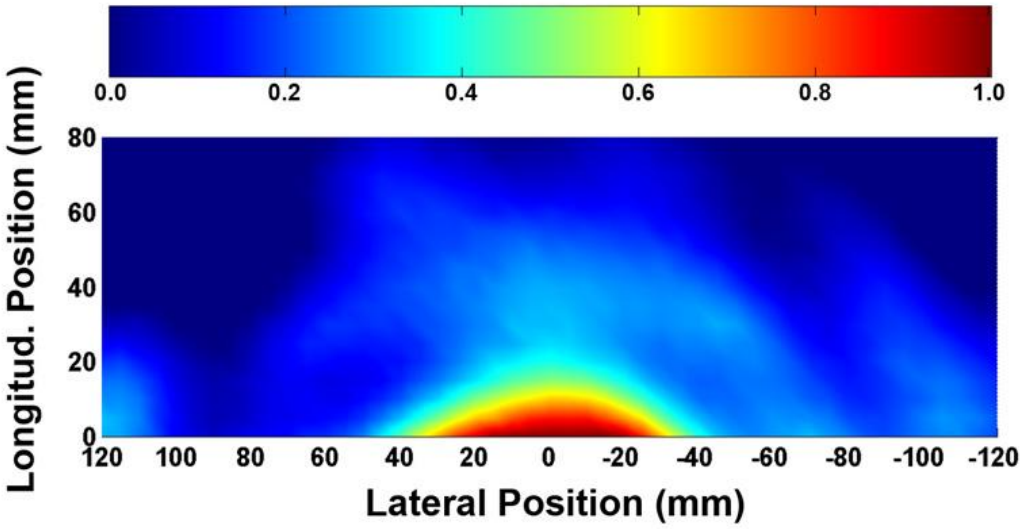

Figure 4.8: The spatial intensity distribution of the outgoing EM waves in free space from the source located at 50 mm away from the z = 0 point at 3.77 GHz.

We plotted the intensity profiles of the outgoing EM waves at z = 0 point for free space and LHM lens in Fig. 4.9. When the EM wave propagates 50 mm away from the source in free space (dashed green line), the full width at half maximum (FWHM) of the beam is measured to be 85 mm (1.07λ). FWHMs of the focused beam from the sources located inside the fourth and fifth layer of the LHM lens are 12.5 mm (0.16λ) and 17.5 mm (0.22λ), respectively. The intensities are normalized with the highest peak value for the source located inside the fourth layer, fifth layer and in air. The intensity is of air is multiplied with 0.5 in the figure. The highest transmission is observed in free space as expected. Intuitively,

the transmission is higher for the source located in the fourth layer, since the EM waves travel less in the lossy LHM media.

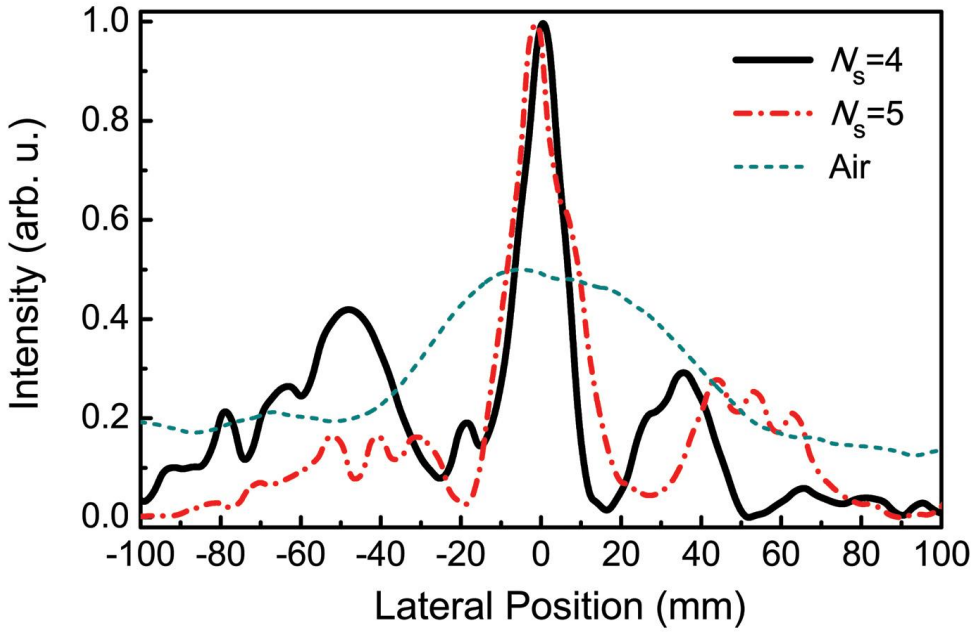

Figure 4.9: The focused beam profile near the LHM-air interface for the sources located inside the fourth layer (black) and fifth layer (red) of the LHM slab at 3.77 GHz. The blue dashed line represents the beam profile when the LHM lens is removed and EM waves propagate in air.

Figure 4.10 depicts the intensity profiles of the EM waves near the LHM lens as a function of the frequency. In addition, the measured reflection spectra for the LHM slab are shown in Fig. 4.10 as a white line. As clearly seen in the figure, the minimum spot size is achieved at frequencies where the reflection is at a minimum. In recent work, we verified the impedance of the LHM to be matched to the free-space impedance at 3.77 GHz, where the reflection is very low. Therefore, the losses due to the reflection do not significantly affect the resolution at this frequency. It is clear from Fig. 4.10 that the beam size of the EM waves at z=0 point is at a minimum at 3.77 GHz. The beam size increases with an increase in

the reflection value. To our knowledge this experiment is the first to have shown the effect of reflection on subwavelength imaging of LHM superlenses.

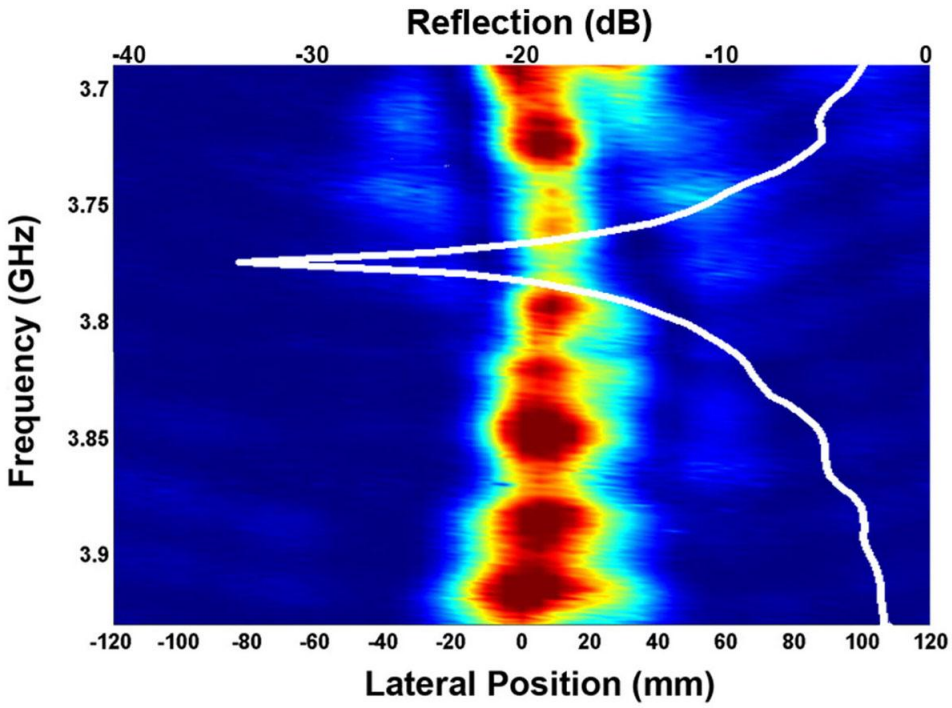

Figure 4.10: The intensity profiles of EM waves near the LHM lens as a function of frequency. The reflection spectrum of the LHM lens is shown in the figure with a white line.

Pendry introduced the term perfect lens, a lens that is capable of overcoming the diffraction limit provided that the $\varepsilon = \mu = -1$. However, it is not easy to fabricate a lossless and perfectly matched negative refractive index material. A perfect lens has not been experimentally shown yet, however it is possible to focus EM waves smaller than a half-wavelength size, which is the diffraction limit.

Negative index materials can recover the evanescent modes in an image, which is not possible for a positive index material. These decaying modes carry information approximately at the near-field of the image. Evanescent modes are amplified at the surface of the LHM lens, in which these modes decay in free

space. Evidently, the near-field information will be lost. Therefore, the focal point is important for resolving the power of a superlens. At 3.77 GHz, we observed a spot size of 0.16λ, however at 3.89 GHz at the focal point, the spot size was 0.4λ.

Chapter 5

Subwavelength resolution with a superlens

5.1. Introduction

Perfect lens is one of the most important applications of materials with negative refractive index. The term, perfect lens, is coined by Pendry owing to the ability of such lenses to reconstruct a perfect image by recovering the evanescent components of the electromagnetic waves [18]. In conventional optics, the lenses are constructed from positive-index materials and require curved surfaces to bring EM waves into a focus. Positive-index lenses suffer from the diffraction limit dictated by wave optics and can only focus objects with sizes on the order of half-wavelength. The finer details of the image are carried by high wave-vector components, so called evanescent waves and they quickly decay before reaching to the image plane. Thus, the contribution of evanescent components to the resolution of the image is absent in conventional lenses. However, Pendry conceived that it is possible to enhance evanescent waves by virtue of a negative refractive index [18]. In near-field regime, the electrostatic and magnetostatic limits apply and thus the electric and magnetic responses of materials can be treated as decoupled. This in turn, brings the possibility of constructing superlenses from materials with

negative permittivity [21, 24, 26] or negative permeability [38]. Photonic crystals [97], transmission lines [23] and metamaterials [19, 25] are experimentally demonstrated to achieve diffraction-free imaging and further theoretical studies supported these results [22, 98-101].

In this chapter, we use a negative-index metamaterial based superlens to resolve two point sources that are separated $\lambda/8$ away. We obtained a considerably high resolution (0.13λ) from a single source with a low loss, impedance-matched NIM superlens which has a refractive index of -2.07. We further proved experimentally that the thickness significantly degrades the performance of the superlens.

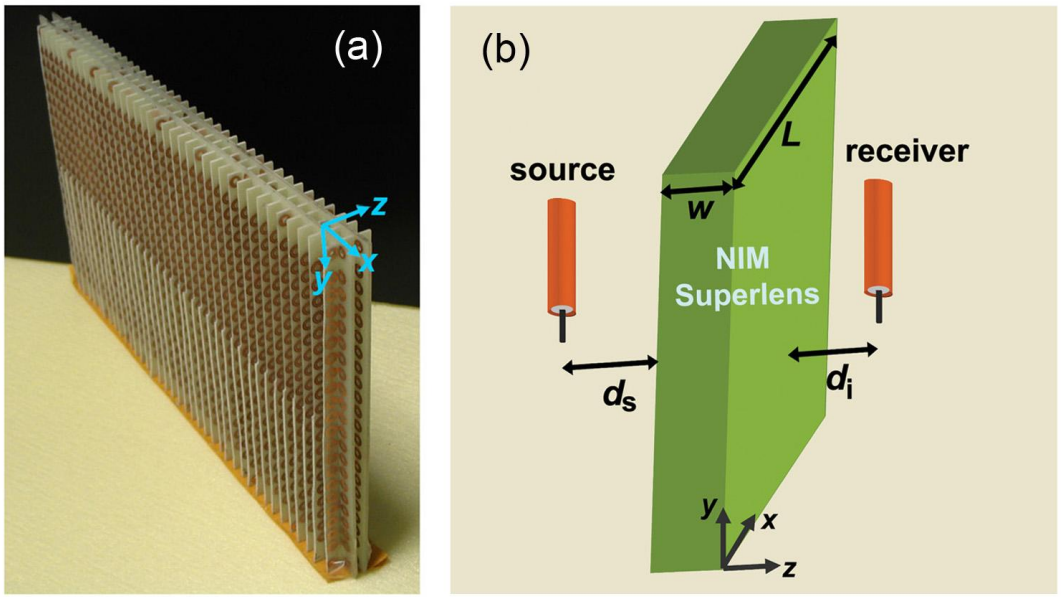

Figure 5.1: The photograph of negative-index metamaterial slab with three unit cells along z-direction. (b) Scheme of experimental setup for imaging measurements.

5.2. Effective parameters of a 2D NIM

The negative-index metamaterial under investigation is a slab of two-dimensional SRR-wire arrays deposited on FR4 printed circuit boards (Fig. 5.1(a)). The NIM slab has 40×20×3 layers along the *x*, *y* and *z* directions with equal lattice constants in all directions, $a_x = a_y = a_z = 9.3$ mm. Transmission and reflection measurements are performed to characterize 2D NIM and the results are plotted in Fig. 5.2. A well-defined transmission peak is observed between 3.65−4.00 GHz, where the effective permeability and the effective permittivity of NIM are simultaneously negative. Thus, this particular frequency range corresponds to the left-handed propagation regime. Interestingly, a sharp dip is observed in the reflection spectrum at 3.78 GHz. The reflection is very low, -37 dB, meaning that the incident EM waves almost do not face any reflection at the NIM surface.

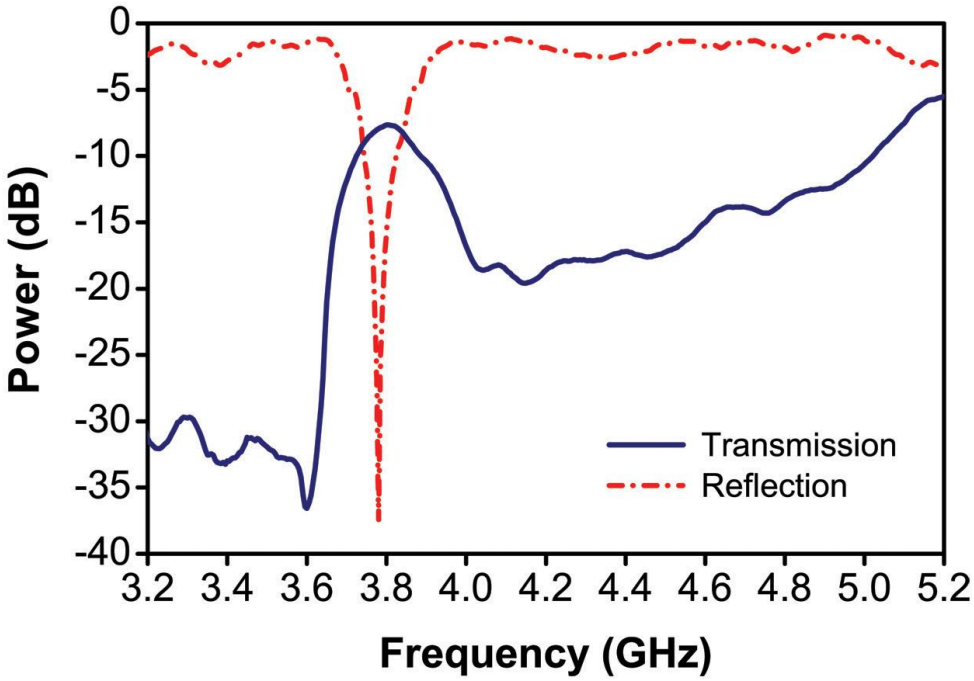

Figure 5.2: Measured transmission (blue) and reflection (red) spectra for an NIM slab.

The effective parameters of the NIM structure are retrieved by using the calculated amplitudes and phases of transmission and reflection. Dielectric permittivity, $\varepsilon = \varepsilon' + i\varepsilon''$ and magnetic permeability, $\mu = \mu' + i\mu''$ are used to describe the response of materials to the incident electromagnetic field; where ε' and μ' are the real parts, ε'' and μ'' are the imaginary parts of the corresponding effective parameters. Figure 5.3 depicts the real parts of ε and μ. Throughout the interested range of frequencies, ε' is negative and μ' possesses negative values between 3.63−3.93 GHz.

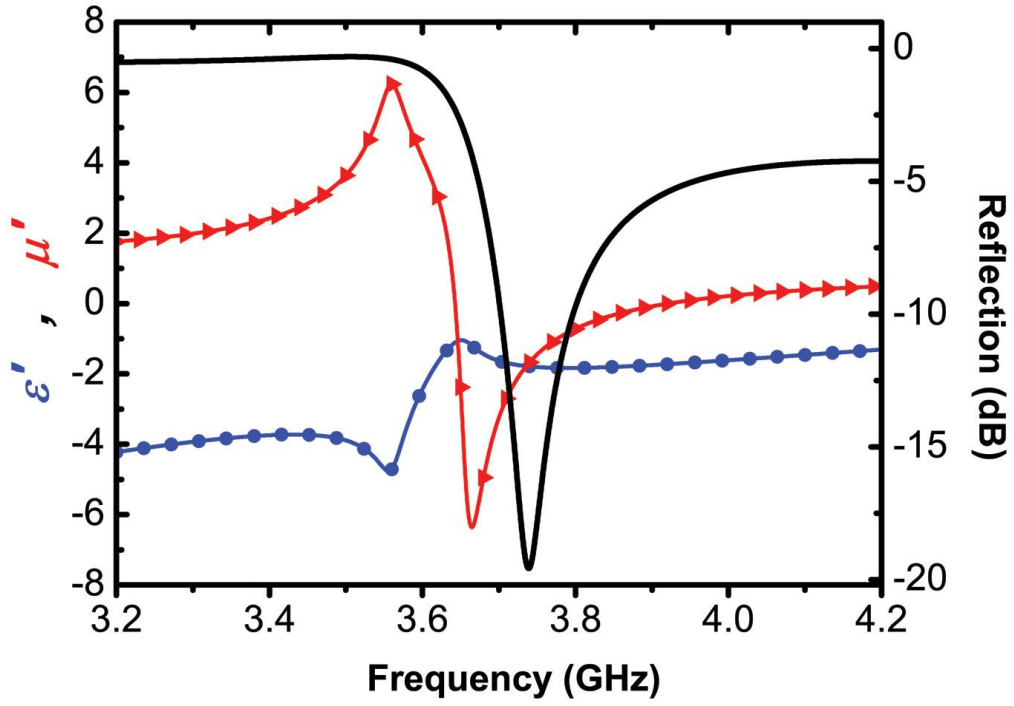

Figure 5.3: Real parts of retrieved effective permittivity (blue) and permeability (red). Reflection spectrum is also plotted within the figure with black line.

The minimum reflection in the simulations occurs at 3.74 GHz, where ε' and μ' are equal with an effective value of -1.8 as plotted with black line in Fig. 5.3. The difference (0.04 GHz) between the frequencies of observed and simulated

minimum reflection may be explained with the deviation of structure parameters during fabricating and aligning the NIM. The real and imaginary parts of index of refraction, *n*' and *n*" and the real part of impedance, *Z*' is plotted in Fig. 5.4. The impedance is defined as $Z = \sqrt{\mu'/\varepsilon'}$, one expects to have an impedance matched medium for the case, where the real parts of ε and μ are equal ($\varepsilon' = \mu'$). Expectedly, impedance of NIM is matched to that of free-space at 3.74 GHz, where *Z*'=1. Conventional materials are not matched to the free-space, but NIM structures has an advantage for achieving matched impedance since their effective permeability and permittivity are strongly frequency dispersive close to the resonant frequencies.

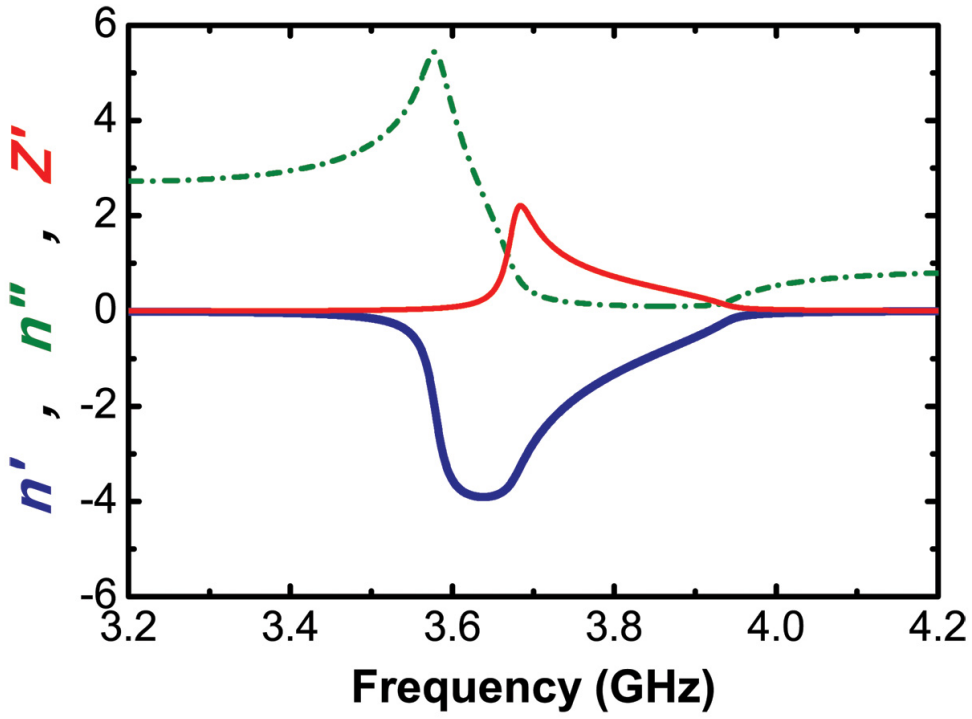

Figure 5.4: Real parts of retrieved refractive index (blue), impedance (red) and imaginary part of the refractive index (green).

5.3. Imaging beyond the diffraction-limit

In previous chapter, we verified that NIM structures used in these experiments exhibit negative refraction and have negative phase velocity at the left-handed propagation regime. The imaging measurements presented here are performed at 3.78 GHz, where the reflection is considerably low and the losses due to reflection are negligible. The NIM has a refractive index of n_{eff} = -2.07±0.22 at 3.78 GHz, which is measured by using a wedge-shaped 2D NIM. The refractive index obtained form the retrieval procedure is n_{eff} = -1.81, with a slight difference from the measured value. In order to use NIMs in practical applications, the structures should have large figure of merit. Figure of merit is defined as the ratio of n' to n'' and widely used in the literature to characterize the performance of negative-index metamaterials [58, 59, 102]. If the imaginary part of refractive index is high, the losses will considerably affect the performance of NIM superlens. In our simulations, the real and imaginary parts of refractive index at the frequency of minimum reflection are calculated to be n'=-1.81 and n'' = -0.15. Therefore the figure of merit is found to be 12, which is one of the highest value ever reported. The NIM structure under investigation has low absorption losses and therefore can be used to achieve subwavelength resolution.

In the imaging experiments, we employed monopole antennas to imitate the point source. The monopole antenna was constructed by removing the shield around one end of a microwave coaxial cable. The exposed center conductor acts as the transmitter and receiver and has a length of 4 cm (~λ/2). A schematic of experimental setup is provided in Fig. 5.1(b). The source antenna is located d_s=1.2 cm away from first boundary and the image forms d_i=0.8 cm away from second boundary of the superlens. The intensity of the electric field at the image plane is scanned by receiver antenna with Δx = 2 mm steps. The NIM slab has a thickness of w=2.56 cm (λ/3) and a length of L=38 cm (4.8λ).

Firstly, we measured the beam profile in free space, i.e. without NIM superlens and the result is plotted in Fig. 5.5 with red dashed line. The full width at half maximum (FWHM) of the beam is 8.2 cm (1.03λ). The field intensity in free space is multiplied with 0.4 in the figure. Then we inserted NIM superlens, and measured the spot size of the beam as 0.13λ, which is well below the diffraction limit. The field intensity is normalized with respect to the maximum intensity in Fig. 5.5.

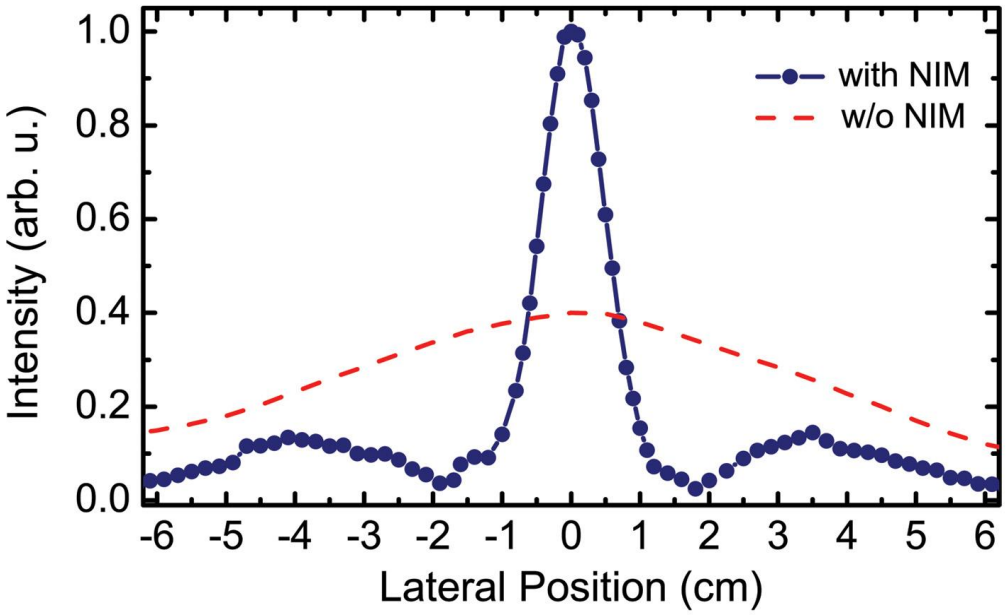

Figure 5.5: The power distribution at the image plane with (blue) and without (dashed red line) NIM superlens.

However, observed high localization of the EM field could be due to channeling effect. The SRR-wire boards are separated with 9.3 mm and the field may propagate on these channels. To ensure that subwavelength imaging is due to the effective response of NIM not that of channels, we performed an additional check. We moved the point source along the source plane by keeping d_s constant. The initial experiment was performed at the point x = 0. Two separate

measurements are done for the point sources at x = 0.5 cm an x = -1.3 cm. The resulting field distribution is plotted in Fig. 5.6 and in all cases the images are formed exactly at the same x-distance with the source. Worthy of note is that the distances are not the multiples of the lattice constant, i.e. the sources are not located on the axes of SRR-wire boards. We can safely claim that the NIM superlens has a flat lens behavior [103, 104].

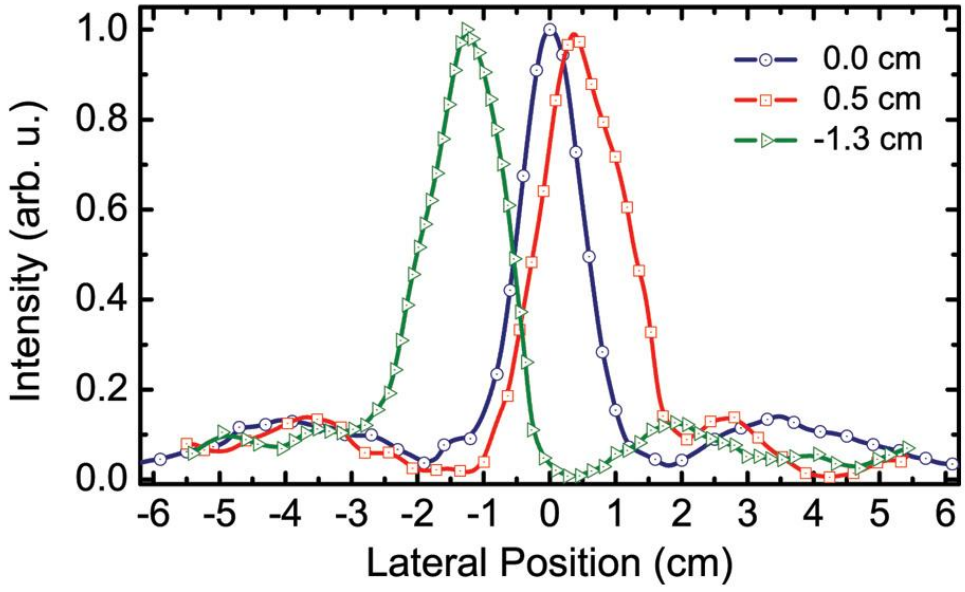

Figure 5.6: The field profiles from single sources placed at three different locations along x-direction, that are x = 0.0 mm (black line), x = 0.5 cm (red line) and x = -1.3 cm (blue line).

5.4. Subwavelength resolution

Since we were able to image a single point source with a subwavelength spot size, we used two point sources separated by distances smaller than wavelength to obtain subwavelength resolution. The sources are driven by two independent signal generators and the power distribution is detected by using a microwave

spectrum analyzer. The frequencies of the sources differ by 1 MHz to ensure that the sources are totally incoherent. The reason behind using incoherent sources is to prevent the contribution of interference effects to the resolution. The imaging experiments are performed for three different separation distances between the sources. The measured power distribution of sources separated by $\lambda/8$ is plotted by blue line in Fig. 5.7. As seen in the figure, the peaks of two sources are clearly resolved. The red line corresponds to $\lambda/5$ separation between the sources and the resolution gets better in this case. Finally, when the sources are $\lambda/3$ apart (green line), two peaks are totally resolved.

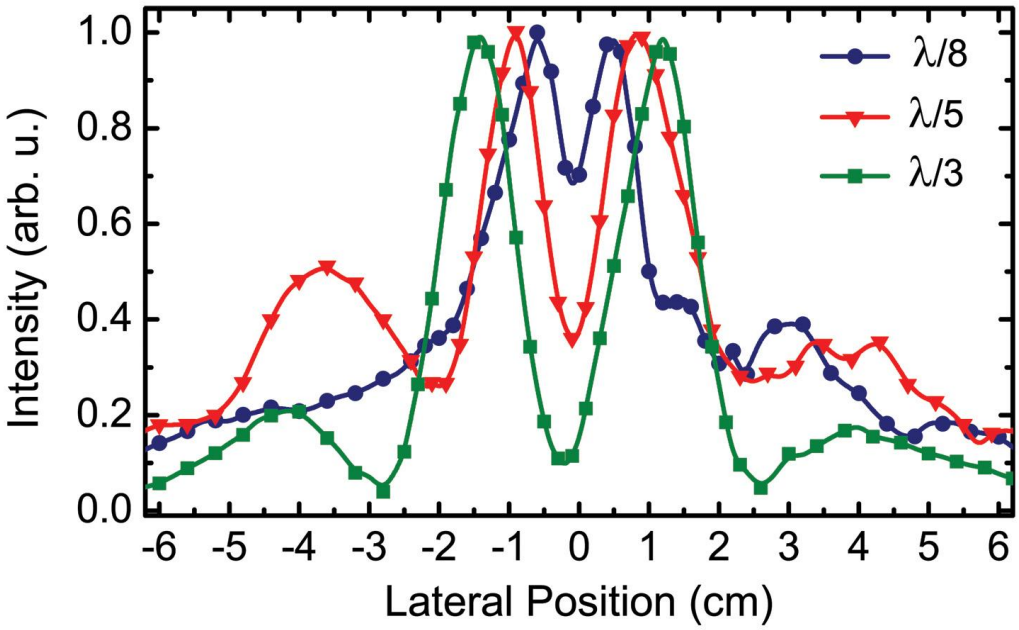

Figure 5.7: The measured power distributions for two point sources separated with distances of $\lambda/8$ (black line), $\lambda/5$ (red line) and $\lambda/3$ (blue line).

We avoid placing sources at the line of SRR-wire boards and the distances between the sources in three cases are not multiples of the lattice constant. The lattice constant is on the order of $\lambda/8.5$, which is well below the wavelength and indeed the NIM structure behaves as an effective medium. The periodicity has a

significant effect on the resolution of the superlens by limiting the recovery of evanescent components [101]. The resolving power can further be increased by using structures with smaller periodicities, but we are restricted to the periodicity of 9.3 mm in order to fabricate an effective two-dimensional negative-index metamaterial.

5.5. Effect of superlens thickness

The thickness of the superlens is critical to achieve high resolution. The effect of thickness is theoretically shown to affect the resolving power [25, 101]. Here, we experimentally verify this effect. We performed imaging experiments with a thicker NIM superlens having 5 unit cells along propagation direction, corresponding to a thickness of w=4.44 cm (0.55λ). The power distribution at the image plane emanating from a single source is shown in Fig. 5.8(a) with red line. FWHM of the image is almost doubled to 0.25λ compared with the image obtained from the thinner lens. Figure 5.8(b) provides comparison of the field profiles between thin and thicker superlenses, obtained from two sources separated by a distance λ/5. The thin superlens has a better resolution compared to thicker superlens. The presence of losses due to absorption hinders the evanescent wave amplification when thicker lenses are used.

The performance of the NIM superlens examined in this study is far from a perfect lens. The perfect lens requires an effective refractive index of n_{eff} = -1 with the condition that ε_{eff} = -1 and μ_{eff} = -1. A perfect lens has not been experimentally shown yet, since the task to fabricate lossless, perfectly matched materials with desired effective parameters is rather difficult. However, it is still possible to reconstruct images below diffraction limit even in the presence of losses. The deviations from the ideal effective parameters n=-1, and ε = μ= -1 also affects the resolving power of a superlens [22, 100, 101]. The imaging experiments presented

here are performed in the near-field regime, since the distances of source and image planes and the thickness of the superlens are below the wavelength. The evanescent components of the EM wave can only be amplified to the second boundary of the superlens and start to die away from the surface. Hence, we are restricted to operate in the near-field regime with current lossy metamaterial designs [100].

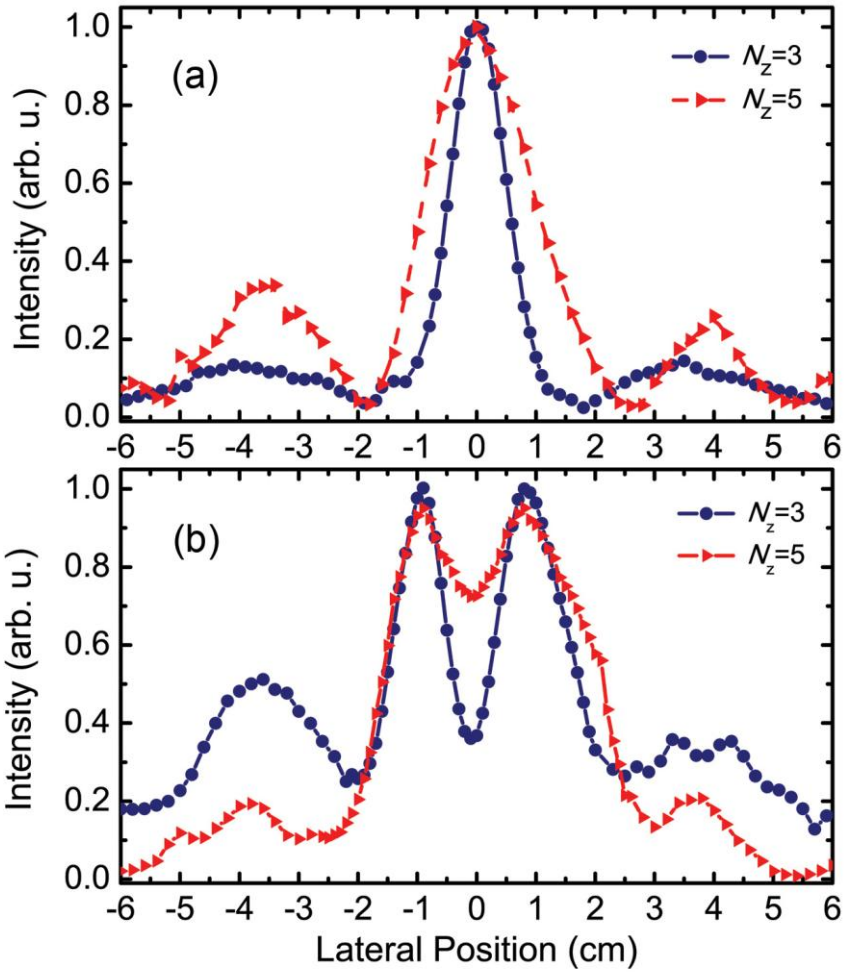

Figure 5.8: The measured field profiles obtained from NIM superlenses with thicknesses w=2.56 cm (blue line) and w=4.44 cm (red line). The NIM superlens is excited with a single source in (a), and with two point sources separated with $\lambda/5$ in (b).

The advantage of using negative-index lenses over negative-permittivity of negative-permeability lenses is that the subwavelength resolution can be obtained for both transverse-electric (TE) and transverse-magnetic (TM) polarization of EM waves. However single-negative can only focus one particular polarization. Photonic crystals (PC) are shown to exhibit subwavelength resolution at microwave frequencies [97]. Dielectric PCs has low losses compared to metamaterial lenses that contain metals. However metamaterial lenses could be designed to achieve impedance-matching at the surface, therefore the reflection could significantly be reduced. It is rather difficult to obtain an impedance-matched PC since magnetic permeability cannot be controlled effectively. PCs, for the time being can only focus particular polarizations of EM waves and complex designs are needed to achieve subwavelength imaging for both polarizations. Also PCs are not effective media since their lattice constants are comparable to half-wavelength; therefore the highest resolution is somewhat limited with the periodicity of the photonic crystal.

Chapter 6

Fishnet-type planar metamaterials

6.1. Introduction

Split ring resonators received a great amount of interest and were widely studied for constructing metamaterials at the microwave [1, 40, 41, 46], millimeter wave [53], and terahertz [54, 55]frequencies. Split ring resonators are not suitable for the planar configuration of metamaterials, since the incident EM wave has to be parallel to the SRR, provided that the magnetic field is perpendicular to the SRR. The magnetic response of split ring resonators starts to saturate optical frequencies [78], and therefore optical magnetism is not achievable with SRRs. However, it is shown that an alternative structure of metal-dielectric composite provides magnetic resonance at optical frequencies [58, 59]. The structure consists of parallel metal slabs with a dielectric substrate in between, wherein the metal slabs provide the inductance and dielectric spacing that in turn provides the capacitance [58]. Realizations of metamaterials using parallel metal slabs (also known as cut-wire pairs) at microwave frequencies followed soon after [105-107]. Fishnet type metamaterials are also reported to exhibit a negative-index at optical [59, 60, 62, 93] and microwave frequencies [37, 108, 109]. The advantage of metamaterials

with fishnet geometry is that the wires providing for negative permittivity and the slab pairs providing for negative permeability are brought together to produce a combined electromagnetic response.

In this chapter, we demonstrate a planar negative-index metamaterial (NIM) that operates independent of the incident polarization due to its symmetric configuration. Single-layer and multi-layer metamaterials are characterized by transmission measurements and simulations.

6.2. Transmission through a fishnet type metamaterial

The fishnet type metamaterials were previously shown to be possible candidates for planar negative index metamaterials. We employed fishnet geometry to construct a metamaterial operating at microwave frequencies. A schematic of a fishnet unit cell is shown in Fig. 6.1(a). The highlighted areas are the metallic parts. The metal used to construct the structure is copper with a thickness of 20 μm. The substrate is a Teflon board with a thickness of t=1 mm. The unit cell is repeated periodically along the x and y directions with a periodicity of a_x=a_y=14 mm.

The structure can be considered as a combination of parallel metal slab pairs with the sizes $w_y \times a_x$, which provide the magnetic resonance and continuous wire pairs with the sizes $w_x \times a_y$ in turn providing the negative permittivity [108]. Here, we chose $w_x = w_y = 7$ mm, and therefore the structure is symmetric in all directions. The structure will then work for TE and TM polarizations, as well as for arbitrary linear polarizations due to the symmetry of the slab and wire pairs. Therefore, the NIM will be functional independent of the incident polarization [108].

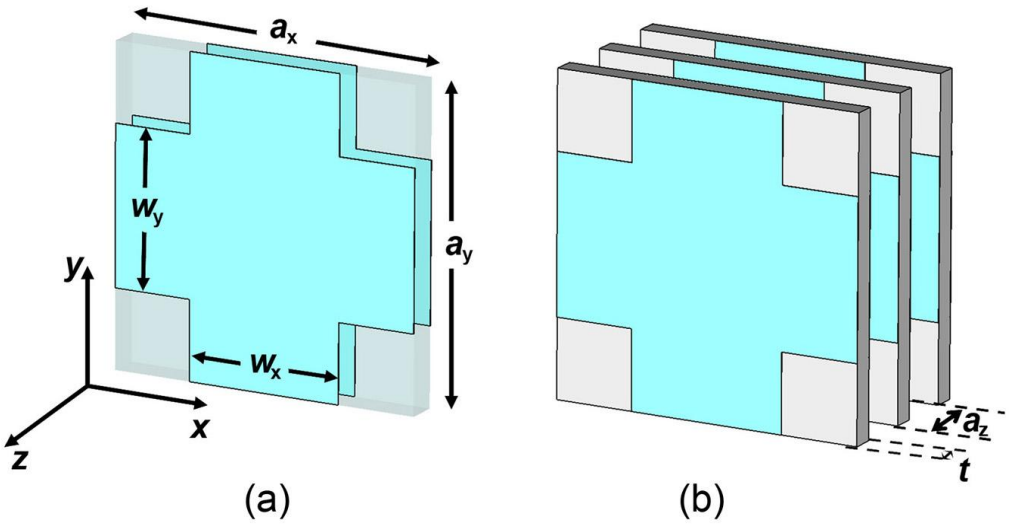

Figure 6.1: Schematic drawings of (a) a fishnet unit cell, and (b) a multi-layer fishnet metamaterial structure.

The number of layers in a single fishnet metamaterial layer (see the inset of Fig. 6.2) are N_x=N_y=10. We then stacked layers with a periodicity along the *z* direction, a_z=2 mm (Fig. 6.1(b)). Transmission and phase measurements were performed using an Agilent N5230A portable network analyzer, which is capable of measuring S-parameters and phase amplitudes. Transmitter and receiver antennae are standard high gain microwave horn antennae. The wave propagates along the *z*-direction, with the *E*-field parallel to the *y* axis and the *H* field parallel to the *x* axis. In these measurements, the distance between the horn antennae were kept at 35 cm. We first measured the transmission through air, and then used this data as a calibration. The measured transmission spectrum of a single fishnet metamaterial layer is plotted with a blue line as shown in Fig. 6.2. We observe a transmission peak between 14.2 and 14.8 GHz that is highlighted in Fig. 6.2. The peak value is -2.4 dB at 14.38 GHz. This transmission band corresponds to the negative-index regime and is a left-handed transmission band, as we will show later on in the following section.

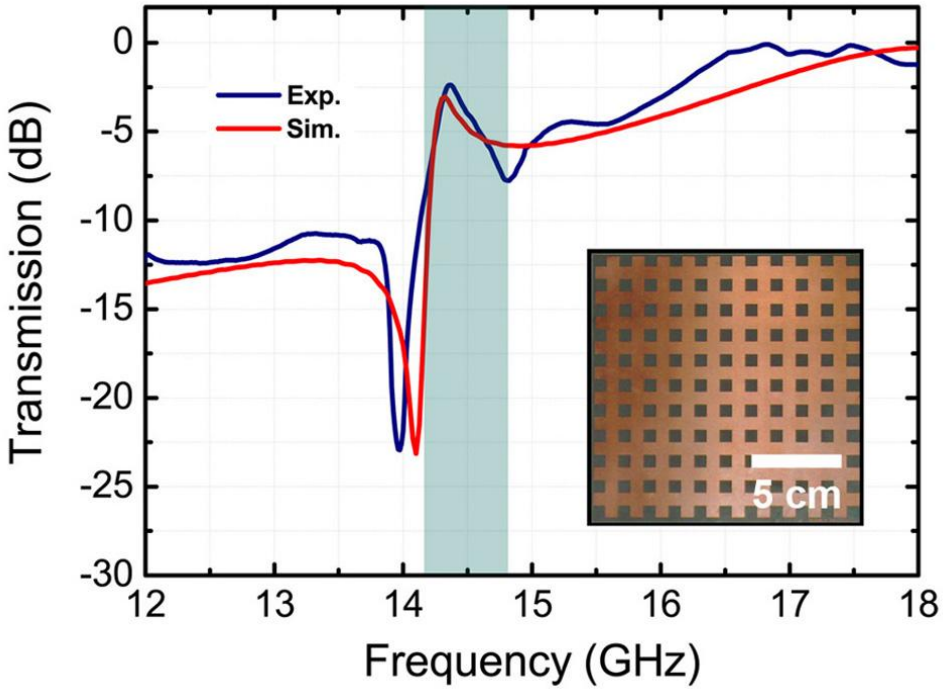

Figure 6.2: Measured (blue line) and simulated (red line) transmission spectra of a single layer fishnet metamaterial. The photograph of the real structure is shown in the inset.

We performed numerical simulations in order to check the experimental results. We used the commercially available software, CST Microwave Studio, for the simulations. We simulated the unit cell as shown in Fig. 6.1(a), with periodic boundary conditions at the *x* and *y* axes. Along the propagation direction (*z* axis), we employed open boundary conditions. Waveguide ports are used to excite and detect electromagnetic waves. The dielectric constant of the Teflon board was taken as ε=2.16 with a tangent loss of δ=0.005. The red line in Fig. 6.2 shows the simulated transmission spectrum of a single layer fishnet structure. The agreement between the theory and experiment is quite good. The transmission peak had a value of -2.9 dB at 14.33 GHz.

Planar metamaterials, where the electromagnetic wave is incident normal to the plane of the metamaterials, were first realized at optical frequencies [59, 60, 62, 93]. The characterization of optical negative-index metamaterials were mainly

done by using a single layer. It is obvious that the basic properties of metamaterial structures, such as a negative index of refraction, the negative phase advance cannot be verified by simply using a single layer of the metamaterial. Recently, there have been studies that characterize planar negative-index metamaterials with more than one layer along the propagation direction [62, 110, 111]. Here, we report the transmission measurements of a two-layer and five-layer NIM structure. Fig. 6.3(a) shows the measured (blue line) and simulated (red line) transmission spectra of a two-layer NIM structure. The periodicity along the propagation direction is a_z = 2 mm. The transmission band is present with a maximum value of -3.7 dB at 14.38 GHz that is obtained from the measurements. The simulation results predict a similar transmission band where the peak is at 14.33 GHz with a maximum value of -3.0 dB.

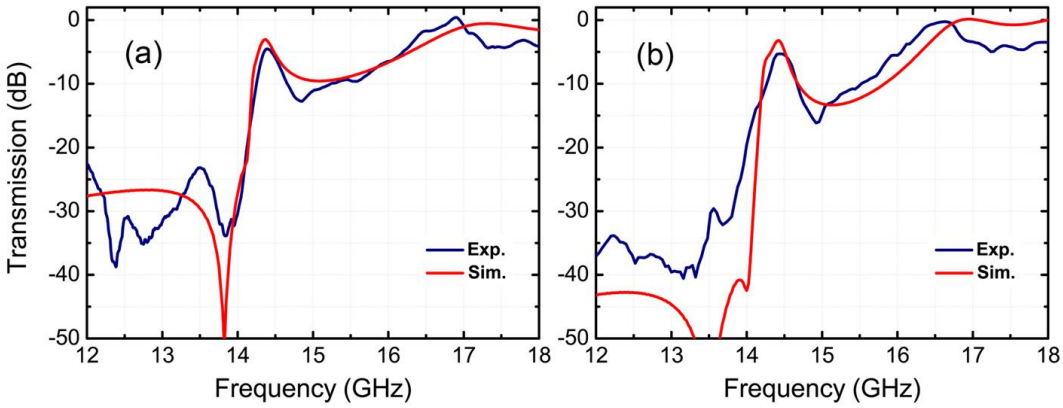

Figure 6.3: Measured (blue line) and simulated (red line) transmission spectra of (a) two-layer and (b) five-layer fishnet metamaterial.

Experimental and simulation results of the transmission spectra of five-layer NIM are shown in Fig. 6.3(b). The transmission peak is at 14. 42 GHz, measured as -5.0 dB, and simulated as -3.2 dB. Slight differences between the simulation and experiments can be attributed to the deviation from the ideal material parameters and possible misalignments that may occur during the stacking of the layers. In the

simulations, the metamaterial is infinitely periodic along *x* and *y* directions, however experimental structure has a finite size which may cause diffraction at the edges. It is noteworthy that increasing the number of layers does not significantly change the transmission value at the left-handed transmission band. This is due to the specific choice of the substrate. The loss mechanism in the fishnet structure is mainly due to the substrate losses. Although the amount of metal is increased by a factor of five, from a one-layer structure to a five-layer structure, the transmission only decreased by -2.6 dB in the measurement. The result is more significant in the simulation results (ideal case) that the transmission peak did not change from a one-layer to a five-layer NIM.

6.3. Retrieved effective parameters

One of the most common characterization tools for the metamaterial structures is the retrieval procedure. It is widely used to calculate the effective parameters of the metamaterial under investigation. The amplitude and phase of the transmission and reflection are either calculated or measured, in which the real and imaginary parts of the refractive index and wave impedance are then retrieved from the transmission and reflection coefficients. We employed the retrieval procedure to obtain effective permittivity, permeability, and a refractive index. We followed the approach as outlined in Ref. [68].

In the retrieval procedure, we employed a single layer of NIM along the *z* axis. Hence, the simulation setup coincides with a slab of NIM that consists of single layer. The effective permittivity and permeability values were then derived from the transmission and reflection coefficients of a single layer of NIM. The real (blue line) and imaginary (red dashed line) parts of the effective permittivity (Fig. 6.4(a)), permeability (Fig. 6.4(c)), and index of refraction (Fig. 6.4(e)) for a single

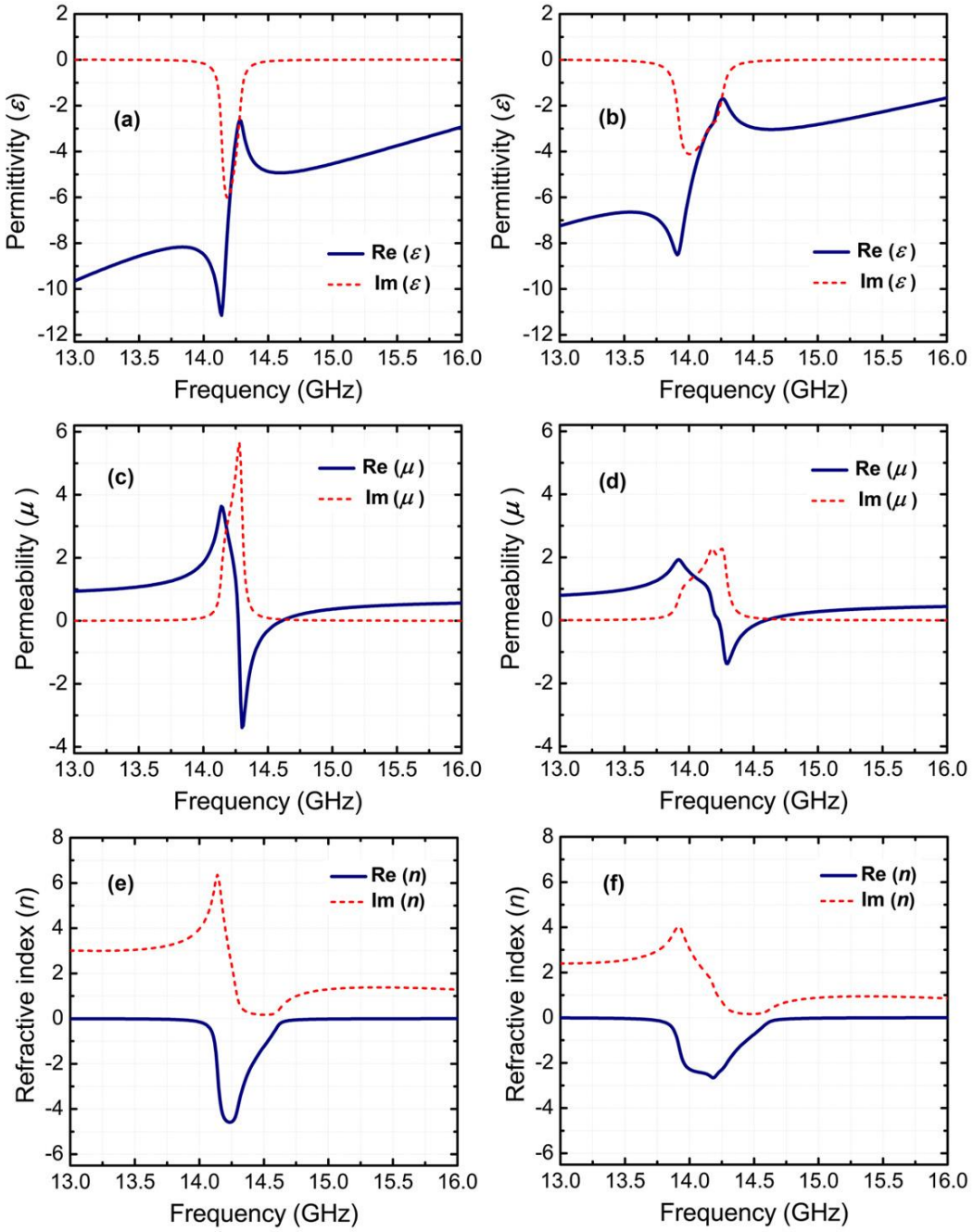

Figure 6.4: Retrieved effective parameters of a (left) single-layer and a (right) two-layer fishnet metamaterials. The real (blue line) and imaginary (red dashed line) parts of effective permittivity (top), permeability (middle), and refractive index (bottom) are shown.

layer of NIM structure was consistent with the simulated and measured transmission spectra. The effective permittivity is negative within the frequency range of interest. The continuous wire arrays that are aligned along the *y* axis cause plasma oscillations. The plasma frequency of an NIM structure is approx. 16.5 GHz. The resonance in the permittivity at approx. 14.25 GHz is a common characteristic of metamaterials with a negative index. The real part of the magnetic permeability has negative values between 14.23 and 14.65 GHz. The lowest value of μ is -3.38 at 14.3 GHz for a single layer NIM. Since both permeability and permittivity are simultaneously negative, the condition needed in order to have a negative index is satisfied. As seen in Fig. 6.4(e), the NIM structure possesses negative values of the refractive index within the frequency range 13.95–14.65 GHz. The retrieval procedure is mainly performed for single unit cells along the propagation direction. However, recent studies have revealed that the geometric size of the structure that was used to calculate the transmission and reflection coefficients affect the retrieved parameters [37, 87]. To check this effect in our fishnet type metamaterial design, we performed further simulations for a two-layer NIM structure. Figures 6.4(b), 6.4(d), and 6.4(f) show the effective permittivity, permeability, and refractive index, respectively. Comparing the results of one-layer and two-layer NIM structure, it is obvious that the real and imaginary parts of ε, μ, and n are different. A single layer NIM responds to the incident electromagnetic field stronger than the two-layer structure. We see that the permittivity values were higher for the two-layer NIM structure. The minimum value of permeability for a two-layer NIM was -1.37 at 14.3 GHz. Throughout the frequency range of interest, we found that the absolute values of permittivity and permeability of a one-layer structure is greater than that of a two-layer NIM, i.e. $|\varepsilon_{1L}| > |\varepsilon_{2L}|$ and $|\mu_{1L}| > |\mu_{2L}|$. Retrieved parameters converge to a value if the metamaterial length employed in the retrieval procedure is equal to the convergence length of the metamaterial [37]. Since two unit cell is below the convergence length of a fishnet metamaterial [37], we found significant difference

in the parameters of one and two layer NIM structures. The results reported here are consistent with Zhou *et al.*, in which the authors performed a detailed analysis for the dependence of geometric size and lattice constant on the retrieved parameters of fishnet type metamaterials [37].

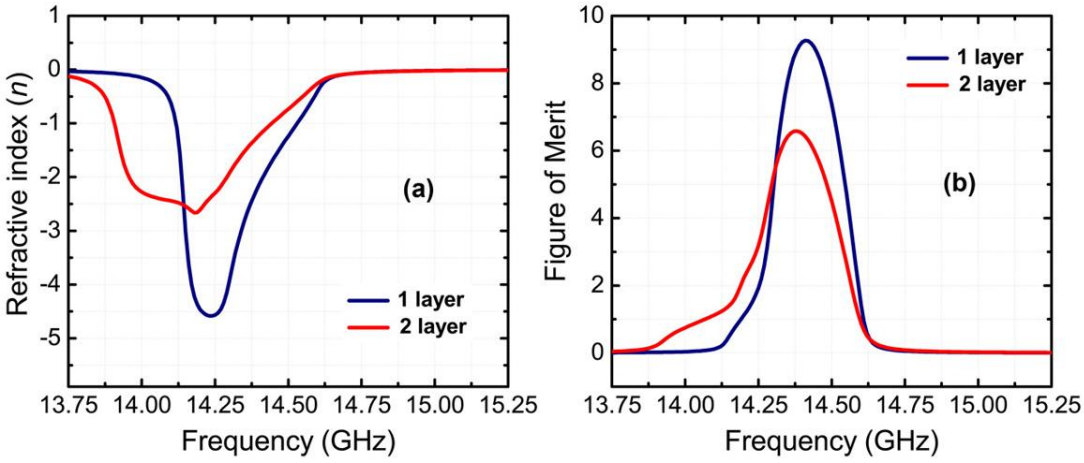

Figure 6.5: Real part of retrieved refractive index and (b) figure of merit for a single-layer (blue line) and two-layer metamaterial (red line).

The real parts of the refractive indices of a one and two-layer structure are plotted together in Fig. 6.5(a). As was expected, the relation between ε and μ holds true for the refractive index, since the index depends on ε and μ. The minimum values of the refractive index for a one-layer NIM was n = -4.58 (at 14.23 GHz) and a two-layer NIM was n = -2.66 (at 14.19 GHz). The frequency region between 14.23 and 14.65 GHz was a double negative region, which means that the permeability and permittivity were both negative. We found that the upper edge for the negative index regime was 14.65 GHz for a one and two-layer NIM, where the permeability starts to take on positive values. However, the lower edge is at lower frequencies for a two-layer NIM. Although the refractive index is negative between 13.72 and 14.23 GHz for a two-layer NIM, the permeability is positive within this frequency range. Therefore, the NIM structure behaves like a single

negative material [108]. For a one-layer NIM, the single negative frequency region was narrower, in turn appearing between 13.94 and 14.23 GHz.

The figure of merit (FOM) for negative-index metamaterials was defined as a ratio of the absolute value of the real part of an index to the imaginary part of an index, FOM = |Re(n)| / Im(n). Figure of merits for one and two-layer NIMs are shown in Fig. 6.5(b). It is obvious that the figure of merit is larger for a single layer NIM structure. The maximum figure of merit value is 9.26 at 14.41 GHz for a one-layer NIM. For a two-layer structure we found the highest value of figure of merit to be 6.58 at 14.38 GHz. FOM decreases with the increasing number of layers due to the decrease in the refractive index.

6.4. Negative phase advance and backward wave propagation

Negative index metamaterials are of special interest for obtaining backward wave propagation, since they inherently have a negative phase advance. A network analyzer is capable of measuring the transmitted phase. We constructed NIM structures with a_z=2 mm that have N_z= 2, 3, 4, and 5 layers along the propagation direction. The transmitted phase of NIM structures were measured by using the same setup with the transmission measurements. In the measurements, the transmitted phase is calibrated with respect to the phase in free space. Figure 6.6(a) shows the transmission phase between 14.20 and 14.65 GHz for two (blue line), three (red line), four (green line), and five (purple line) layers of the NIM structure. We plotted the transmitted phase in a narrow band since the transmission below 14.20 GHz and above 14.65 GHz are low and imaginary part of the refractive index is significant (see Fig. 6.4(f)). The phase decreases between 14.20 and 14.65 GHz with the increasing number of layers along the propagation

direction. This is typical behavior for left-handed metamaterials with a negative phase advance [50, 112].

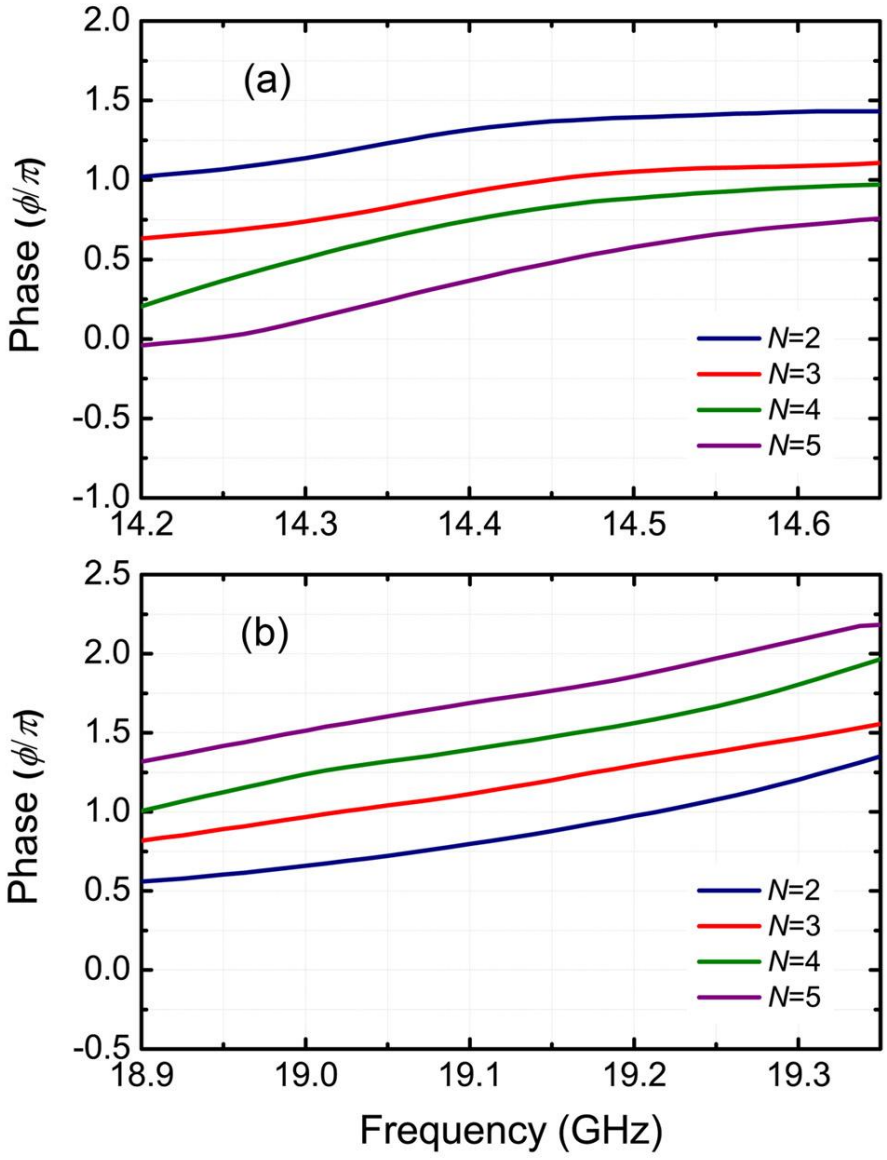

Figure 6.6: Transmitted phase of metamaterial structure for two (blue line), three (red line), four (green line), and five (purple line) NIM layers between (a) 14.2 and 14.8 GHz (left-handed transmission regime) and (b) 18.9 and 19.4 GHz (right-handed transmission regime).

We also performed phase measurements at a frequency range where we know that the transmission band has right handed characteristics. The phase spectra for four different NIM structures are shown in Fig. 6.6(b) at the right-handed transmission region. We observed an increase in the phase with the increasing number of layers along the propagation direction. The negative phase shift for a NIM structure at the negative-index frequency regime means that the phase is directed towards the source. Such behavior is due to the negative phase advance within the interested range of frequencies. These measurements clearly verify the negative phase advance behavior of planar fishnet type multi-layer metamaterials. To our knowledge, this is the first direct observation of negative phase advance for fishnet type NIM structures.

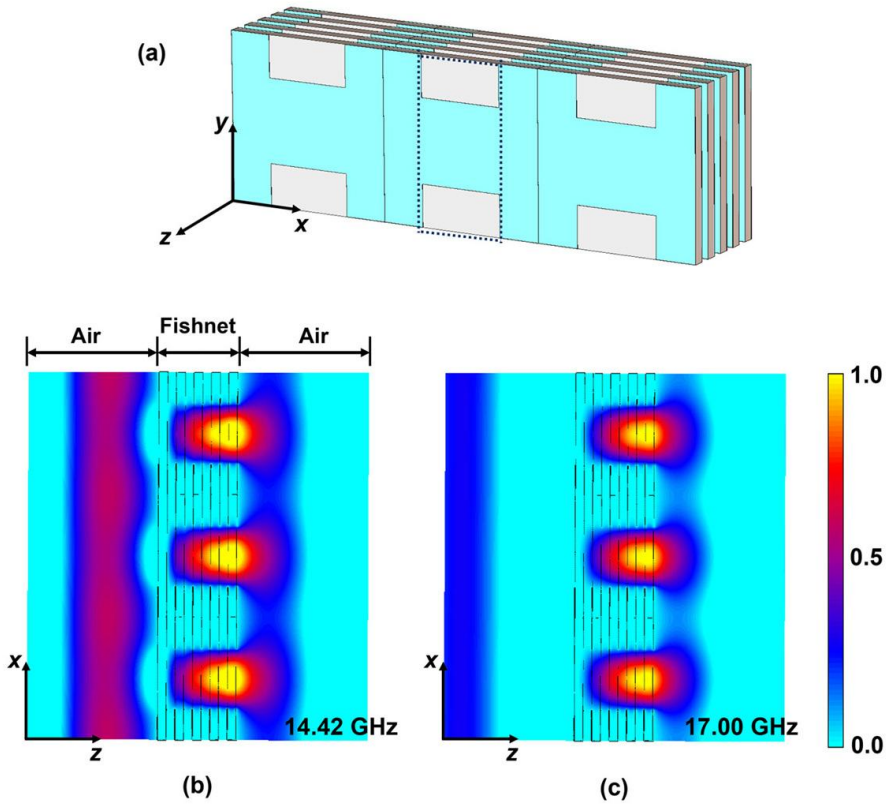

Figure 6.7: (a) Schematic drawing of a simulated NIM structure with an alternative unit cell. Simulated *E*-field profile evaluated at (b) 14.42 GHz and (c) 17.00 GHz.

Metamaterials with a negative phase advance are also called backward wave materials, since the wave propagation is towards the source inside the metamaterial. We performed numerical simulations using CST Microwave Studio in order to investigate the wave propagation inside our NIM structure. Figure 6.7(a) shows the simulated NIM structure. We used the same parameters with the structure as shown in Fig. 6.1(a), but in this case with an alternative unit cell. The structure is excited with a plane wave with a wave-vector along the +*z* direction using CST Microwave Studio. The *E* field is along the *y* axis and the *H* field is along the *x* axis in the simulations. The structure had three unit cells along *x* and 5 unit cells along *z*.

We calculated the electric field profile by placing electric field monitors along the *y* axis at two different frequencies, 14.42 GHz and 17.00 GHz. 14.42 GHz was the frequency of the highest transmission within the negative-index regime for a five-layer NIM. Figure 6.7(b) shows the *E* field profile along the *y* direction, where the profile was calculated at the point *y*=5 mm. The wave propagates along the +*z* direction in air. However, inside the fishnet structure, we observed backward wave propagation in the simulations. The EM wave is guided through channels as shown with a dashed rectangular box in Fig. 6.7(a). The wave propagation inside the metamaterial at 17.00 GHz is along the +*z* direction (Fig. 6.7(c)), since this frequency corresponds to the right-handed transmission regime where ε and μ are both positive.

Chapter 7

SRR-coupled enhanced transmission

7.1. Introduction

Enhanced transmission of light through apertures that are much smaller than the wavelength has received a burgeoning amount of interest [113], after the seminal work by Ebbesen *et al.*, realizing the extraordinary transmission from subwavelength hole arrays that were milled in optically thin metallic films [114]. Extraordinary light transmission has been extensively studied by using subwavelength periodic hole arrays [115-117] or metallic structures with a single aperture [118-123]. Based on Bethe's theoretical description, transmission through a single subwavelength aperture of a radius $r << \lambda$ scales with $(r/\lambda)^4$ [124]. However, one can increase the amount of light passing through a single hole by corrugating the metal surface with periodic grooves [123], by filling the hole with a material of high dielectric permittivity [119, 122], by using alternative aperture geometries [120, 121] or by placing artificially designed metamaterial covers in front of the aperture [118]. In all of the approaches, transmission is enhanced by a resonant process that leads to the effective coupling of light to a small aperture. Although much of the work on enhanced transmission has been carried out at

optical frequencies, similar results are also obtained at microwave [125, 126] and THz [127] frequency regimes.

In this chapter, we propose and demonstrate an alternative approach that utilizes the resonance of a split-ring resonator (SRR) in order to enhance the transmission of electromagnetic waves at the microwave frequency regime. We successfully demonstrated the extraordinary transmission of microwave radiation through an aperture of radius *r*, which is twenty times smaller than the incident wavelength (r/λ = 0.05). To our knowledge, this is the smallest aperture size utilized for achieving enhanced transmission. We measured a 740-fold enhancement by using electrically coupled SRR in the proximity of a single aperture. However, it is also possible to enhance the transmission by exciting the magnetic resonance of SRRs. Enhanced transmission is attributed to the highly localized electric fields at the resonance frequency of split ring resonators that couple incident EM radiation to the aperture.

7.2. Enhanced transmission by coupling to the electric resonance of SRR

Figure 7.1(a) shows the schematics of the structure under investigation. A commercial 1.6 mm thick FR4 printed circuit board deposited with a thin (30 μm) copper plate of the size L x L (L = 200 mm) was used in the experiments. A circular aperture with a radius of r = 4 mm at the center of a metallic plate was created by mechanical etching. In the experiments, a split-ring resonator was used to couple electromagnetic waves to the aperture at a resonance frequency of SRR. The split ring resonator was comprised of two concentric rings with the parameters as provided in chapter 2. The radius of the SRR is 3.6 mm, which is comparable with the aperture size. Figure 7.1(b) shows an alternative configuration of placing SRR in front of the aperture, wherein a different resonance mechanism (magnetic resonance) plays a role in the enhanced transmission.

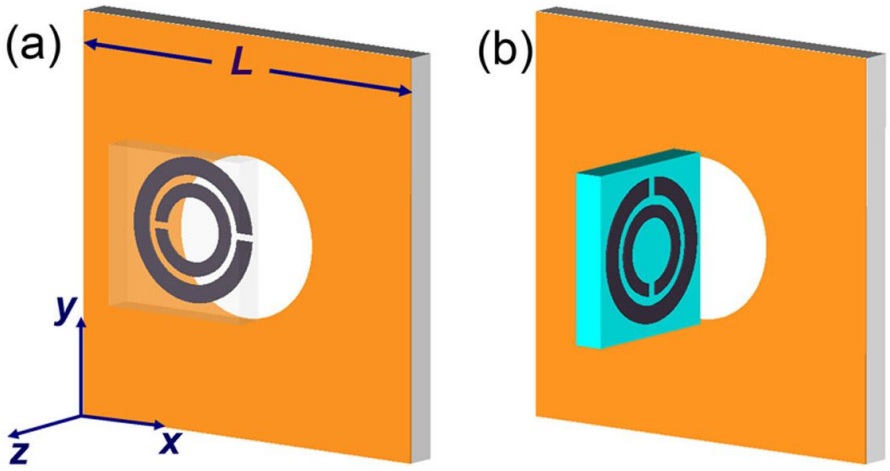

Figure 7.1: Schematic drawings of a subwavelength aperture in a metallic plate and SRR plane (a) parallel, and (b) perpendicular to the aperture plane.

The resonance of a single SRR for a different configuration and the incident polarization of an electromagnetic wave were studied simply by measuring the transmission spectrum. Transmission measurements were performed by using two waveguides as a transmitter and receiver, which were connected to the Agilent N5230A portable network analyzer. Four different orientations of SRR with respect to the incident EM wave were investigated, in which the results are shown in Fig. 7.2. For the structures SRR (A) and SRR (B), the wave propagation was perpendicular to the plane of SRRs, i.e. along the z' axis. Magnetic resonance cannot be excited with perpendicular propagation, since the *H*-field is parallel to the SRR plane. However, it is possible to excite an electrical resonance for SRR (A), where *E* is along the y', and *H* is along the x' due to the asymmetry of the SRR structure with respect to the electric field of the incident EM wave [49]. The resonance frequency for SRR (A) is measured at 3.55 GHz. For the SRR (B) case, where $E \,//\, x'$ and $H \,//\, y'$, the transmission resonance was not observed, since the structure is symmetric with respect to the *E*-field.

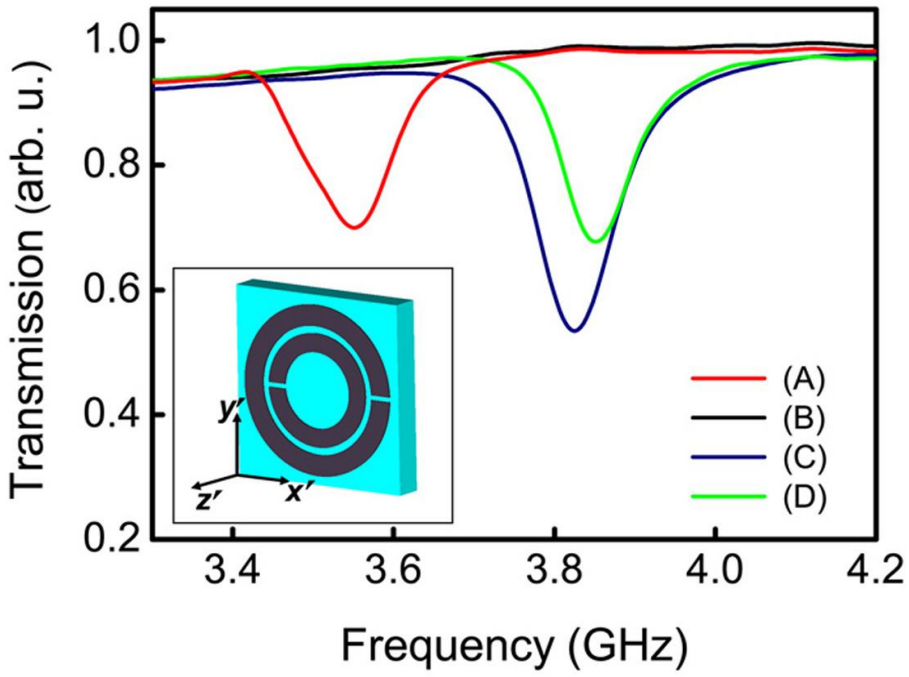

Figure 7.2: Measured transmission spectra from a single SRR with four different orientations.

The magnetic resonance in SRRs could only be excited when *H* was perpendicular to the plane of SRR. For the configurations SRR (C) and SRR (D), the wave propagates parallel to the SRR plane, whereas the *H*-field is perpendicular (along the *z′* axis). The wave propagates along the *x′* and E-field is along the *y′* for SRR (C). Both electric and magnetic fields contribute to the resonance mechanism of SRRs for configuration (C) [49]. The resonance of SRR (D) is purely of magnetic origin since E is along *x′*, which is symmetric with the orientation of the splits. The resonance frequencies were measured as 3.82 GHz for SRR (C) and 3.85 GHz for SRR (D).

In the measurements, we employed two waveguide antennae to transmit and receive electromagnetic waves. A transmitter antenna was placed 0.1 mm away from the metallic plate with the aperture and the transmitted power was collected 5 cm away from the structure. Wave propagation was along the *z* axis, where *E*-field

and *H*-field were oriented along the *y* and *x* directions, as shown in Fig. 7.1(a). We first measured the transmission through the reference sample, which was the metallic plate with a single subwavelength aperture. The measured intensity through the aperture was plotted with a red dashed line as shown in Fig. 2(a). As expected from the diffraction theory, the transmission of electromagnetic waves through a small aperture was insignificant [124]. We then placed a single SRR, 0.1 mm away from the aperture with the outer split region facing the center of the aperture as shown in Fig. 7.1(a). The blue line in Fig. 7.3 plots the measured intensity of the EM wave, which propagated through the SRR (A) structure and aperture. The transmission is significantly increased when a single SRR was placed at the near-field of the aperture. We observed a 740-fold enhancement in the transmission at 3.55 GHz (inset). Here, we define the enhancement as the ratio of the field intensity of a transmitted EM wave through an SRR and aperture to that through the aperture only.

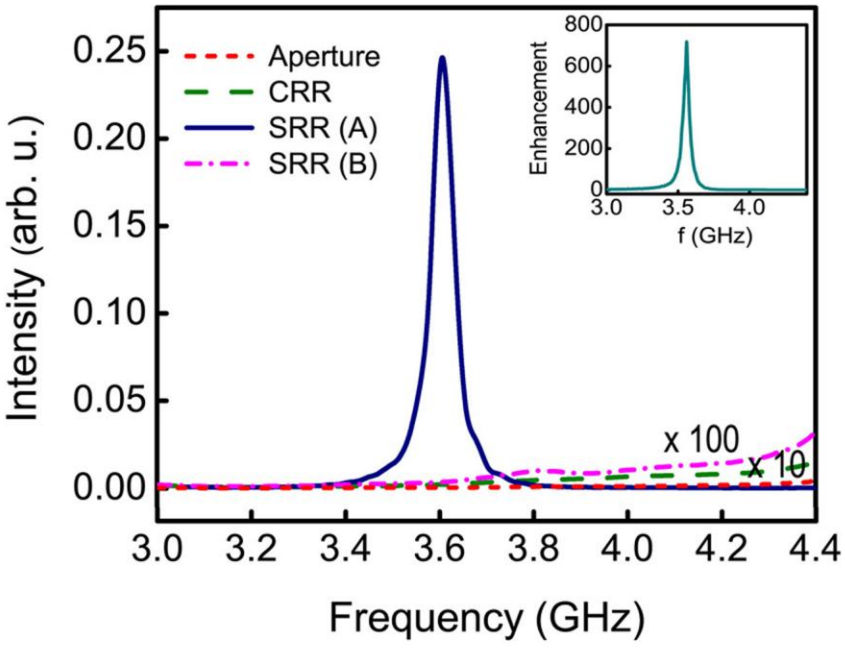

Figure 7.3: Measured intensity of transmitted EM wave from only aperture, and aperture covered with CRR, SRR (A) and SRR (B).

It is noteworthy that the maximum enhancement was obtained at the resonance frequency of SRR (A). The electrically excited resonance of SRR causes the strong localization of the electric field at the splits and gaps of an SRR structure. The resonance of SRR is responsible for the enhancement in the transmission. In order to verify this evidence, we performed additional measurements. We placed a closed ring resonator (CRR), in which the structure comprised of two concentric rings without splits. Evidently, the resonance behavior was no longer present for CRR and the transmission was comparable with that of the aperture-only structure. We also checked the SRR (B) configuration together with the aperture, for which E // x and H // y. As seen in Fig. 7.2, the electrical resonance could not be excited for this configuration. Since the resonant coupling of EM waves to the aperture lacks in this case, we did not observe an enhanced transmission for the SRR (B) case. In our approach, where we utilized a bianisotropic SRR, the enhancement of microwave radiation depends on the polarization of the incident EM wave. It has been previously shown that apertures with rectangular [120, 121] and elliptical [116] shapes yield enhanced transmission for a specific polarization of an incident EM wave. Here, we achieved strong polarization dependence of enhanced transmission through a circular aperture by using a bianisotropic SRR structure.

Numerical simulations were performed by using the commercially available software, CST Microwave Studio. In the simulations, we employed perfect electric conductor approximation for the metals, since the metals were good conductors at microwave frequencies. The dielectric constant and tangent loss of the FR4 dielectric substrate were taken as $\varepsilon = 3.6$ and $\delta = 0.01$, respectively. We modeled the waveguide antennae that were used in the experiments to transmit and detect the electromagnetic waves. Open boundary conditions were applied along all the directions. Figure 7.4 shows the numerical simulation results for only aperture, CRR, SRR (A) and SRR (B) configurations. There was a good agreement between the measured and simulated results. In the simulations, the maximum transmission through SRR (A) and aperture is observed at 3.70 GHz and the enhancement factor

is calculated as 820 (inset). The differences between the measured and simulated results were attributed to the deviation from the ideal material parameters and the sensitivity of the distance between the SRR and aperture on the transmission.

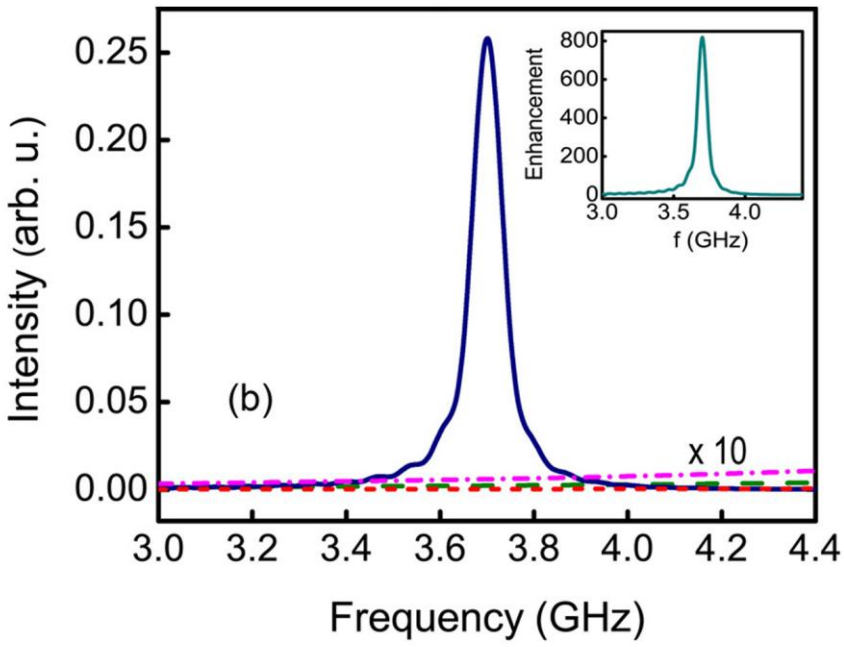

Figure 7.4: Simulated intensity of transmitted EM wave from only aperture, and aperture covered with CRR, SRR (A) and SRR (B).

7.3. Enhanced transmission by coupling to the magnetic resonance of SRR

The maximum transmission enhancement was obtained when the outer split region of SRR coincided with the center of the aperture. The incident EM wave was normal to the SRR structure, which dictates that the magnetic field is parallel to the SRR plane. The resonance did not originate from the magnetic field but the electric field was responsible for the resonant behavior. One can also achieve

enhanced transmission through SRR and aperture with a different resonance mechanism, which is the magnetic resonance of SRR. A single SRR is placed in front of the aperture, as is schematically drawn in Fig. 7.1(b). SRR (D) is symmetric with respect to the *E*-field, whereas SRR (C) is antisymmetric. The corresponding results are plotted in Fig. 7.5(a) and Fig. 7.5(b). SRR's positions with respect to the aperture are shown in the figure insets.

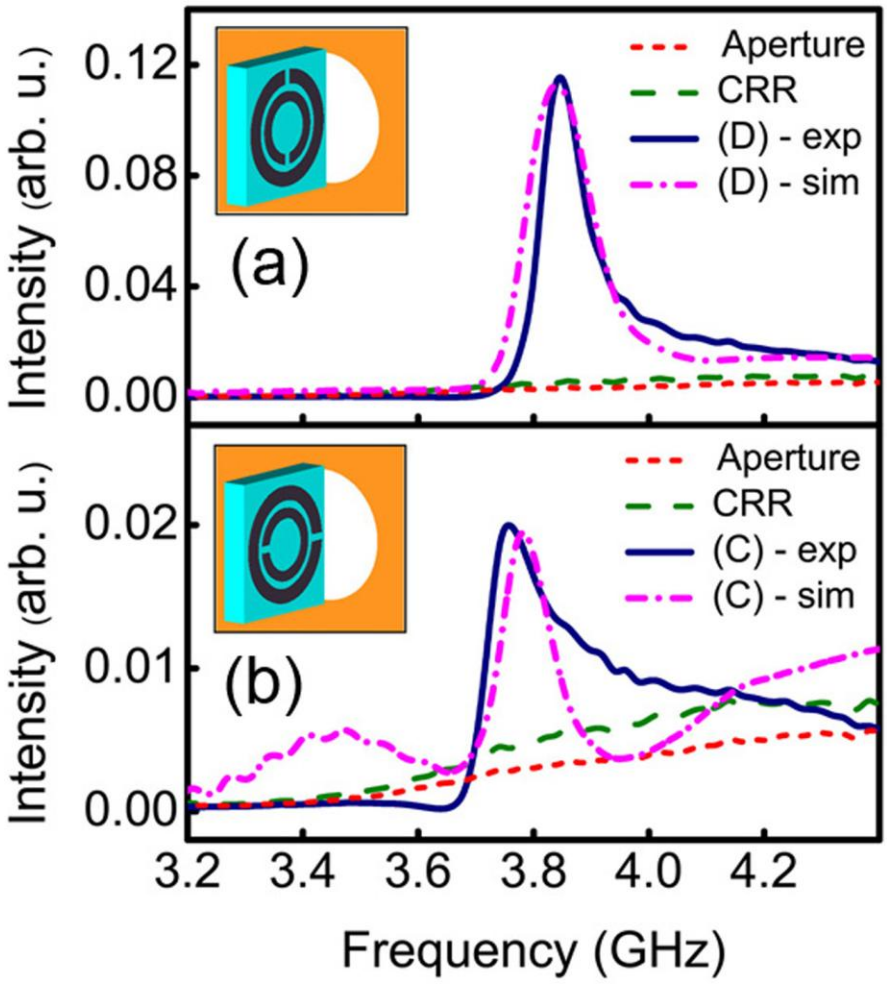

Figure 7.5: Measured and simulated intensity of transmitted EM waves from a single aperture covered with (a) SRR (D) and (b) SRR (C).

Measurements (solid blue line) and simulations (dashed dotted line) revealed that the transmission through the subwavelength aperture was increased for both SRR configurations. Configuration (D) yielded a higher transmission compared to that of configuration (C). The magnetic field excited the resonance in both orientations. However, due to the asymmetry of the SRR (C) structure with respect to the incident *E*-field, there occurred an electric coupling to the magnetic resonance, which was not present in SRR (D). Obviously, additional electric resonance hinders the performance of enhanced transmission through SRR and aperture. Enhancement was measured to be 38 for configuration (D) at 3.84 GHz and 7.5 for configuration (C) at 3.76 GHz as plotted in Fig. 7.6. The simulation results were consistent with the experiments where we calculated the enhancement factors of 34 and 7.8 for (D) and (C) configurations.

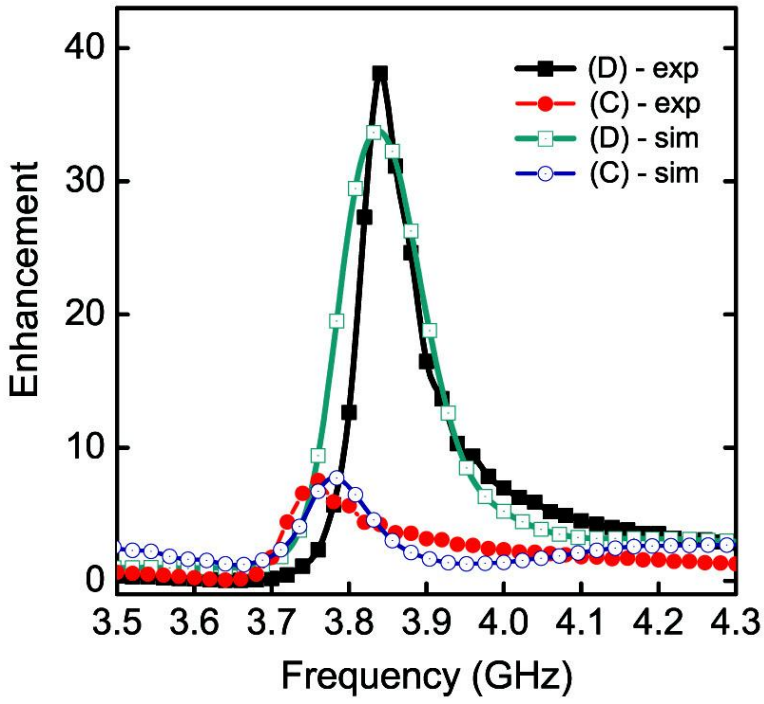

Figure 7.6: Enhancement factors obtained from the measurements and simulations for configurations (C) and (D).

7.4. Strong localization of electric field and coupling mechanism

In order to gain insight to the physical mechanisms behind the transmission enhancement processes, we performed additional numerical simulations to evaluate the amplitude of the electric field at frequencies where our simulations predicted the highest transmission. We used plane wave excitation and monitored *E* field by using the field monitor facility of CST. Figure 7.7(a) plots the amplitude of E_y evaluated at y=0 plane, corresponding to the center of the structure. The amplitude of the electric field of the incident plane wave was unity. The wave was incident from –z and propagated along the +z direction. The aperture was located at z=0, between x/r = -1 and x/r = 1. In the figures, the x and z values were given in terms of the radius of the aperture r, which was 4 mm. The solid rectangles showed the positions of the dielectric FR4 substrates on which the SRR and metallic plate were deposited. It is clearly seen that the electric fields were strongly localized at two different points, which correspond to the split regions of the SRR. By placing a single SRR at the near-field of a subwavelength sized aperture, one can couple the focused electromagnetic waves to the aperture.

Figure 7.7(b) shows the E_y amplitude for the SRR (D) configuration that is evaluated at y=3 plane, where the outer split of the SRR is located. The incident EM wave was coupled through the aperture via the magnetic resonance of SRR. The amplitude of E_y for the SRR (C) and aperture at y=0 plane is shown in Fig. 7.7(c). Although the field enhancement is higher for the SRR (C) structure compared to that of SRR (D), the transmitted electromagnetic wave is apparently smaller.

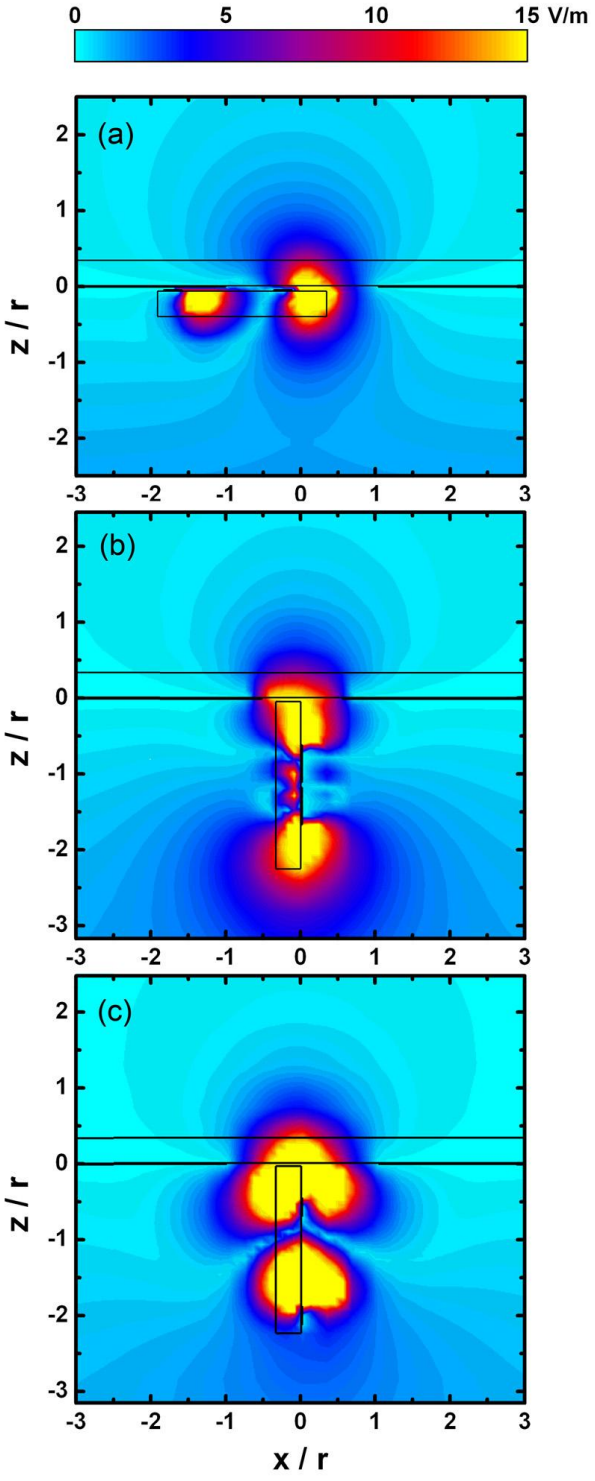

Figure 7.7: Simulated E_y magnitude for an aperture and (a) SRR (A), (b) SRR (D) and (c) SRR (C) structure.

In all of the experiments and simulations, the aperture radius was 20 times smaller than the wavelength ($r/\lambda = 0.05$), whereas the typical aperture sizes utilized to achieve enhanced transmission was $r/\lambda = 0.20$ [123]. We were able to transmit light through a single aperture that was four times smaller than the size of conventional subwavelength apertures. In our experiments, we successfully showed that an enhanced transmission was achieved around the resonance frequency of SRR, where the resonance wavelength was much larger than the size of SRR. Since the frequency of an enhanced transmission was determined by the resonance frequency of SRR, one can employ an active SRR medium [128] to tune the wavelength of maximum enhancement. Utilizing SRR also provides design flexibility, in which one can easily fabricate SRRs to resonate at a desired frequency. Here, we used a single SRR and a single subwavelength aperture in order to show the possibility of enhancing the transmission of electromagnetic waves. We believe that the optimization of aperture size, SRRs distance and place could yield to more efficient coupling and thus increasing the amount of enhancement. Even more interesting results could be achieved by utilizing periodic aperture and SRR arrays.

Our experiments were carried out at microwave frequencies, but similar results could also be obtained from THz [54] to near IR [129] frequencies, since SRRs have already been realized at these frequency regimes. Optical antennae were fabricated in front of a subwavelength aperture to achieve an enhanced transmission at optical frequencies, since the fields were strongly localized in the antenna feed [130], very much like the localization of fields at the SRRs split region. It is noteworthy that the metals are perfect conductors at microwave frequencies and, therefore, localized surface plasmons do not contribute to the enhancement process. Furthermore, surface waves were not present in our approach, since we did not use a grating structure to enhance the radiation. The strongly localized fields around the SRR couple the EM waves through a resonant process to the subwavelength aperture.

Chapter 8

Conclusion

The aim of this thesis was to understand the physics of metamaterials with a focus on negative-index metamaterials and their applications at microwave frequencies. We characterized metamaterials with negative permittivity, negative permeability and negative refractive index by using experimental and numerical techniques.

In chapter 2, we studied the building block of a metamaterial which is called a split-ring resonator (SRR). The resonance behavior of such resonators is verified by measuring and simulating transmission through a single SRR unit cell. A comparison is made with another structure so called closed ring resonator (CRR), in which the splits of SRR are removed. The magnetic resonance is disappeared for the CRR structure. A periodic arrangement of SRR and CRR arrays are utilized to investigate the transmission characteristics of such resonator arrays. Negative permeability region is found at magnetic resonance frequency where a band gap appeared in the transmission spectrum. We further investigated the effect of SRR's parameters on the resonance frequency of SRR. Additionally we proposed using capacitor loaded SRRs to tune the magnetic resonance frequency.

Chapter 3 studied the left-handed metamaterials (LHM) in detail. We have successfully demonstrated a left-handed transmission band for an LHM that is

comprised of split-ring resonator and wire arrays. Retrieval procedure is used to calculate the effective parameters of the left-handed metamaterial. It is found out that the permeability, permittivity and refractive index possesses negative values within the left-handed transmission band. We also studied reflection characteristics of one-dimensional LHMs and observed very low reflection at frequencies where the real parts of permittivity and permeability are equal, indicating an impedance-matched frequency. We confirmed that 2D negative-index metamaterial has a negative refractive index at frequencies where dielectric permittivity and magnetic permeability are simultaneously negative. We have been able to observe negative refractive index for 2D NIMs by using three different, independent methods. By measuring the refraction from prism-shaped and slab-shaped NIM structures, we calculated the refractive index for the metamaterials. The results obtained from these experiments are in good agreement. Phase shift and therefore phase velocity is shown to be negative.

In chapter 4, the flat lens behavior of a 2D LHM slab is investigated for a point source, located at two different distances away from the air-LHM interface. Subwavelength focusing is achieved along the longitudinal and lateral direction. A free space flat-lens made of an all-angle negative refractive index LHM with low reflection is successfully demonstrated. The source is then places inside an LHM flat lens and focusing behavior is verified.

We have demonstrated subwavelength imaging with a SRR-wire geometry based NIM superlens in the near-field zone in chapter 5. We have been able to obtain images with resolution of 0.14λ from a single point source, which is the highest resolution achieved by a negative-index metamaterial. The resolution is not limited by the wavelength, but losses and periodicity affects the superlens performance. The NIM structure has considerably low-losses with a figure of merit of 12 and thus can be used in microwave imaging applications. Moreover, two sources separated with a distance of $\lambda/8$ are resolved clearly. Effect of thickness on

the subwavelength resolution is verified experimentally. Thicker superlens substantially reduced the resolution down to 0.25λ.

In chapter 6, we demonstrated backward wave propagation in a negative-index metamaterial at microwave frequencies. The advantages of our design are: (i) low-loss substrate in turn providing high transmission even for a five-layer NIM, (ii) negative-index behavior is present independent of the incident electromagnetic wave polarization, due to the symmetric configuration of the slab and wire pairs. We measured the highest transmission for a planar multi-layer structure with -3.7 dB transmission for two-layers and -5.0 dB for five-layers. The retrieved parameters for single and two layer NIM structures differ. The absolute values of ε, μ, and n are higher for a one-layer NIM structure. Negative phase velocity was experimentally verified by measuring the phase difference between those NIM structures with a different number of layers along the propagation direction. The transmitted phase decreases with an increase in the NIM size at the negative-index transmission band. Numerical simulations verified the backward wave propagation within the fishnet metamaterial.

Finally in chapter 7, we successfully demonstrated the enhanced transmission of microwave radiation through a single subwavelength aperture by the placement of a single resonant element in the proximity of the aperture. The resonant element was a split-ring resonator, in which the resonance wavelength was much larger than the size of an SRR. The enhanced transmission was achieved by exciting the electric and/or magnetic resonance of SRR. A 740-fold enhancement was obtained through an aperture that was twenty times smaller than the wavelength. We also found that there was strong polarization dependence for enhancing the transmission, due to the bianisotropic nature of a split-ring resonator.

Bibliography

1. D. R. Smith, W. J. Padilla, D. C. Vier, S. C. Nemat-Nasser, and S. Schultz, "Composite medium with simultaneously negative permeability and permittivity," Phys Rev Lett 84, 4184-4187 (2000).

2. V. G. Veselago, "The electrodynamics of substances with simultaneously negative values of permittivity and permeability," Sov. Phys. Usp. 10, 504-509 (1968).

3. J. B. Pendry, A. J. Holden, D. J. Robbins, and W. J. Stewart, "Magnetism from conductors and enhanced nonlinear phenomena," IEEE Trans Microw Theory 47, 2075-2084 (1999).

4. G. Veselago, and E. E. Narimanov, "The left hand of brightness: past, present and future of negative index materials," Nature Mater 5, 759-762 (2006).

5. C. Caloz, and T. Itoh, *Electromagnetic Metamaterials: Transmission Line Theory and Microwave Applications* (Wiley-IEEE Press, 2005).

6. G. V. Eleftheriades, and K. G. Balmain, *Negative Refraction Metamaterials: Fundamental Principles and Applications* (Wiley-IEEE Press, 2005).

7. R. Marques, F. Martin, and M. Sorolla, *Metamaterials with Negative Parameters: Theory, Design and Microwave Applications* (Wiley, 2008).

8. A. K. Sarychev, and V. M. Shalaev, *Electrodynamics of Metamaterials* (World Scientific Publishing Company, 2007).

9. N. Engheta, R. W. Ziolkowski, ed. *Electromagnetic Metamaterials: Physics and Engineering Explorations* (Wiley-IEEE Press, 2006).

10. R. A. Shelby, D. R. Smith, and S. Schultz, "Experimental verification of a negative index of refraction," Science 292, 77-79 (2001).

11. E. Cubukcu, K. Aydin, E. Ozbay, S. Foteinopoulou, and C. M. Soukoulis, "Negative refraction by photonic crystals," Nature 423, 604-605 (2003).

12. S. Foteinopoulou, E. N. Economou, and C. M. Soukoulis, "Refraction in media with a negative refractive index," Phys Rev Lett 90, 107402 (2003).

13. C. Luo, S. G. Johnson, J. D. Joannopoulos, and J. B. Pendry, "All-angle negative refraction without negative effective index," Phys Rev B 65, 201104 (2002).

14. C. Y. Luo, S. G. Johnson, J. D. Joannopoulos, and J. B. Pendry, "Negative refraction without negative index in metallic photonic crystals," Opt Express 11, 746-754 (2003).

15. P. V. Parimi, W. T. Lu, P. Vodo, J. Sokoloff, J. S. Derov, and S. Sridhar, "Negative refraction and left-handed electromagnetism in microwave photonic crystals," Phys Rev Lett 92, 127401 (2004).

16. H. J. Lezec, J. A. Dionne, and H. A. Atwater, "Negative refraction at visible frequencies," Science 316, 430-432 (2007).

17. A. J. Hoffman, L. Alekseyev, S. S. Howard, K. J. Franz, D. Wasserman, V. A. Podolskiy, E. E. Narimanov, D. L. Sivco, and C. Gmachl, "Negative refraction in semiconductor metamaterials," Nature Mater 6, 946-950 (2007).

18. J. B. Pendry, "Negative refraction makes a perfect lens," Phys Rev Lett 85, 3966-3969 (2000).

19. K. Aydin, I. Bulu, and E. Ozbay, "Subwavelength resolution with a negative-index metamaterial superlens," Appl Phys Lett 90, 254102 (2007).

20. W. S. Cai, D. A. Genov, and V. M. Shalaev, "Superlens based on metal-dielectric composites," Phys Rev B 72, 193101 (2005).

21. N. Fang, H. Lee, C. Sun, and X. Zhang, "Sub-diffraction-limited optical imaging with a silver superlens," Science 308, 534-537 (2005).

22. N. Fang, and X. Zhang, "Imaging properties of a metamaterial superlens," Appl Phys Lett 82, 161-163 (2003).

23. A. Grbic, and G. V. Eleftheriades, "Overcoming the diffraction limit with a planar left-handed transmission-line lens," Phys Rev Lett 92, 117403 (2004).

24. P. G. Kik, S. A. Maier, and H. A. Atwater, "Image resolution of surface-plasmon-mediated near-field focusing with planar metal films in three dimensions using finite-linewidth dipole sources," Phys Rev B 69, 045418 (2004).

25. A. N. Lagarkov, and V. N. Kissel, "Near-perfect imaging in a focusing system based on a left-handed-material plate," Phys Rev Lett 92, 077401 (2004).

26. D. O. S. Melville, and R. J. Blaikie, "Super-resolution imaging through a planar silver layer," Opt Express 13, 2127-2134 (2005).

27. J. B. Pendry, and D. R. Smith, "The quest for the superlens," Sci Am 295, 60-67 (2006).

28. X. Zhang, and Z. Liu, "Superlenses to overcome the diffraction limit," Nature Mater 7, 435-441 (2008).

29. Z. Jacob, L. V. Alekseyev, and E. Narimanov, "Optical hyperlens: Far-field imaging beyond the diffraction limit," Opt Express 14, 8247-8256 (2006).

30. Z. W. Liu, H. Lee, Y. Xiong, C. Sun, and X. Zhang, "Far-field optical hyperlens magnifying sub-diffraction-limited objects," Science 315, 1686-1686 (2007).

31. I. I. Smolyaninov, Y. J. Hung, and C. C. Davis, "Magnifying superlens in the visible frequency range," Science 315, 1699-1701 (2007).

32. J. B. Pendry, D. Schurig, and D. R. Smith, "Controlling electromagnetic fields," Science 312, 1780-1782 (2006).

33. W. S. Cai, U. K. Chettiar, A. V. Kildishev, and V. M. Shalaev, "Optical cloaking with metamaterials," Nature Photonics 1, 224-227 (2007).

34. D. Schurig, J. J. Mock, B. J. Justice, S. A. Cummer, J. B. Pendry, A. F. Starr, and D. R. Smith, "Metamaterial electromagnetic cloak at microwave frequencies," Science 314, 977-980 (2006).

35. B. Edwards, A. Alu, M. E. Young, M. Silveirinha, and N. Engheta, "Experimental verification of epsilon-near-zero metamaterial coupling and energy squeezing using a microwave waveguide," Phys Rev Lett 100, 033903 (2008).

36. R. Liu, Q. Cheng, T. Hand, J. J. Mock, T. J. Cui, S. A. Cummer, and D. R. Smith, "Experimental demonstration of electromagnetic tunneling through an

epsilon-near-zero metamaterial at microwave frequencies," Phys Rev Lett 100, 023903 (2008).

37. J. F. Zhou, T. Koschny, M. Kafesaki, and C. M. Soukoulis, "Size dependence and convergence of the retrieval parameters of metamaterials," Photonic Nanostruct 6, 96-101 (2008).

38. M. C. K. Wiltshire, J. B. Pendry, and J. V. Hajnal, "Sub-wavelength imaging at radio frequency," J Phys-Condens Mat 18, L315-L321 (2006).

39. M. C. K. Wiltshire, J. B. Pendry, I. R. Young, D. J. Larkman, D. J. Gilderdale, and J. V. Hajnal, "Microstructured magnetic materials for RF flux guides in magnetic resonance imaging," Science 291, 849-851 (2001).

40. R. A. Shelby, D. R. Smith, S. C. Nemat-Nasser, and S. Schultz, "Microwave transmission through a two-dimensional, isotropic, left-handed metamaterial," Appl Phys Lett 78, 489-491 (2001).

41. M. Bayindir, K. Aydin, E. Ozbay, P. Markos, and C. M. Soukoulis, "Transmission properties of composite metamaterials in free space," Appl Phys Lett 81, 120-122 (2002).

42. A. Grbic, and G. V. Eleftheriades, "Experimental verification of backward-wave radiation from a negative refractive index metamaterial," J Appl Phys 92, 5930-5935 (2002).

43. A. A. Houck, J. B. Brock, and I. L. Chuang, "Experimental observations of a left-handed material that obeys Snell's law," Phys Rev Lett 90, 137401 (2003).

44. K. Li, S. J. McLean, R. B. Greegor, C. G. Parazzoli, and M. H. Tanielian, "Free-space focused-beam characterization of left-handed materials," Appl Phys Lett 82, 2535-2537 (2003).

45. C. G. Parazzoli, R. B. Greegor, K. Li, B. E. C. Koltenbah, and M. Tanielian, "Experimental verification and simulation of negative index of refraction using Snell's law," Phys Rev Lett 90, 107401 (2003).

46. K. Aydin, K. Guven, M. Kafesaki, L. Zhang, C. M. Soukoulis, and E. Ozbay, "Experimental observation of true left-handed transmission peaks in metamaterials," Opt Lett 29, 2623-2625 (2004).

47. K. Aydin, K. Guven, N. Katsarakis, C. M. Soukoulis, and E. Ozbay, "Effect of disorder on magnetic resonance band gap of split-ring resonator structures," Opt Express 12, 5896-5901 (2004).

48. N. Katsarakis, T. Koschny, M. Kafesaki, E. N. Economou, E. Ozbay, and C. M. Soukoulis, "Left- and right-handed transmission peaks near the magnetic resonance frequency in composite metamaterials," Phys Rev B 70, 201101 (2004).

49. N. Katsarakis, T. Koschny, M. Kafesaki, E. N. Economou, and C. M. Soukoulis, "Electric coupling to the magnetic resonance of split ring resonators," Appl Phys Lett 84, 2943-2945 (2004).

50. K. Aydin, K. Guven, C. M. Soukoulis, and E. Ozbay, "Observation of negative refraction and negative phase velocity in left-handed metamaterials," Appl Phys Lett 86, 124102 (2005).

51. I. Bulu, H. Caglayan, K. Aydin, and E. Ozbay, "Compact size highly directive antennas based on the SRR metamaterial medium," New J Phys 7, 223 (2005).

52. I. Bulu, H. Caglayan, and E. Ozbay, "Experimental demonstration of labyrinth-based left-handed metamaterials," Opt Express 13, 10238-10247 (2005).

53. M. Gokkavas, K. Guven, I. Bulu, K. Aydin, R. S. Penciu, M. Kafesaki, C. M. Soukoulis, and E. Ozbay, "Experimental demonstration of a left-handed metamaterial operating at 100 GHz," Phys Rev B 73, 193103 (2006).

54. T. J. Yen, W. J. Padilla, N. Fang, D. C. Vier, D. R. Smith, J. B. Pendry, D. N. Basov, and X. Zhang, "Terahertz magnetic response from artificial materials," Science 303, 1494-1496 (2004).

55. S. Linden, C. Enkrich, M. Wegener, J. F. Zhou, T. Koschny, and C. M. Soukoulis, "Magnetic response of metamaterials at 100 terahertz," Science 306, 1351-1353 (2004).

56. H. O. Moser, B. D. F. Casse, O. Wilhelmi, and B. T. Saw, "Terahertz response of a microfabricated rod-split-ring-resonator electromagnetic metamaterial," Phys Rev Lett 94, 063901 (2005).

57. V. M. Shalaev, "Optical negative-index metamaterials," Nature Photonics 1, 41-48 (2007).

58. V. M. Shalaev, W. S. Cai, U. K. Chettiar, H. K. Yuan, A. K. Sarychev, V. P. Drachev, and A. V. Kildishev, "Negative index of refraction in optical metamaterials," Opt Lett 30, 3356-3358 (2005).

59. S. Zhang, W. J. Fan, K. J. Malloy, S. R. J. Brueck, N. C. Panoiu, and R. M. Osgood, "Near-infrared double negative metamaterials," Opt Express 13, 4922-4930 (2005).

60. S. Zhang, W. J. Fan, N. C. Panoiu, K. J. Malloy, R. M. Osgood, and S. R. J. Brueck, "Experimental demonstration of near-infrared negative-index metamaterials," Phys Rev Lett 95, 137404 (2005).

61. W. S. Cai, U. K. Chettiar, H. K. Yuan, V. C. de Silva, A. V. Kildishev, V. P. Drachev, and V. M. Shalaev, "Metamagnetics with rainbow colors," Opt Express 15, 3333-3341 (2007).

62. G. Dolling, M. Wegener, C. M. Soukoulis, and S. Linden, "Negative-index metamaterial at 780 nm wavelength," Opt Lett 32, 53-55 (2007).

63. K. Aydin, I. Bulu, K. Guven, M. Kafesaki, C. M. Soukoulis, and E. Ozbay, "Investigation of magnetic resonances for different split-ring resonator parameters and designs," New J Phys 7, 168 (2005).

64. K. Aydin, and E. Ozbay, "Identifying magnetic response of split-ring resonators at microwave frequencies," Opto-Electron Rev 14, 193-199 (2006).

65. K. Aydin, and E. Ozbay, "Experimental and numerical analyses of the resonances of split ring resonators," Phys Status Solidi B 244, 1197-1201 (2007).

66. E. Ozbay, K. Guven, and K. Aydin, "Metamaterials with negative permeability and negative refractive index: experiments and simulations," J Opt A-Pure Appl Op 9, S301-S307 (2007).

67. K. Aydin, and E. Ozbay, "Capacitor-loaded split ring resonators as tunable metamaterial components," J Appl Phys 101, 024911 (2007).

68. X. D. Chen, T. M. Grzegorczyk, B. I. Wu, J. Pacheco, and J. A. Kong, "Robust method to retrieve the constitutive effective parameters of metamaterials," Phys Rev E 70, 016608 (2004).

69. J. Garcia-Garcia, F. Martin, J. D. Baena, R. Marques, and L. Jelinek, "On the resonances and polarizabilities of split ring resonators," J Appl Phys 98, 033103 (2005).

70. P. Gay-Balmaz, and O. J. F. Martin, "Electromagnetic resonances in individual and coupled split-ring resonators," J Appl Phys 92, 2929-2936 (2002).

71. P. Markos, and C. M. Soukoulis, "Numerical studies of left-handed materials and arrays of split ring resonators," Phys Rev E 65, 036622 (2002).

72. R. Marques, F. Medina, and R. Rafii-El-Idrissi, "Role of bianisotropy in negative permeability and left-handed metamaterials," Phys Rev B 65, 144440 (2002).

73. R. Marques, F. Mesa, J. Martel, and F. Medina, "Comparative analysis of edge- and broadside-coupled split ring resonators for metamaterial design - Theory and experiments," IEEE Trans Antenn Propag 51, 2572-2581 (2003).

74. A. Radkovskaya, M. Shamonin, C. J. Stevens, G. Faulkner, D. J. Edwards, E. Shamonina, and L. Solymar, "Resonant frequencies of a combination of split rings: Experimental, analytical and numerical study," Microw Opt Techn Let 46, 473-476 (2005).

75. B. Sauviac, C. R. Simovski, and S. A. Tretyakov, "Double split-ring resonators: Analytical modeling and numerical simulations," Electromagnetics 24, 317-338 (2004).

76. M. Shamonin, E. Shamonina, V. Kalinin, and L. Solymar, "Properties of a metamaterial element: Analytical solutions and numerical simulations for a singly split double ring," J Appl Phys 95, 3778-3784 (2004).

77. M. Shamonin, E. Shamonina, V. Kalinin, and L. Solymar, "Resonant frequencies of a split-ring resonator: Analytical solutions and numerical simulations," Microw Opt Techn Let 44, 133-136 (2005).

78. J. Zhou, T. Koschny, M. Kafesaki, E. N. Economou, J. B. Pendry, and C. M. Soukoulis, "Saturation of the magnetic response of split-ring resonators at optical frequencies," Phys Rev Lett 95, 223902 (2005).

79. J. F. Zhou, T. Koschny, and C. M. Soukoulis, "Magnetic and electric excitations in split ring resonators," Opt Express 15, 17881-17890 (2007).

80. J. B. Pendry, A. J. Holden, W. J. Stewart, and I. Youngs, "Extremely low frequency plasmons in metallic mesostructures," Phys Rev Lett 76, 4773-4776 (1996).

81. J. B. Pendry, A. J. Holden, D. J. Robbins, and W. J. Stewart, "Low frequency plasmons in thin-wire structures," J Phys-Condens Mat 10, 4785-4809 (1998).

82. D. R. Smith, D. C. Vier, W. Padilla, S. C. Nemat-Nasser, and S. Schultz, "Loop-wire medium for investigating plasmons at microwave frequencies," Appl Phys Lett 75, 1425-1427 (1999).

83. K. Aydin, I. Bulu, and E. Ozbay, "Verification of impedance matching at the surface of left-handed materials," Microw Opt Techn Let 48, 2548-2552 (2006).

84. K. Aydin, and E. Ozbay, "Experimental investigation of reflection characteristics of left-handed metamaterials in free space," IET Microw Antenna P 1, 89-93 (2007).

85. X. Chen, B. I. Wu, J. A. Kong, and T. M. Grzegorczyk, "Retrieval of the effective constitutive parameters of bianisotropic metamaterials," Phys Rev E 71, 046610 (2005).

86. T. Koschny, M. Kafesaki, E. N. Economou, and C. M. Soukoulis, "Effective medium theory of left-handed materials," Phys Rev Lett 93, 107402 (2004).

87. T. Koschny, P. Markos, E. N. Economou, D. R. Smith, D. C. Vier, and C. M. Soukoulis, "Impact of inherent periodic structure on effective medium description of left-handed and related metamaterials," Phys Rev B 71, 245105 (2005).

88. T. Koschny, P. Markos, D. R. Smith, and C. M. Soukoulis, "Resonant and antiresonant frequency dependence of the effective parameters of metamaterials," Phys Rev E 68, 065602 (2003).

89. D. R. Smith, S. Schultz, P. Markos, and C. M. Soukoulis, "Determination of effective permittivity and permeability of metamaterials from reflection and transmission coefficients," Phys Rev B 65, 195104 (2002).

90. D. R. Smith, D. C. Vier, T. Koschny, and C. M. Soukoulis, "Electromagnetic parameter retrieval from inhomogeneous metamaterials," Phys Rev E 71, 036617 (2005).

91. D. R. Smith, P. M. Rye, J. J. Mock, D. C. Vier, and A. F. Starr, "Enhanced diffraction from a grating on the surface of a negative-index metamaterial," Phys Rev Lett 93, 137405 (2004).

92. S. A. Cummer, and B. I. Popa, "Wave fields measured inside a negative refractive index metamaterial," Appl Phys Lett 85, 4564-4566 (2004).

93. G. Dolling, C. Enkrich, M. Wegener, C. M. Soukoulis, and S. Linden, "Simultaneous negative phase and group velocity of light in a metamaterial," Science 312, 892-894 (2006).

94. J. D. Wilson, and Z. D. Schwartz, "Multifocal flat lens with left-handed metamaterial," Appl Phys Lett 86, 021113 (2005).

95. P. Vodo, P. V. Parimi, W. T. Lu, and S. Sridhar, "Focusing by planoconcave lens using negative refraction," Appl Phys Lett 86, 201108 (2005).

96. J. B. Brock, A. A. Houck, and I. L. Chuang, "Focusing inside negative index materials," Appl Phys Lett 85, 2472-2474 (2004).

97. E. Cubukcu, K. Aydin, E. Ozbay, S. Foteinopolou, and C. M. Soukoulis, "Subwavelength resolution in a two-dimensional photonic-crystal-based superlens," Phys Rev Lett 91, 207401 (2003).

98. C. Y. Luo, S. G. Johnson, J. D. Joannopoulos, and J. B. Pendry, "Subwavelength imaging in photonic crystals," Phys Rev B 68, 045115 (2003).

99. J. B. Pendry, and S. A. Ramakrishna, "Refining the perfect lens," Physica B 338, 329-332 (2003).

100. V. A. Podolskiy, and E. E. Narimanov, "Near-sighted superlens," Opt Lett 30, 75-77 (2005).

101. D. R. Smith, D. Schurig, M. Rosenbluth, S. Schultz, S. A. Ramakrishna, and J. B. Pendry, "Limitations on subdiffraction imaging with a negative refractive index slab," Appl Phys Lett 82, 1506-1508 (2003).

102. G. Dolling, C. Enkrich, M. Wegener, C. M. Soukoulis, and S. Linden, "Low-loss negative-index metamaterial at telecommunication wavelengths," Opt Lett 31, 1800-1802 (2006).

103. W. T. Lu, and S. Sridhar, "Flat lens without optical axis: Theory of imaging," Opt Express 13, 10673-10680 (2005).

104. P. V. Parimi, W. T. T. Lu, P. Vodo, and S. Sridhar, "Photonic crystals - Imaging by flat lens using negative refraction," Nature 426, 404-404 (2003).

105. K. Guven, M. D. Caliskan, and E. Ozbay, "Experimental observation of left-handed transmission in a bilayer metamaterial under normal-to-plane propagation," Opt Express 14, 8685-8693 (2006).

106. J. F. Zhou, T. Koschny, L. Zhang, G. Tuttle, and C. M. Soukoulis, "Experimental demonstration of negative index of refraction," Appl Phys Lett 88, 221103 (2006).

107. J. F. Zhou, L. Zhang, G. Tuttle, T. Koschny, and C. M. Soukoulis, "Negative index materials using simple short wire pairs," Phys Rev B 73, 041101 (2006).

108. M. Kafesaki, I. Tsiapa, N. Katsarakis, T. Koschny, C. M. Soukoulis, and E. N. Economou, "Left-handed metamaterials: The fishnet structure and its variations," Phys Rev B 75, 235114 (2007).

109. V. D. Lam, J. B. Kim, S. J. Lee, and Y. P. Lee, "Left-handed behavior of combined and fishnet structures," J Appl Phys 103, 033107 (2008).

110. M. Kafesaki, T. Koschny, R. S. Penciu, T. F. Gundogdu, E. N. Economou, and C. M. Soukoulis, "Left-handed metamaterials: detailed numerical studies of the transmission properties," J Opt A-Pure Appl Op 7, S12-S22 (2005).

111. N. Liu, H. C. Guo, L. W. Fu, S. Kaiser, H. Schweizer, and H. Giessen, "Three-dimensional photonic metamaterials at optical frequencies," Nature Mater 7, 31-37 (2008).

112. K. Aydin, and E. Ozbay, "Left-handed metamaterial based superlens for subwavelength imaging of electromagnetic waves," Applied Physics A-Materials Science & Processing 87, 137-141 (2007).

113. C. Genet, and T. W. Ebbesen, "Light in tiny holes," Nature 445, 39-46 (2007).

114. T. W. Ebbesen, H. J. Lezec, H. F. Ghaemi, T. Thio, and P. A. Wolff, "Extraordinary optical transmission through sub-wavelength hole arrays," Nature 391, 667-669 (1998).

115. W. L. Barnes, W. A. Murray, J. Dintinger, E. Devaux, and T. W. Ebbesen, "Surface plasmon polaritons and their role in the enhanced transmission of light through periodic arrays of subwavelength holes in a metal film," Phys Rev Lett 92, 107401 (2004).

116. R. Gordon, A. G. Brolo, A. McKinnon, A. Rajora, B. Leathem, and K. L. Kavanagh, "Strong polarization in the optical transmission through elliptical nanohole arrays," Phys Rev Lett 92, 037401 (2004).

117. L. Martin-Moreno, F. J. Garcia-Vidal, H. J. Lezec, K. M. Pellerin, T. Thio, J. B. Pendry, and T. W. Ebbesen, "Theory of extraordinary optical transmission through subwavelength hole arrays," Phys Rev Lett 86, 1114-1117 (2001).

118. A. Alu, F. Bilotti, N. Engheta, and L. Vegni, "Metamaterial covers over a small aperture," Ieee T Antenn Propag 54, 1632-1643 (2006).

119. F. J. G. I. de Abajo, "Light transmission through a single cylindrical hole in a metallic film," Opt Express 10, 1475-1484 (2002).

120. A. Degiron, H. J. Lezec, N. Yamamoto, and T. W. Ebbesen, "Optical transmission properties of a single subwavelength aperture in a real metal," Opt Commun 239, 61-66 (2004).

121. F. J. Garcia-Vidal, E. Moreno, J. A. Porto, and L. Martin-Moreno, "Transmission of light through a single rectangular hole," Phys Rev Lett 95, 103901 (2005).

122. K. J. Webb, and J. Li, "Analysis of transmission through small apertures in conducting films," Phys Rev B 73, 033401 (2006).

123. H. J. Lezec, A. Degiron, E. Devaux, R. A. Linke, L. Martin-Moreno, F. J. Garcia-Vidal, and T. W. Ebbesen, "Beaming light from a subwavelength aperture," Science 297, 820-822 (2002).

124. H. A. Bethe, "Theory of diffraction by small holes," Physical Review 66, 163-182 (1944).

125. S. S. Akarca-Biyikli, I. Bulu, and E. Ozbay, "Enhanced transmission of microwave radiation in one-dimensional metallic gratings with subwavelength aperture," Appl Phys Lett 85, 1098-1100 (2004).

126. H. Caglayan, I. Bulu, and E. Ozbay, "Extraordinary grating-coupled microwave transmission through a subwavelength annular aperture," Opt Express 13, 1666-1671 (2005).

127. J. G. Rivas, C. Schotsch, P. H. Bolivar, and H. Kurz, "Enhanced transmission of THz radiation through subwavelength holes," Phys Rev B 68, 201306 (2003).

128. H. T. Chen, W. J. Padilla, J. M. O. Zide, A. C. Gossard, A. J. Taylor, and R. D. Averitt, "Active terahertz metamaterial devices," Nature 444, 597-600 (2006).

129. C. Enkrich, M. Wegener, S. Linden, S. Burger, L. Zschiedrich, F. Schmidt, J. F. Zhou, T. Koschny, and C. M. Soukoulis, "Magnetic metamaterials at telecommunication and visible frequencies," Phys Rev Lett 95, 203901 (2005).

130. P. Muhlschlegel, H. J. Eisler, O. J. F. Martin, B. Hecht, and D. W. Pohl, "Resonant optical antennas," Science 308, 1607-1609 (2005).

Appendix A

Publications in SCI Journals

1) M. Bayindir, K. Aydin, E. Ozbay, P. Markos and C. M. Soukoulis, "Transmission properties of composite metamaterials in free space," *Appl. Phys. Lett.* **81**, 120 (2002).
2) E. Cubukcu, K. Aydin, E. Ozbay, S. Foteinopoulou, and C. M. Soukoulis, "Electromagnetic waves: Negative refraction by photonic crystals," *Nature* **423**, 604 (2003).
3) Ekmel Ozbay, Koray Aydin, E. Cubukcu, M. Bayindir, "Transmission and reflection properties of composite double negative metamaterials in free space," *IEEE Trans. Antennas Propag.* **51**, 2592 (2003).
4) E. Cubukcu, K. Aydin, S. Foteinopolou, C. M. Soukoulis, and E. Ozbay, "Subwavelength resolution in a two-dimensional photonic crystal based superlens," *Phys. Rev. Lett.* **91**, 207401 (2003).
5) E.Ozbay, K. Guven, E. Cubukcu, K. Aydin, and B. K. Alici, "Negative refraction and subwavelength focusing using photonic crystals," *Mod. Phys. Lett. B* **18**, 1275 (2004).
6) K. Guven, K. Aydin, K. B. Alici, C. M. Soukoulis, and E. Ozbay, "Spectral negative refraction and point focusing analysis of a two-dimensional left-handed photonic crystal lens," *Phys. Rev. B.* **70**, 205125 (2004).
7) Koray Aydin, K. Guven, L. Zhang, M. Kafesaki, C. M. Soukoulis, and E. Ozbay, "Experimental observation of true left-handed transmission peak in metamaterials," *Opt. Lett.* **29**, 2623 (2004).

8) Koray Aydin, K. Guven, N. Katsarakis, C. M. Soukoulis, and E. Ozbay, “Effect of disorder on magnetic resonance band gap of split-ring resonator structures,” *Opt. Express* **12**, 5896 (2004).

9) E. Ozbay, I. Bulu, K. Aydin, H. Caglayan, K. Guven, and Boratay K. Alici, “Highly directive radiation and negative refraction using photonic crystals,” *Laser Phys.* **15**, 217 (2005).

10) Koray Aydin, K. Guven, C. M. Soukoulis and E. Ozbay, “Observation of negative refraction and negative phase velocity in left-handed metamaterials”, *Appl. Phys. Lett.* **86**, 124102 (2005).

11) Koray Aydin, I. Bulu, K. Guven, M. Kafesaki, C. M. Soukoulis and E. Ozbay, “Investigation of magnetic resonances for different split-ring resonator parameters and designs,” *New J. Phys.* **7**, 168 (2005).

12) I. Bulu, H. Caglayan, K. Aydin, and E. Ozbay, “Compact size highly directive antennas based on SRR metamaterial medium,” *New J. Phys.* **7**, 223 (2005).

13) Koray Aydin, I. Bulu and E. Ozbay, "Focusing of electromagnetic waves by a left-handed metamaterial flat lens", *Opt. Express* **13**, 8753 (2005).

14) K. Guven, K. Aydin, and E. Ozbay "Experimental analysis of true left-handed behavior and transmission properties of composite metamaterials", *Photonics and Nanostruct. - Fund. Appl.* **3**, 75 (2005).

15) Koray Aydin, and E. Ozbay, "Negative refraction through an impedance matched left-handed metamaterial slab," *J. Opt. Soc. Am. B* **23**, 415 (2006).

16) M. Gokkavas, K. Guven, I. Bulu, K. Aydin, R. S. Penciu, M. Kafesaki, C. M. Soukoulis, and E. Ozbay, "Experimental demonstration of a left-handed metamaterial operating at 100 GHz," *Phys. Rev. B* **73**, 193103 (2006).

17) E. Ozbay, I. Bulu, K. Guven, H. Caglayan, and K. Aydin, "Observation of negative refraction and focusing in two-dimensional photonic crystals", *Japanese J. Appl. Phys*. **45**, 6064 (2006).

18) Koray Aydin, and E. Ozbay, "Identifying the magnetic response of split-ring resonators at microwave frequencies" *Opto-Electron. Rev.* **14**, 193 (2006).

19) Koray Aydin, I. Bulu and E. Ozbay, "Verification of impedance matching at the surface of left-handed materials," *Microw. Opt. Tech. Lett.* **48**, 2548 (2006).

20) Koray Aydin, I. Bulu, and E. Ozbay, "Electromagnetic wave focusing from sources inside a two-dimensional left-handed material superlens" *New J. Phys.* **8**, 221 (2006).

21) K. Aydin, and E. Ozbay, "Capacitor-loaded split ring resonators as tunable metamaterial components" *J. Appl. Phys.* **101**, 024911 (2007).

22) K. Aydin, and E. Ozbay, "Experimental investigation of reflection characteristics of left-handed metamaterials in free space" *IET Microw. Antennas Propag.* **1**, 89 (2007).

23) I. Bulu, H. Caglayan, K. Aydin, and E. Ozbay, "Study of the field emitted by a source placed inside a two dimensional left-handed metamaterial" *Opt. Lett.* **32**, 850 (2007).

24) K. Aydin, and E. Ozbay, "Experimental and numerical analyses of the resonances of split-ring resonators" *Phys. Stat. Sol. B.* **244**, 1197 (2007).

25) E. Ozbay, K. Aydin, I. Bulu, and K. Guven, "Negative refraction, subwavelength focusing and beam formation by photonic crystals" *J. Phys. D: Appl. Phys.* **40**, 2652 (2007).

26) Koray Aydin, and E. Ozbay, "Left-handed metamaterial based superlens for subwavelength imaging of electromagnetic waves" *Appl. Phys. A: Mat. Sci. Proc.* **87**, 137 (2007).

27) Koray Aydin, I. Bulu and E.Ozbay, "Subwavelength resolution with a negative-index metamaterial superlens" *Appl. Phys. Lett.* **90**, 254102 (2007).

28) E. Ozbay, K. Guven and K. Aydin, "Metamaterials with negative permeability and negative refractive index: Experiments and simulations" *J. Opt. A.: Pure Appl. Opt.* **9**, S301 (2007).

29) Zhaofeng Li, Koray Aydin, and Ekmel Ozbay, "Highly directional emission from photonic crystals with a wide bandwidth" *Appl. Phys. Lett.* **91**, 121105 (2007).

30) Koray Aydin, Zhaofeng Li, M. Hudlicka, S. A. Tretyakov, Ekmel Ozbay, "Transmission characteristics of bianisotropic metamaterials based on omega shaped metallic inclusions" *New J. Phys.* **9**, 326 (2007).

31) F. Bilotti, A. Toscano, L. Vegni, K. Aydin, K. B. Alici, and E. Ozbay, "Equivalent circuit models for the design of metamaterials based on artificial magnetic inclusions" *IEEE Trans. Microw. Theory Tech.***55**, 2865 (2007).

32) K. Aydin, Z. Li, S. Bilge, and E. Ozbay, "Experimental and numerical study of omega type bianostropic metamaterials combined with a negative permittivity medium" *Photon. Nanostr.: Fundam. Appl.* **6**, 116 (2008).

33) E. Ozbay and K. Aydin, "Negative refraction and imaging beyond the diffraction limit by a two-dimensional left-handed metamaterial" *Photon. Nanostr.: Fundam. Appl*. **6**, 108 (2008).

34) B. Butun, K. Aydin, E. Ulker, S. Cheylan, G. Badenes, M. Forster, U. Scherf, and E. Ozbay, "A hybrid light source with integrated inorganic light-emitting diode and organic polymer distributed feedback grating" *Nanotechnology* **19**, 195202 (2008).

35) Koray Aydin, Z. Li, L. Sahin, and E. Ozbay, "Negative phase advance in polarization independent, multi-layer negative-index metamaterials," *Optics Express* **16**, 8835 (2008).

36) Zhaofeng Li, Koray Aydin, and Ekmel Ozbay, "Wide bandwidth directional beaming via waveguide ports in photonic crystals," *J. Phys. D* (in press).

37) Ekmel Ozbay, Z. Li, and Koray Aydin, "Super-resolution imaging by one-dimensional, microwave left-handed metamaterials with an effective negative-index," *J. Phys. Cond. Matt.* (in press).

38) Koray Aydin, A. O. Cakmak, L. Sahin, Z. Li, F. Bilotti, L. Vegni, and E. Ozbay, "Split-ring resonator coupled enhanced transmission from a single subwavelength aperture," (http://arxiv.org/abs/0805.3907) *submitted to Phys. Rev. Lett.*